Energy Alignment and Recombination in Perovskite Solar Cells: Weighted Influence on the Open Circuit Voltage

Ilario Gelmetti[a,b‡], Núria F. Montcada[a‡], Ana Pérez-Rodríguez[c], Esther Barrena*[c], Carmen Ocal[c], Inés García-Benito[d], Agustín Molina-Ontoria[d], Nazario Martín[d,e]*, Anton Vidal-Ferran[a,f]* and Emilio Palomares[a,f]*

[a.] *Institute of Chemical Research of Catalonia (ICIQ). The Barcelona Institute of Science and Technology. Avda. Països Catalans, 16. Tarragona. E-43007. Spain.*
[b.] *Departament d'Enginyeria Electrònica, Elèctrica i Automàtica, Universitat Rovira i Virgili, Avda. Països Catalans 26, 43007 Tarragona, Spain*
[c.] *Institut de Ciència de Materials de Barcelona (ICMAB-CSIC), Campus UAB, Bellaterra 08193-Barcelona, Spain.*
[d.] *IMDEA-Nanociencia, C/ Faraday, 9, Campus de Cantoblanco, E-28049, Madrid, Spain.*
[e.] *Departamento de Química Orgánica I, Facultad de Ciencias Químicas, Universidad Complutense de Madrid, Madrid, Spain.*
[f.] *ICREA. Passeig Lluis Companys, 23. Barcelona. E-08010. Spain.*
**Author information: EP epalomares@iciq.es*
‡ These authors contributed equally to this work

Abstract

In this work, we assess the possible reasons for the differences observed in open circuit voltage (V_{OC}) in mixed cation perovskite solar cells when comparing four different hole transport materials (HTMs), namely TAE-1, TAE-3, TAE-4 and spiro-OMeTAD. All these HTMs present close chemical and physical properties. Additionally to the evaluation of the HTM influence on recombination, we find that, upon deposition of the organic HTM on top of the perovskite, there is an important change in the energy levels position, and the impact on the device V_{OC} is discussed. We consider that this experimental observation could be general for other organic HTMs and would justify the difficulties for finding molecules and materials that could improve the efficiency of perovskite solar cells overcoming the solar-to-energy conversion efficiency of solar cells made using spiro-OMeTAD as holes selective contact.

Introduction

Organic-inorganic lead halide perovskites have become the focus of intense research due to their outstanding performance in hybrid photovoltaic devices.[1] Perovskite solar cells without the use of HTM achieved efficiencies of 16 %,[2] way below the efficiencies of standard perovskite solar cells using HTMs.[1] Spiro-OMeTAD is the material of choice for most reported examples of triple cation (formamidinium, methylammonium, cesium) mixed halide (bromide, iodide) lead perovskite solar cells[3] with the FTO/d-TiO_2/CsFAMAPbIBr/HTM/Au structure, where FTO is fluorine doped tin oxide, d-TiO_2 is a dense layer of titania, and Au is the gold anode. In spite of the tremendous interest in developing novel HTMs for replacing the expensive spiro-OMeTAD, improving power conversion efficiency and cell stability, it is still unclear how to rationalize the HTM design. Although one significant design parameter for maximizing the V_{OC} is the position of the Highest Occupied Molecular Orbital (HOMO) level, a clear correlation is not always found among the published results.[4–9] A complication in determining the role of the HTM on device performance is that changing the HTM often affects other photophysical properties of the solar cell with significant impact on photovoltaic behaviour.

In a previous communication, aiming to match or improve the performance of the spiro-OMeTAD based devices, we reported the easy synthesis of a new organic HTM: TAE-1 (Figure 1).[10,11] However, despite its promising properties, with a slightly deeper oxidation potential in comparison with spiro-OMeTAD (Figure 2), the solar cells fabricated with TAE-1 were unable to overcome the V_{OC} values of the perovskite solar cell obtained using spiro-OMeTAD (Table 1).

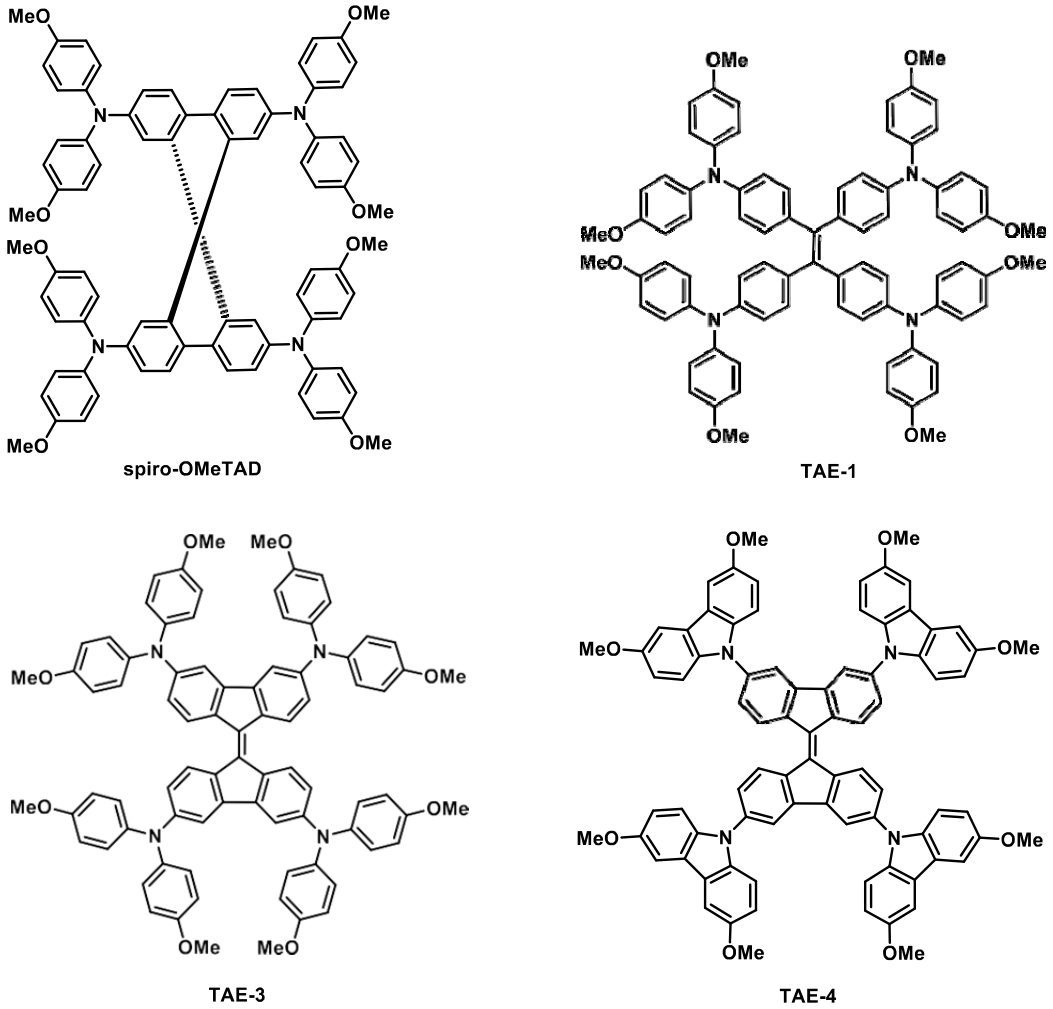

Figure 1. Molecular structures of spiro-OMeTAD, TAE-1, TAE-3 and TAE-4.

In this work, not only we replicate our observation on more HTMs, namely TAE-3 and TAE-4 (Figure 1), but we also move one step further and get insight into the origin of the observed differences in V_{OC}. Unlike our previous communication,[10] where a 400 nm layer of mesoporous titania (m-TiO_2) was used as scaffold for the perovskite, herein we investigate planar junctions fabricated using d-TiO_2 as n-type selective contact, which reduces the device complexity. We evaluate the influence of the molecular energetics, in other words, the different driving forces for the charge transfer process between the HTM and the perovskite (Figure 2), and the charge recombination between electrons at the perovskite and holes at the HTM on the V_{OC} observed in devices employing TAEs or spiro-OMeTAD. As the stack underlying the HTM is identical for all the studied devices, the relation between the V_{OC} and the electron transport material (ETM) or the perovskite characteristics[12] will not be considered.

The usage of advanced time-resolved techniques, namely Photo-Induced Charge Extraction (PICE) and Photo-Induced Transient Photo-Voltage (PI-TPV),[4,13] allows us to determine the

impact of the HTM on the energetics and charge recombination kinetics.[14–17] Further insight on the role of the interface energetics is provided by analysing the work function (WF), determined from contact potential difference (CPD) measured by Kelvin probe force microscopy (KPFM).[18,19]

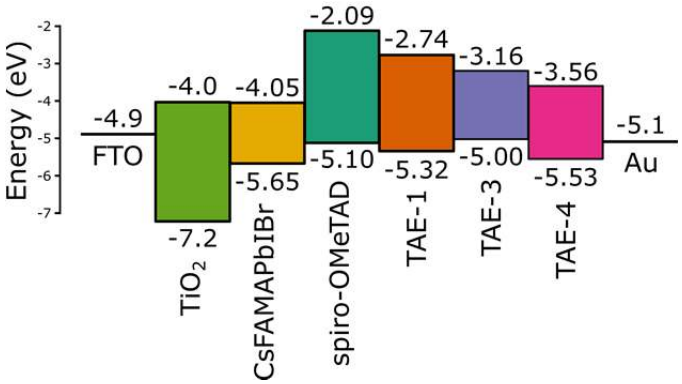

Figure 2. Schematics of the energy diagram for the materials in the perovskite solar cells studied in this work. The oxidation potential values approximating the HOMO of TAE-1, TAE-3, TAE-4 and spiro-OMeTAD have been extracted from cyclic voltammetry in solution (see Figure S14). The direct optical band gap has been determined by Tauc plot in solution (see Figures S21-S22).

Experimental

Materials

All solvents were purchased from Sigma-Aldrich and used without any additional treatment. Formamidinium iodide (FAI) and methylammonium bromide (MABr) were bought from GreatCell Solar. PbI_2 (99 %), $PbBr_2$ (99.999 %) and CsI (99.999 %) were bought form Sigma-Aldrich. All of these components are stored in a nitrogen-filled glovebox. The solution for the dense TiO_2 layer was prepared using 0.65 mL of Ti(IV) isopropoxide (Sigma-Aldrich 97 %) and 0.38 mL of acetylacetone (Sigma-Aldrich) in 5 mL of ethanol. The perovskite (CsFAMAPbIBr) precursors solution was prepared dissolving 507 mg of PbI_2, 73.4 mg of $PbBr_2$, 172 mg of FAI and 22.4 mg of MABr in 0.2 mL dimethyl sulfoxide (DMSO) mixed with 0.8 mL of N,N-dimethylformamide (DMF, anhydrous). The solution was stirred at RT for 1 hour. Then 42 µL of a 1.5 M CsI solution in DMSO were added to the previous solution. Spiro-OMeTAD (1-Material) solution was prepared dissolving 72.3 mg in 1 mL of chlorobenzene (anhydrous), then 28.8 µL of 4-tert-butylpyridine (Sigma-Aldrich) and 17.5 µL of a 520 $mg \cdot mL^{-1}$ of a Lithium bis trifluoromethylsulfonyl imide (LiTFSI, Sigma-Aldrich) solution in acetonitrile were added. TAE-1 was synthesized as reported[10] and the solution was prepared using the same additives as for the spiro-OMeTAD solution, but all the molar concentrations halved due to solubility issues. TAE-3 and TAE-4 solutions were prepared with the same additives as for spiro-OMeTAD

solution, but all the molar concentrations reduced to one third for TAE-3 and to one sixth for TAE-4 due to their lower solubility.

Novel HTMs synthesis and characterization

Complete synthetic procedure and characterization can be found in the SI. Flash chromatography was performed using silica gel (Merck, Kieselgel 60, 230–240 mesh or Scharlau 60, 230–240 mesh). Analytical thin layer chromatography was performed using aluminium-coated Merck Kieselgel 60 F254 plates. Oxidation potential in solution was measured with cyclic voltammetry measurements using an Autolab PGSTAT 30 electrochemical analyser at RT with a three-electrode configuration in dichloromethane containing approximately 1 mM of analyte. 0.1 M supporting electrolyte of NBu_4PF_6 was added. A glassy carbon electrode was used as working electrode, and platinum wires were used as counter and reference electrodes. Solutions were stirred and deaerated by bubbling nitrogen for a few minutes prior to each voltammetric measurement. Ferrocene was added as an internal standard; its oxidation potential in DCM was positioned at 0.7 V vs. NHE and HTMs' oxidation potential were recalculated in reference to NHE. The CV scanning rate was 100 $mV \cdot s^{-1}$. NMR spectra were recorded on a Bruker Advance 300 (^{1}H: 400 MHz; ^{13}C: 100 MHz) spectrometer at 298 K using partially deuterated solvents as internal standards. Coupling constants (*J*) are denoted in Hz and chemical shifts (δ) in ppm. Multiplicities are denoted as follows: s = singlet, d = doublet, t = triplet, m = multiplet. FT-IR spectra were recorded on a Bruker Tensor 27 (ATR device) spectrometer. Mass spectra matrix-assisted laser desorption ionization (coupled to a Time-of-Flight analyser) experiments (MALDI-TOF) were recorded on a MAT 95 thermo spectrometer and a Bruker REFLEX spectrometer, respectively. UV-Vis absorbance spectra were recorded in a Varian Cary 50 spectrophotometer. Direct optical band gap was estimated via Tauc plot of absorbance. Fluorescence measurements were carried out on a Fluorolog Horiba Jobin Yvon spectrofluorimeter equipped with photomultiplier detector, double monochromator and Xenon light source.

Device fabrication

All devices were fabricated using 1.5 x 1.5 cm FTO coated glasses (TEC7, 7 Ω/square, Pilkington FTO glass 2.2 mm thickness, Xinyan Technology Ltd, pre-patterned). The substrates were cleaned (ultrasonication) in water with Hellmanex soap, water and finally isopropanol; dried and UV/ozone treated for 20 minutes.

Dense TiO_2 layer was deposited (static dispensing, 80 µL) by spin-coating using the described solution at 3000 rpm, 3000 $rpm \cdot s^{-1}$, for 60 s (~30 nm) over the previously cleaned FTO. Then

the substrates were sintered at 500 °C for 30 minutes and subsequently immersed in a 40 mM $TiCl_4$ solution in 9 % HCl at 70 °C for 30 minutes, cleaned with water, with isopropanol and calcined at 500 °C for 30 minutes. Perovskite precursor solution was filtered (0.2 µm, PTFE) and deposited by spin-coating (80 µL, static dispensing, first step 1000 rpm, 1000 rpm·s^{-1}, 10 s; second step 6000 rpm, 1000 rpm·s^{-1}, 20 s; fast crystallization was induced dynamically dispensing 50 µL of chlorobenzene on the spinning substrate 5 s before the end of the second step) obtaining a 500 nm thick perovskite layer. The substrates were directly transferred from the spin coater to a hot plate and annealed at 100 °C for 60 minutes. The HTM solutions (spiro-OMeTAD, TAE-1, TAE-3 or TAE-4) were filtered (0.2 µm, PTFE) and deposited by spin-coating onto the perovskite layer (60 µL, static dispensing, spiro-OMeTAD at 4000 rpm, 4000 rpm·s^{-1}, for 30 s; TAE-1 and TAE-3 at 2000 rpm, 2000 rpm·s^{-1}, for 30 s; TAE-4 at 1000 rpm, 2000 rpm·s^{-1}, for 45 s) and similar HTM thickness were obtained (~100 nm). In order to increase the oxidative doping of the HTMs, the devices were kept 1 hour in dark in a dry air chamber. Finally, 80 nm of gold was deposited by thermal evaporation in an ultra-high vacuum chamber ($1\cdot10^{-6}$ mbar) using a shadow mask leading to 4 diodes for substrate each with an active area of 9 mm^2. The cleaning and d-TiO_2 deposition processes were performed in a class 7 clean room. The perovskite and HTM deposition processes were performed in a nitrogen-filled glovebox while purging with a nitrogen flow for reducing the DMF and DMSO vapours concentration.

Device characterization

Current-voltage characteristics were measured using a Sun 2000 solar simulator (150 W, ABET Technologies), the proper filters of the lamp were set to simulate the AM 1.5G solar spectrum, calibrated with a silicon photodiode (NREL) to obtain 1000 W·m^{-2} of light intensity. Applied voltage and current were measured with a Keithley digital 2400 Source Meter (sweep speed 0.6 V·s^{-1}, auto-scale disabled). PI-TPV and PICE measurements were carried out using a white light LED ring LUXEON® Lumileds providing different light intensities, the signal is measured in an oscilloscope Yokogawa DLM2052 registering drops in voltage. The light perturbations pulses were provided by a nanosecond PTI GL-3300 nitrogen laser. In PICE, a complete device is held at open circuit conditions and irradiated using white LEDs until the steady-state is reached, in other words, until the V_{OC} of each device is completely stabilized; then the device is simultaneously short-circuited and the LEDs are switched off. The charges, which have been accumulated during the irradiation, are extracted throughout an external circuit having an oscilloscope in parallel to a known small resistance (50 Ω). The measurements are performed at different light irradiation intensities, the voltage measured across the small resistance is converted to a current (via Ohm's law) and the integration over time gives the extracted

charge at different light intensities. The current-voltage scans data acquisition was performed with open source Python code developed in-house PyPV (https://github.com/ilario/PyPV). The data analysis for current-voltage scans, PICE and PI-TPV was performed with open source R developed in-house.

Mobility measurements via space-charge limited current

The HTM hole mobility has been estimated on a device with configuration ITO/PEDOT:PSS (25 nm)/HTM (100 nm)/Au (120 nm) from a current-voltage measurement up to 5 V. The mobility was obtained fitting the SCLC curve.[20,21]

Work Function determination via KPFM

WF measurements were carried out at room temperature and under ambient conditions using a commercial scanning probe microscopy (SPM) instrument from Nanotec Electrónica. Data were analysed using the WSxM freeware.[22] Conducting CrPt coated Si tips (by Budgetsensors) mounted on cantilevers with nominal force constant k = 3 $N \cdot m^{-1}$ were used. WF values were obtained by measuring the CPD between tip and sample that is determined from the parabolic dependence of the frequency shift versus bias voltage, Δf(V) (see SI). In this work ⊗f(V) curves were acquired for pristine CsFAMAPbIBr, spiro-OMeTAD/CsFAMAPbIBr and the diverse TAEs/CsFAMAPbIBr. To avoid tip-dependent uncertainties, CPD measurements were systematically performed on grounded on-top Au electrodes (that in air conditions has been reported to be WF_{Au} = 4.9 eV)[23] deposited on each device so that a common WF reference and reproducibility were ensured. For each sample, the CPD was measured at a minimum of 15 diverse locations and 5 curves were taken at each position. As a measure of the measurements precision, the given error corresponds to the standard deviation estimated from data obtained for each case.

Theoretical simulations

In order to simulate the UVvis spectra of the three TAE compounds, full level DFT geometry optimization of TAEs were carried out using the M06-2X[24] functional and the def2-SVP basis set[25] as implemented in Gaussian 09, Revision D.01.[26] The M06-2X/def2-SVP level of theory offers a good compromise between the size of the system and the accuracy of the results.[27] Solvent effects (tetrahydrofuran) were incorporated employing the Polarizable Continuum Model (PCM) with the integral equation formalism (IEFPCM calculations)[28] with radii and non-electrostatic terms[29] as implemented in Gaussian 09, Revision D.01.

The optimized co-ordinates were used in calculation of UVvis data employing a hybrid exchange–correlation functional (CAM-B3LYP), since this methodology has proven to be reliable in UVvis predictions.[30] The CAM-B3LYP[31] correlation functional and the previously mentioned basis set as implemented in Gaussian were used to calculate excitation energies and oscillator strengths. UVvis data obtained from computational studies were plotted using GaussSum.[32]

Results and discussion

In a previous communication[10] we compared the novel TAE-1 molecule with the reference spiro-OMeTAD as HTM for methylammonium lead iodide perovskite solar cells with mesoporous TiO_2 as ETM. Here we investigate, in depth, the influence of the HTM on the V_{OC} of a triple cation perovskite solar cell with planar TiO_2 as ETM and we introduce two novel HTMs, TAE-3 and TAE-4.

These new derivatives were prepared following a straightforward two-step synthetic procedure. The synthetic route illustrated in Scheme S1 (see Supplementary Information for more details) allowed us to obtain TAE-3 and TAE-4. Firstly, 3,3',6,6'-Tetrabromo-9,9'-bifluorenylidene was obtained from a one-pot reaction by treating 3,6-dibromo-9H-fluoren-9-one, synthesised by reported procedures,[10,33] in the presence of Lawesson's reagent in refluxing toluene. Finally, *p*-methoxydiphenylamine or 3,6- dimethoxy-9H-carbazole were covalently linked to the central unit by a four-fold Buchwald-Hartwig cross-coupling reaction to obtain TAE-3 and TAE-4 respectively in good yields. Complete structural characterization of the final compound TAE-3 and TAE-4 and the corresponding intermediates was accomplished using standard spectroscopic techniques such as ^{1}H NMR, ^{13}C NMR, FTIR, and UV-Visible. The ^{1}H NMR spectra of the final molecules reveal the characteristic signals of the bifluorenylidene core (two doublets and one double doublet corresponding to 4 protons each) and the representative signals of the donor units. In addition, mass spectrometry HRMS [MALDI-TOF] confirmed the presence of TAE-3 with a molecular ion peak $[M]^{+}$ at 1236.5029 $m{\cdot}z^{-1}$ and TAE-4 at 1228.4446 $m{\cdot}z^{-1}$. The hole mobility of the novel HTMs are not dissimilar to the spiro-OMeTAD one, being $5.9{\cdot}10^{-5}$, $8{\cdot}10^{-4}$, $7{\cdot}10^{-4}$ and $2.6{\cdot}10^{-4}$ $cm^{2}{\cdot}V^{-1}{\cdot}s^{-1}$ for TAE-1,[10] TAE-3, TAE-4 and spiro-OMeTAD[10] respectively (see Figure S27). Additionally to the experimental measurement of the oxidation potential of TAE-3 and TAE-4 (see Figure 2 and Figure S14), theoretical calculations have been used for predicting the HOMO and LUMO energies of all the novel HTMs (see Table S1 and Figures S15-S17). The oxidation potential of the HTMs follows the relation TAE-3 < spiro-OMeTAD < TAE-1 < TAE-4, being the HOMO of TAE-4 the closest to the

valence band (VB) of the perovskite. We note that the values of HOMO derived from cyclic voltammetry oxidation potential, using a reported linear relation,[34] can differ from those obtained in the solid state for example by measuring ultraviolet photoelectron spectroscopy. Nonetheless, as a first approximation, we use these values with the complementarity of DFT theoretical results. Figure 2 illustrates the trend for the HOMO values as a result of our experimental and theoretical approach.[34] However, it is possible to have both a shift in the HOMO and LUMO energy or a change in the oxidative doping density upon deposition of the HTMs onto the perovskite thin film, as explained further in the paper.

The perovskite solar cells using as HTM either one of the TAEs or spiro-OMeTAD were fabricated using the procedure described in detail in the experimental section. All comparisons were carried out within the same set of solar cells and confirmed on at least two independent sets of devices. Every HTM was deposited by spin-coating obtaining similar thicknesses of ~100 nm (see Figure S7). The average and champion device performance parameters are listed in Table 1; Figure 3 shows the reverse current-voltage scans. The complete statistics, including forward scans data, can be found in Figures S8-S13. The most interesting observation extracted from Table 1 is the larger V_{OC} in devices with spiro-OMeTAD, which is contrary to the predicted dependence[35–37] of the V_{OC} with the ionization potential, i.e., a larger V_{OC} for TAE-1 and TAE-4 than for spiro-OMeTAD. The average V_{OC} of spiro-OMeTAD devices differs from those of TAE-1 and TAE-4 devices by 90 and 170 mV, respectively.

Table 1. Reverse scan solar cell parameters (short circuit current, open circuit voltage, fill factor, power conversion efficiency) for spiro-OMeTAD and TAEs devices.

Device	J_{sc} (mA·cm^{-2})	V_{oc} (V)	FF	PCE (%)
spiro-OMeTAD	23.0 (21.4±1.6)*	1.13 (1.07±0.06)	0.75 (0.68±0.11)	18.4 (15.6±3.1)
TAE-1	20.2 (20.2±0.9)	1.02 (0.98±0.03)	0.69 (0.60±0.10)	14.3 (11.8±2.1)
TAE-3	22.5 (22.5±1.9)	0.93 (0.89±0.04)	0.74 (0.71±0.06)	15.3 (14.1±1.4)
TAE-4	24.2 (21.0±1.8)	0.97 (0.90±0.06)	0.71 (0.61±0.09)	16.5 (11.6±2.8)

* The value in parenthesis are the average and standard deviation of 85 diodes for spiro-OMeTAD, 23 diodes for TAE-1, 29 diodes for TAE-3 and 21 diodes for TAE-4 (see Figure S8).

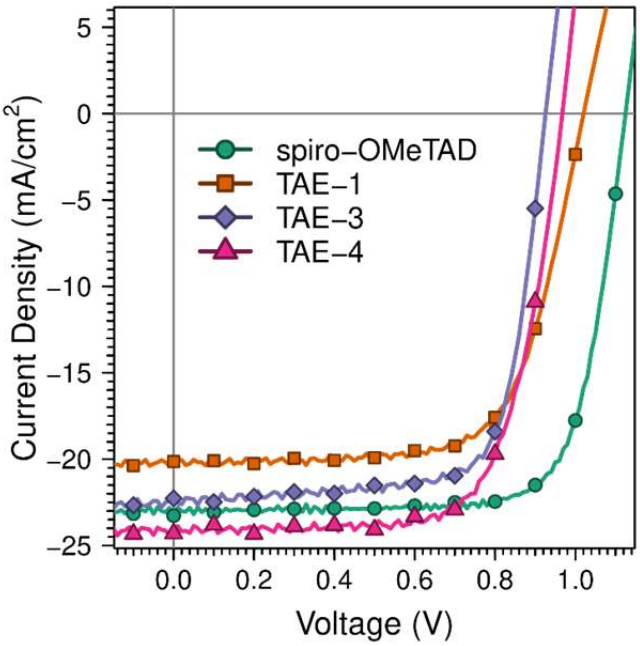

Figure 3. The current-voltage curves of the most representative perovskite devices using spiro-OMeTAD (green round points), TAE-1 (orange square points), TAE-3 (purple diamond points) and TAE-4 (magenta triangle points) as HTM under 1 sun conditions (1000 W·m^{-2}) and in reverse scan (forward curves are shown in Figure S9).

Performing the current-voltage scans at various light intensities, we obtained an ideality factor (see Figures S10-S13) of 1.57 for spiro-OMeTAD, 1.44 for TAE-1, 1.79 for TAE-3 and 1.83 for TAE-4, respectively. From this, we can state that the TAE-3 and TAE-4 trap states contributing to interfacial Shockley Read Hall (SRH) recombination are deeper in energy than those in spiro-OMeTAD and TAE-1.[38] We carried out time-resolved electrical measurements to assess how the HTM influences the free charges' recombination lifetime in the complete devices. These time-resolved techniques allowed us to determine the different origin of recombination in other type of solar cells such as organic solar cells[17,39] and dye sensitized solar cells.[40,41] PICE has been used previously to obtain the free carrier density in a device at different light bias (device V_{OC} at different light intensities). The charge distribution versus voltage is very sensitive to the presence of additives[42–44] and to differences in the HOMO energy level[45,46] leading to sensible shifts on the measured charge versus light bias voltage curves. Charge extraction of devices has been measured using the same system as described elsewhere by our group. Due to the short measurement time window (10 ms, see Fig. S40, ESI†), we did not observe any contribution from ionic migration,36 which would give a small and long lasting displacement current at larger time scales.[47,49] The charge distribution of all devices is obtained as shown in Figure 4 and each experimental curve can be fitted to a linear plus exponential dependence law. The linear component is caused by the geometric capacitance of free charges

accumulating in the selective contacts.[13,17] Since this capacitance follows the planar capacitor model, with the main parameters being the thickness of the perovskite layer and its static permittivity, no significant difference was observed for the different devices (see linear region in Figure 4). Once the photo-induced quasi-Fermi splitting in the perovskite layer approaches the built-in potential (HTM HOMO and ETM LUMO energies difference) the depletion layers in the contacts start to saturate[19,50] and the photo-generated charges will stay in the perovskite layer[51] increasing their chemical potential. This regime is called chemical capacitance or quantum capacitance and is revealed by an exponential increase in the charge versus light bias voltage plot. As can be observed in Figure 4 the voltage at which the chemical capacitance becomes relevant for each cell follows the trend TAE-3 < TAE-4 < TAE-1 < spiro-OMeTAD. From such shifts, we can infer that there is a difference in the in energy offsets respect to perovskite valence band (VB), with the most favourable alignment for spiro-OMeTAD. This is in correlation with the built-in voltage, and, as the ETM is the same for all the samples, also with the HTM HOMO energies, being spiro-OMeTAD the deepest. Interestingly, this order does not relate to the HOMO as measured by solution cyclic voltammetry and shown in Figure 2. This discrepancy can arise from differences between the solution and solid state state,[19,40–42] due to chemical reactivity[43] or intermixing with the perovskite layer components.[20,44]

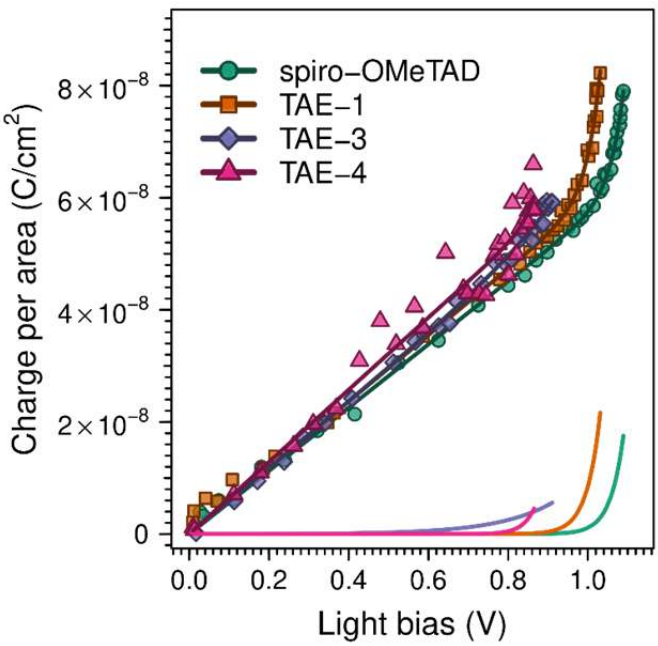

Figure 4. Charge from PICE at different light bias voltages for solar cells with TAE-1, TAE-3,TAE-4 and spiro-OMeTAD. The dark solid lines are the data fits using a linear plus exponential model $y=Ax+Be^{Cx}$. The light colour solid lines at the graph bottom represent only the exponential part of the fits: $y=Be^{Cx}$.

When considering different HTMs for fabricating a perovskite solar cell, the resulting V_{OC} will mainly relate to the HOMO energy level, as well as the recombination constant[17] and density of states disorder.[59] In our case, we will not consider the density of states disorder as we presume that it will not differ significantly for molecules with such similar chemical structures as the ones studied here. Considering the HOMO energy, a deeper level, which is a bigger built-in voltage, allows the solar cell to reach a higher V_{OC}.[57,58,60] This intuitive relation can be rationalized as follows, considering the ETM/perovskite/HTM interfacial recombination:[38,61,62] (a) the V_{OC} is the applied voltage where the amount of recombination equals the amount of photo-generation; (b) the interfacial SRH recombination is proportional to the electrons or holes concentration in the perovskite at the interface with the HTM or ETM respectively;[61,62,63] (c) these concentrations increase after the filling of the contacts' depletion layers, which happens when the quasi-Fermi levels splitting in the perovskite (that is the origin of the V_{OC}) approaches the built-in potential. Coherently, the aforementioned order of HOMO energies as obtained by the exponential onset in charge extraction (Figure 4) is reflected by the order of average V_{OC}s in Table 1: spiro-OMeTAD > TAE-1 > TAE-4 > TAE-3.

In order to analyse first the influence of the recombination, we carried out PI-TPV measurements on the devices under open circuit conditions. For all HTMs, the device's PI-TPV transient decays (see Figure 5 and S14) lead, through exponential decay fitting, to lifetimes at 1-sun illumination of the same order of magnitude, from 0.4 to 1.1 µs (see for each device the rightmost point in Figure 5 and Figure S24). We can safely state that the bulk radiative recombination is negligible compared to the interfacial recombination as in cesium containing triple cation mixed halide perovskite the charges' diffusion length has been reported in the micrometre when isolated,[64] and gets notably reduced when sandwiched between an HTM and ETM extracting layers.[4] More interestingly, referring the transient decay lifetimes at different light intensities from PI-TPV (see Figure S25) to the obtained chemical charge, subtracting the charge accumulated in the geometric capacitance, from PICE (see Figure 4) we obtain a direct relationship between free charges lifetime and charge density in the perovskite layer, as shown in Figure 5. The choice of subtracting the charges accumulated in the contacts comes from the consideration that the interfacial SRH recombination is mainly influenced by changes in the low concentration of carriers in the perovskite layer rather than by the high concentration of majority carriers in the doped contacts.[47,63]

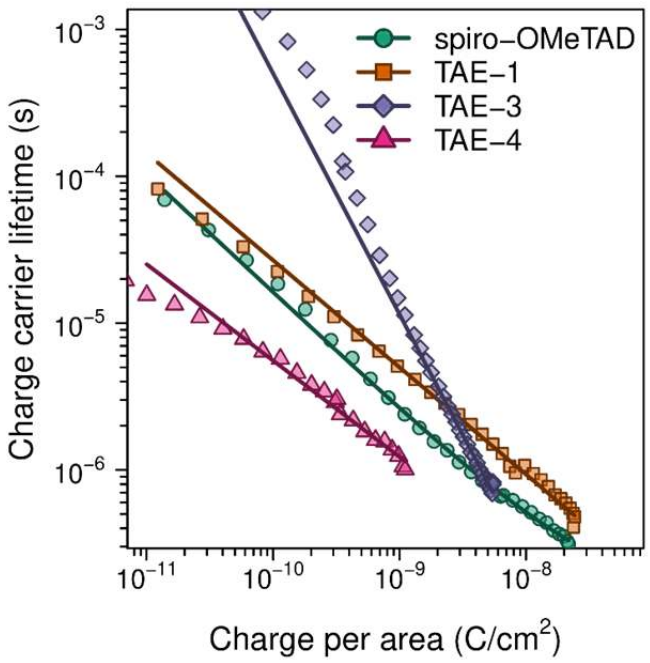

Figure 5. Charge carriers lifetime (obtained via PI-TPV) at different chemical charge (as opposed to charges assigned to geometric capacitance, obtained from the exponential part of PICE in Figure 4) of spiro-OMeTAD, TAE-1, TAE-3 and TAE-4 devices. The solid lines correspond to the respective fittings to a power law equation ($y=y_0+Ax^{-\lambda}$).[45]

As can be seen in Figure 5, the slopes for the TAE-1, TAE-4 and spiro-OMeTAD devices data are similar, indicating a common main carrier recombination pathway. In fact, the recombination order Φ obtained from the exponent λ of the power law fit (see caption of Figure 5, $\Phi = 1+\lambda$) is 1.7 for TAE-1 cell, 1.6 for TAE-4 cell and 1.8 for spiro-OMeTAD cell (value compatible with reports on surface recombination via deep-traps),[38] while deviates to 2.6 for TAE-3 cell,[45] pointing to an additional recombination pathway in the TAE-3 device, which is not the main study here and will be investigated elsewhere. Such high recombination orders are not uncommon neither in organic[65] nor in perovskite solar cells.[66,67]

Further inspection of Figure 5 shows that though higher for TAE-3, the recombination lifetime at the same chemical charge, for example at 10^{-9} C·cm^{-2}, does not drastically differ for the diverse HTMs. However, the perceived tendency does not correspond to the trend observed in V_{OC} (Table 1).

Once demonstrated that the carrier recombination between the electrons in the perovskite and the holes in the distinct HTMs is not the key factor at the origin of our observation in V_{OC}, we examine next the impact in the vacuum level misalignment at the different heterojunctions.

To evaluate any possible deviation in the relative alignment of the HTMs´ HOMO on the FTO/d-TiO_2/CsFAMAPbIBr layer, the WF has been experimentally determined for the different layer stacks from CPD measurements via KPFM (see experimental section and SI). As can be seen in Figure 6, the obtained WF of the FTO/d-TiO_2/CsFAMAPbIBr surface is 4.24±0.04 eV, which is comparable with the reported value for $MAPbI_3$ on *n*-type substrates.[68,69] When the HTMs are deposited on top of the perovskite, vacuum level (V_L) alignment is basically fulfilled for spiro-OMeTAD, TAE-1 and TAE-4, while the relative work function of TAE-3 with respect to that of the perovskite leads to an upward shift of the V_L as large as ~200 mV. This implies an upward shift of the HOMO of TAE-3 from the VB of the perovskite, within the rigid band model.

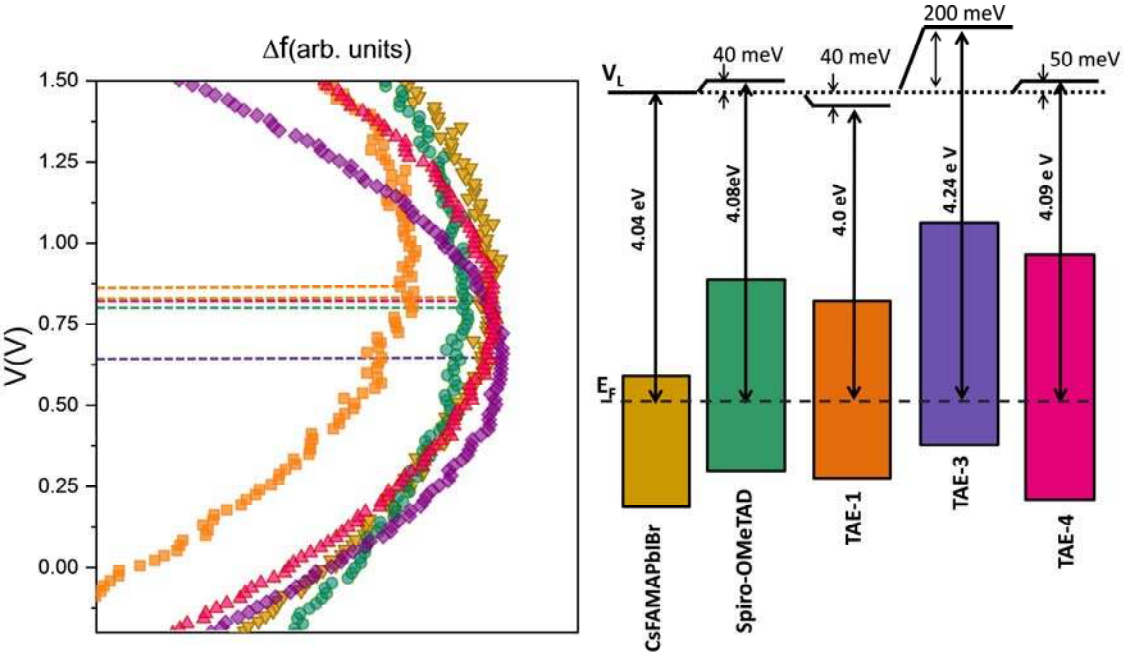

Figure 6. (left) CPD measurements between the KPFM tip and the surfaces of pristine CsFAMAPbIBr and the different HTMs devices (spiro-OMeTAD, TAE-1, TAE-3 and TAE-4). The corresponding WF values obtained from the parabolic fit of the data (see experimental section) are given in the schematics (right) of the proposed energy diagram. The corresponding vacuum level (V_L) shifts are obtained from the WF values.

In agreement with previous works[6,9] our results show that the design of new HTMs, for optimizing the solar cell performance and obtaining higher V_{OC} in the heterojunction, does not only consist of lowering the HOMO energy level. Notwithstanding that the lower V_{OC} for TAE-3 can be correlated with its less favourable energy alignment with the perovskite and its larger interfacial recombination with respect to the other HTMs , the fact is that for TAE-1, TAE-4 and spiro-OMeTAD the V_{OC} shows no correlation with the corresponding HOMO level position.

The whole experimental data and analysis presented here suggest that for the design of novel HTMs that aim to overcome the solar to energy conversion of the spiro-OMeTAD careful

analysis of the energetics at the interface between the organic semiconductor material and the perovskite must be taken into account in conjunction with carrier mobility properties and interfacial carrier recombination processes

Conclusions

We present a thorough investigation with the aim of shedding light on the underlying reason for the changes of the opencircuit voltage in mixed cation perovskite solar cells using two already known and two unpublished hole transporting materials: spiro-OMeTAD, TAE-1, TAE-3 and TAE-4, all with quite similar chemical structures. The choice of these HTMs is not arbitrary as they contain the most common moieties used in the myriad of novel HTMs described in the scientific literature focussed on perovskite solar cells. We observe how the energy levels as obtained by the cyclic voltammograms are a valid starting point when trying to predict the device characteristics. However, as we have demonstrated, it is possible that the HOMO energy values differ importantly when the organic semiconductor molecule is deposited on top of the perovskite semiconductor material.

By means of photo-induced charge extraction, we have been able to obtain a better indication of the HOMO level position of the HTM when layered in a solar cell stack. Kelvin probe force microscopy has been employed as a local probe for confirming the work function actually in place in a complete and functional device. Complementing this experimental information with the study of the interfacial recombination processes occurring under solar cell operando conditions – via the photoinduced transient photovoltage – has allowed us to disentangle the complex influence of the HTM on the device photovoltaic performances. The shift of the energy levels of the TAEmolecules upon contact with the perovskite layer, together with changes in recombination rate, influences the measured VOC values, which are notably different fromthe expected ones related to the HOMO energy values inferred from the cyclic voltammetry experiments further supported by the advanced DFT calculations.

We have shown that the design of a HTM that can reach the expected maximum theoretical efficiency in perovskite solar cells will require fine-tuning of the energetics at the interface between the HTM and the perovskite, for instance the use of a self-assembled monolayer of molecular dipoles, etc., without increasing the interfacial carrier recombination processes between the HTM and the semiconductor perovskite.

References

1 M. A. Green, Y. Hishikawa, E. D. Dunlop, D. H. Levi, J. Hohl-Ebinger and A. W. Y. Ho-Baillie, *Prog. Photovoltaics Res. Appl.*, 2018, **26**, 427–436.

2 Y. Li, S. Ye, W. Sun, W. Yan, Y. Li, Z. Bian, Z. Liu, S. Wang and C. Huang, *J. Mater. Chem. A*, 2015, **3**, 18389–18394.

3 M. Saliba, T. Matsui, J.-Y. Seo, K. Domanski, J.-P. Correa-Baena, M. K. Nazeeruddin, S. M. Zakeeruddin, W. Tress, A. Abate, A. Hagfeldt and M. Grätzel, *Energy Environ. Sci.*, 2016, **9**, 1989–1997.

4 J. Jiménez-López, W. Cambarau, L. Cabau and E. Palomares, *Sci. Rep.*, 2017, **7**, 6101.

5 A. Abate, M. Planells, D. J. Hollman, V. Barthi, S. Chand, H. J. Snaith and N. Robertson, *Phys. Chem. Chem. Phys.*, 2015, **17**, 2335–2338.

6 L. E. Polander, P. Pahner, M. Schwarze, M. Saalfrank, C. Koerner and K. Leo, *APL Mater.*, 2014, **2**, 081503.

7 S. M. Park, S. M. Mazza, Z. Liang, A. Abtahi, A. M. Boehm, S. R. Parkin, J. E. Anthony and K. R. Graham, *ACS Appl. Mater. Interfaces*, 2018, **10**, 15548–15557.

8 N. Ishida, A. Wakamiya and A. Saeki, *ACS Photonics*, 2016, **3**, 1678–1688.

9 R. A. Belisle, P. Jain, R. Prasanna, T. Leijtens and M. D. McGehee, *ACS Energy Lett.*, 2016, **1**, 556–560.

10 L. Cabau, I. Garcia-Benito, A. Molina-Ontoria, N. F. Montcada, N. Martin, A. Vidal-Ferran and E. Palomares, *Chem. Commun.*, 2015, **51**, 13980–13982.

11 H. Choi, K. Do, S. Park, J.-S. Yu and J. Ko, *Chem. - A Eur. J.*, 2015, **21**, 15919–15923.

12 C. Bi, Q. Wang, Y. Shao, Y. Yuan, Z. Xiao and J. Huang, *Nat. Commun.*, 2015, **6**, 7747.

13 I. Gelmetti, L. Cabau, N. F. Montcada and E. Palomares, *ACS Appl. Mater. Interfaces*, 2017, **9**, 21599–21605.

14 T. Du, J. Kim, J. Ngiam, S. Xu, P. R. F. Barnes, J. R. Durrant and M. A. McLachlan, *Adv. Funct. Mater.*, 2018, **28**, 1801808.

15 J. M. Marin-Beloqui, J. P. Hernández and E. Palomares, *Chem. Commun.*, 2014, **50**, 14566–14569.

16 J. M. Marin-Beloqui, L. Lanzetta and E. Palomares, *Chem. Mater.*, 2016, **28**, 207–213.

17 J. W. Ryan and E. Palomares, *Adv. Energy Mater.*, 2017, **7**, 1601509.

18 A. Opitz, *J. Phys. Condens. Matter*, 2017, **29**, 133001.

19 I. M. Hermes, Y. Hou, V. W. Bergmann, C. J. Brabec and S. A. L. Weber, *J. Phys. Chem. Lett.*, 2018, 6249–6256.

20 P. N. Murgatroyd, *J. Phys. D. Appl. Phys.*, 1970, **3**, 308.

21 J. A. Röhr, D. Moia, S. A. Haque, T. Kirchartz and J. Nelson, *J. Phys. Condens. Matter*, 2018, **30**, 105901.

22 I. Horcas, R. Fernández, J. M. Gómez-Rodríguez, J. Colchero, J. Gómez-Herrero and A. M. Baro, *Rev. Sci. Instrum.*, 2007, **78**, 013705.

23 I. D. Baikie, A. C. Grain, J. Sutherland and J. Law, *Appl. Surf. Sci.*, 2014, **323**, 45–53.

24 M. W. Wong, K. B. Wiberg and M. J. Frisch, *J. Am. Chem. Soc.*, 1992, **114**, 1645–1652.

25 F. Weigend and R. Ahlrichs, *Phys. Chem. Chem. Phys.*, 2005, **7**, 3297.

26 M. J. Frisch, G. W. Trucks, H. B. Schlegel, G. E. Scuseria, M. A. Robb, J. R. Cheeseman, G. Scalmani, V. Barone, G. A. Petersson, H. Nakatsuji, X. Li, M. Caricato, A. V Marenich, J. Bloino, B. G. Janesko, R. Gomperts, B. Mennucci, H. P. Hratchian, J. V Ortiz, A. F. Izmaylov, J. L. Sonnenberg, Williams, F. Ding, F. Lipparini, F. Egidi, J. Goings, B. Peng, A. Petrone, T. Henderson, D. Ranasinghe, V. G. Zakrzewski, J. Gao, N. Rega, G. Zheng, W. Liang, M. Hada, M. Ehara, K. Toyota, R. Fukuda, J. Hasegawa, M. Ishida, T. Nakajima, Y. Honda, O. Kitao, H. Nakai, T. Vreven, K. Throssell, J. A. Montgomery Jr., J. E. Peralta, F. Ogliaro, M. J. Bearpark, J. J. Heyd, E. N. Brothers, K. N. Kudin, V. N. Staroverov, T. A. Keith, R. Kobayashi, J. Normand, K. Raghavachari, A. P. Rendell, J. C. Burant, S. S. Iyengar, J. Tomasi, M. Cossi, J. M. Millam, M. Klene, C. Adamo, R. Cammi, J. W. Ochterski, R. L. Martin, K. Morokuma, O. Farkas, J. B. Foresman and D. J. Fox, 2009, Gaussian 09.

27 B. Balakrishna, A. Bauzá, A. Frontera and A. Vidal-Ferran, *Chem. - A Eur. J.*, 2016, **22**, 10607–10613.

28 G. Scalmani and M. J. Frisch, *J. Chem. Phys.*, 2010, **132**, 114110.

29 A. V Marenich, C. J. Cramer and D. G. Truhlar, *J. Phys. Chem. B*, 2009, **113**, 6378–6396.

30 S. Kupfer, J. Guthmuller and L. González, *J. Chem. Theory Comput.*, 2013, **9**, 543–554.

31 T. Yanai, D. P. Tew and N. C. Handy, *Chem. Phys. Lett.*, 2004, **393**, 51–57.

32 N. M. O'boyle, A. L. Tenderholt and K. M. Langner, *J. Comput. Chem.*, 2008, **29**, 839–845.

33 B. Wang, Z. Xie, Y. Li, Z. Yang and L. Chen, *Macromolecules*, 2018, **51**, 3443–3449.

34 B. W. D'Andrade, S. Datta, S. R. Forrest, P. Djurovich, E. Polikarpov and M. E. Thompson, *Org. Electron. physics, Mater. Appl.*, 2005, **6**, 11–20.

35 H.-Y. Chen, J. Hou, S. Zhang, Y. Liang, G. Yang, Y. Yang, L. Yu, Y. Wu and G. Li, *Nat. Photonics*, 2009, **3**, 649–653.

36 Y. S. Kwon, J. Lim, H.-J. Yun, Y.-H. Kim and T. Park, *Energy Environ. Sci.*, 2014, **7**, 1454.

37 K. Rakstys, A. Abate, M. I. Dar, P. Gao, V. Jankauskas, G. Jacopin, E. Kamarauskas, S. Kazim, S. Ahmad, M. Grätzel and M. K. Nazeeruddin, *J. Am. Chem. Soc.*, 2015, **137**, 16172–16178.

38 P. Calado, D. Burkitt, J. Yao, J. Troughton, T. M. Watson, M. J. Carnie, A. M. Telford, B. C. O'Regan, J. Nelson and P. R. F. Barnes, 2018, arXiv:1804.09049.

39 D. Fernandez, A. Viterisi, V. Challuri, J. W. Ryan, E. Martinez-Ferrero, F. Gispert-Guirado, M. Martinez, E. Escudero, C. Stenta, L. F. Marsal and E. Palomares, *ChemSusChem*, 2017, **10**, 3118–3134.

40 M. Godfroy, C. Aumaitre, F. Caffy, Y. Kervella, L. Cabau, L. Pellejà, P. Maldivi, S. Narbey, F. Oswald, E. Palomares, D. Joly and R. Demadrille, *Dye. Pigment.*, 2017, **146**, 352–360.

41 P. R. F. Barnes, K. Miettunen, X. Li, A. Y. Anderson, T. Bessho, M. Grätzel and B. C. O'Regan, *Adv. Mater.*, 2013, **25**, 1881–1922.

42 B. C. O'Regan, K. Bakker, J. Kroeze, H. Smit, P. Sommeling and J. R. Durrant, *J. Phys. Chem. B*, 2006, **110**, 17155–17160.

43 S. Nakade, T. Kanzaki, W. Kubo, T. Kitamura, Y. Wada and S. Yanagida, *J. Phys. Chem. B*, 2005, **109**, 3480–3487.

44 Y.-C. Chang, H.-P. Wu, N. M. Reddy, H.-W. Lee, H.-P. Lu, C.-Y. Yeh and E. W.-G. Diau, *Phys. Chem. Chem. Phys.*, 2013, **15**, 4651.

45 D. Credgington, R. Hamilton, P. Atienzar, J. Nelson and J. R. Durrant, *Adv. Funct. Mater.*, 2011, **21**, 2744–2753.

46 A. Sánchez-Díaz, M. Izquierdo, S. Filippone, N. Martin and E. Palomares, *Adv. Funct. Mater.*, 2010, **20**, 2695–2700.

47 B. C. O'Regan, P. R. F. Barnes, X. Li, C. Law, E. Palomares and J. M. Marin-Beloqui, *J. Am. Chem. Soc.*, 2015, **137**, 5087–5099.

48 C. Eames, J. M. Frost, P. R. F. Barnes, B. C. O'Regan, A. Walsh and M. S. Islam, *Nat. Commun.*, 2015, **6**, 7497.

49 D. Moia, I. Gelmetti, P. Calado, W. Fisher, M. Stringer, O. Game, Y. Hu, P. Docampo, D. Lidzey, E. Palomares, J. Nelson and P. R. F. Barnes, 2018, arXiv:1805.06446.

50 F. Fabregat-Santiago, G. Garcia-Belmonte, I. Mora-Seró and J. Bisquert, *Phys. Chem. Chem. Phys.*, 2011, **13**, 9083.

51 V. W. Bergmann, Y. Guo, H. Tanaka, I. M. Hermes, D. Li, A. Klasen, S. A. Bretschneider, E. Nakamura, R. Berger and S. A. L. Weber, *ACS Appl. Mater. Interfaces*, 2016, **8**, 19402–19409.

52 P. Sehati, S. Braun and M. Fahlman, *Chem. Phys. Lett.*, 2013, **583**, 38–41.

53 F. Bussolotti, J. Yang, A. Hinderhofer, Y. Huang, W. Chen, S. Kera, A. T. S. Wee and N. Ueno, *Phys. Rev. B*, 2014, **89**, 115319.

54 T. Breuer, A. Karthäuser and G. Witte, *Adv. Mater. Interfaces*, 2016, **3**, 1500452.

55 J. Carrillo, A. Guerrero, S. Rahimnejad, O. Almora, I. Zarazua, E. Mas-Marza, J. Bisquert and G. Garcia-Belmonte, *Adv. Energy Mater.*, 2016, **6**, 1502246.

56 S. Kim, S. Bae, S.-W. Lee, K. Cho, K. D. Lee, H. Kim, S. Park, G. Kwon, S.-W. Ahn, H.-M. Lee, Y. Kang, H.-S. Lee and D. Kim, *Sci. Rep.*, 2017, **7**, 1200.

57 C. J. Brabec, A. Cravino, D. Meissner, N. S. Sariciftci, T. Fromherz, M. T. Rispens, L. Sanchez and J. C. Hummelen, *Adv. Funct. Mater.*, 2001, **11**, 374–380.

58 A. Gadisa, M. Svensson, M. R. Andersson and O. Inganäs, *Appl. Phys. Lett.*, 2004, **84**, 1609–1611.

59 N. K. Elumalai and A. Uddin, *Energy Environ. Sci.*, 2016, **9**, 391–410.

60 C. Uhrich, D. Wynands, S. Olthof, M. K. Riede, K. Leo, S. Sonntag, B. Maennig and M. Pfeiffer, *J. Appl. Phys.*, 2008, **104**, 043107.

61 M. Stolterfoht, P. Caprioglio, C. M. Wolff, J. A. Márquez, J. Nordmann, S. Zhang, D. Rothhart, U. Hörmann, A. Redinger, L. Kegelmann, S. Albrecht, T. Kirchartz, M. Saliba, T. Unold and D. Neher, 2018, arXiv:1810.01333.

62 M. Stolterfoht, C. M. Wolff, J. A. Márquez, S. Zhang, C. J. Hages, D. Rothhardt, S. Albrecht, P. L. Burn, P. Meredith, T. Unold and D. Neher, *Nat. Energy*, 2018, **3**, 847–854.

63 W. Shockley and W. T. Read, *Phys. Rev.*, 1952, **87**, 835–842.

64 S. Liu, W. Huang, P. Liao, N. Pootrakulchote, H. Li, J. Lu, J. Li, F. Huang, X. Shai, X. Zhao, Y. Shen, Y.-B. Cheng and M. Wang, *J. Mater. Chem. A*, 2017, **5**, 22952–22958.

65 T. Kirchartz, B. E. Pieters, J. Kirkpatrick, U. Rau and J. Nelson, *Phys. Rev. B*, 2011, **83**, 115209.

66 Y.-C. Shih, L. Wang, H.-C. Hsieh and K.-F. Lin, *ACS Appl. Mater. Interfaces*, 2018, **10**, 11722–11731.

67 A. Baumann, K. Tvingstedt, M. C. Heiber, S. Väth, C. Momblona, H. J. Bolink and V. Dyakonov, *APL Mater.*, 2014, **2**, 081501.

68 E. M. Miller, Y. Zhao, C. C. Mercado, S. K. Saha, J. M. Luther, K. Zhu, V. Stevanović, C. L. Perkins and J. van de Lagemaat, *Phys. Chem. Chem. Phys.*, 2014, **16**, 22122–22130.

69 S. Olthof and K. Meerholz, *Sci. Rep.*, 2017, **7**, 40267.

Acknowledgements

EP and AVF thankMINECO (projects CTQ2013-47183 and CTQ2017-89814-P). NM thanks the European Research Council (ERC-320441- Chirallcarbon), the CAM (Y2018/NMT-4783QUIMTRONIC-CM) and the Spanish Ministry of Economy and Competitiveness MINECO (projects CTQ2014-52045-R, CTQ2015-71154-P, CTQ2016-80042-R, CTQ2017-83531-R and CTQ2016-81911-REDT). NM also thanks the Alexander von Humboldt Foundation and the Unidad de Excelencia Severo Ochoa SEV-2016-0686 is acknowledged. EP and AV are also grateful to ICIQ and ICREA for economical support. EB and CO thank the Generalitat de Catalunya 2017 SGR668 and 2017 SGR669, the MINEICO projects MAT2016-77852-C2-1-R (AEI/FEDER, UE), MAT2015-68994-REDC and the ‘‘Severo Ochoa’’ Program for Centers of Excellence in R&D (SEV-2015-0496). IG thanks Jesús Jiménez-López for the fruitful discussions.

Author contributions

NFM and IG contributed equally to this work. IG prepared the solar cells. IG and NFM measured current-voltage curves. IG carried out the PICE and PI-TPV experiments. NFM measured mobility via SCLC. EP and NFM designed the experiments and supervised the experimental part. EP, NFM and IG interpreted the data measured using PICE and PI-TPV. AV carried out the HOMO-LUMO calculations and UVvis simulations. NM and AM designed the TAE-1, TAE-3 and TAE-4. IGB synthesized the molecules. APR, EB and CO performed and analysed the Kelvin probe force microscopy contact potential measurements. The manuscript was written through contributions of all authors. All authors have given approval to the final version of the manuscript.

Additional Information

Supplementary information accompanies this paper .

Competing Interests: The authors declare no competing financial interests.

Supporting Information

Energy Alignment and Recombination in Perovskite Solar Cells: Weighted Influence on the Open Circuit Voltage

Ilario Gelmetti[a,b‡], Núria F. Montcada[a‡], Ana Pérez-Rodríguez[c], Esther Barrena*[c], Carmen Ocal[c], Inés García-Benito[d], Agustín Molina-Ontoria[d], Nazario Martín[d,e*], Anton Vidal-Ferran[a,f*], and Emilio Palomares[a,f*]

a. Institute of Chemical Research of Catalonia (ICIQ). The Barcelona Institute of Science and Technology. Avda. Països Catalans, 16. Tarragona. E-43007. Spain.

b. Departament d'Enginyeria Electrònica, Elèctrica i Automàtica, Universitat Rovira i Virgili, Avda. Països Catalans 26, 43007 Tarragona, Spain

c. Institut de Ciència de Materials de Barcelona (ICMAB-CSIC), Campus UAB, Bellaterra 08193-Barcelona, Spain.

d. IMDEA-Nanociencia, C/ Faraday, 9, Campus de Cantoblanco, E-28049, Madrid, Spain.

e. Departamento de Química Orgánica I, Facultad de Ciencias Químicas, Universidad Complutense de Madrid, Madrid, Spain.

f. ICREA. Passeig Lluis Companys, 23. Barcelona. E-08010. Spain.

Author information: EP epalomares@iciq.es

‡ These authors contributed equally to this work

Contents

1. Experimental details

Materials

All solvents were purchased from Sigma-Aldrich and used without any additional treatment. Formamidinium iodide (FAI) and methylammonium bromide (MABr) were bought from GreatCell Solar. PbI_2 (99 %), $PbBr_2$ (99.999 %) and CsI (99.999 %) were bought form Sigma-Aldrich. All of these components are stored in a nitrogen-filled glovebox. The solution for the dense TiO_2 layer was prepared using 0.65 mL of Ti(IV) isopropoxide (Sigma-Aldrich 97 %) and 0.38 mL of acetylacetone (Sigma-Aldrich) in 5 mL of ethanol. The perovskite (CsFAMAPbIBr) precursors solution was prepared dissolving 507 mg of PbI_2, 73.4 mg of $PbBr_2$, 172 mg of FAI and 22.4 mg of MABr in 0.2 mL dimethyl sulfoxide (DMSO) mixed with 0.8 mL of N,N-dimethylformamide (DMF, anhydrous). The solution was stirred at RT for 1 hour. Then 42 µL of a 1.5 M CsI solution in DMSO were added to the previous solution. Spiro-OMeTAD (1-Material) solution was prepared dissolving 72.3 mg in 1 mL of chlorobenzene (anhydrous), then 28.8 µL of 4-tert-butylpyridine (Sigma-Aldrich) and 17.5 µL of a 520 $mg \cdot mL^{-1}$ of a Lithium bis trifluoromethylsulfonyl imide (LiTFSI, Sigma-Aldrich) solution in acetonitrile were added. TAE-1 was synthesized as reported[1] and the solution was prepared using the same additives as for the spiro-OMeTAD solution, but all the molar concentrations halved due to solubility issues. TAE-3 and TAE-4 solutions were prepared with the same additives as for spiro-OMeTAD solution, but all the molar concentrations reduced to one third for TAE-3 and to one sixth for TAE-4 due to their lower solubility.

Novel HTMs synthesis and characterization

Complete synthetic procedure and characterization can be found in the SI. Flash chromatography was performed using silica gel (Merck, Kieselgel 60, 230–240 mesh or Scharlau 60, 230–240 mesh). Analytical thin layer chromatography was performed using aluminium-coated Merck Kieselgel 60 F254 plates. Oxidation potential in solution was measured with cyclic voltammetry measurements using an Autolab PGSTAT 30 electrochemical analyser at RT with a three-electrode configuration in dichloromethane containing approximately 1 mM of analyte. 0.1 M supporting electrolyte of NBu_4PF_6 was added. A glassy carbon electrode was used as working electrode, and platinum wires were used as counter and reference electrodes. Solutions were stirred and deaerated by bubbling nitrogen for a few minutes prior to each voltammetric measurement. Ferrocene was added as an internal standard; its oxidation potential in DCM was positioned at 0.7 V vs. NHE and HTMs' oxidation potential were recalculated in reference to NHE. The CV scanning rate was 100 $mV \cdot s^{-1}$. NMR spectra were recorded on a Bruker Advance 300 (^1H: 400 MHz; ^{13}C: 100 MHz) spectrometer at 298 K using partially deuterated solvents as internal standards. Coupling constants (*J*) are denoted in Hz and chemical shifts (*δ*) in ppm. Multiplicities are denoted as follows: s = singlet, d = doublet, t = triplet, m = multiplet. FT-IR spectra were recorded on a Bruker Tensor 27 (ATR device) spectrometer. Mass spectra matrix-assisted laser desorption ionization (coupled to a Time-of-Flight analyser) experiments (MALDI-TOF) were recorded on a MAT 95 thermo spectrometer and a Bruker REFLEX spectrometer, respectively. UV-Vis absorbance spectra were recorded in a Varian Cary 50 spectrophotometer. Direct optical band gap was estimated via Tauc plot of absorbance. Fluorescence measurements were carried out on a Fluorolog Horiba Jobin Yvon spectrofluorimeter equipped with photomultiplier detector, double monochromator and Xenon light source.

Device fabrication

All devices were fabricated using 1.5 x 1.5 cm FTO coated glasses (TEC7, 7 Ω/square, Pilkington FTO glass 2.2 mm thickness, Xinyan Technology Ltd, pre-patterned). The substrates were cleaned (ultrasonication) in water with Hellmanex soap, water and finally isopropanol; dried and UV/ozone treated for 20 minutes. Dense TiO_2 layer was deposited (static dispensing, 80 µL) by spin-coating using the described solution at 3000 rpm, 3000 $rpm \cdot s^{-1}$, for 60 s (~30 nm) over the previously cleaned FTO. Then the substrates were sintered at 500 °C for 30 minutes and subsequently immersed in a 40 mM $TiCl_4$ solution in 9 % HCl at 70 °C for 30 minutes, cleaned with water, with isopropanol and calcined at 500 °C for 30 minutes. Perovskite

precursor solution was filtered (0.2 µm, PTFE) and deposited by spin-coating (80 µL, static dispensing, first step 1000 rpm, 1000 rpm·s^{-1}, 10 s; second step 6000 rpm, 1000 rpm·s^{-1}, 20 s; fast crystallization was induced dynamically dispensing 50 µL of chlorobenzene on the spinning substrate 5 s before the end of the second step) obtaining a 550-600 nm thick perovskite layer. The substrates were directly transferred from the spin coater to a hot plate and annealed at 100 °C for 60 minutes. The HTM solutions (spiro-OMeTAD, TAE-1, TAE-3 or TAE-4) were filtered (0.2 µm, PTFE) and deposited by spin-coating onto the perovskite layer (60 µL, static dispensing, spiro-OMeTAD at 4000 rpm, 4000 rpm·s^{-1}, for 30 s; TAE-1 and TAE-3 at 2000 rpm, 2000 rpm·s^{-1}, for 30 s; TAE-4 at 1000 rpm, 2000 rpm·s^{-1}, for 45 s) and similar HTM thickness were obtained (~50 nm). In order to increase the oxidative doping of the HTMs, the devices were kept 1 hour in dark in a dry air chamber. Finally, 80 nm of gold was deposited by thermal evaporation in an ultra-high vacuum chamber (1·10^{-9} bar) using a shadow mask leading to 4 diodes for substrate each with an active area of 9 mm^2. The cleaning and d-TiO_2 deposition processes were performed in a class 7 clean room. The perovskite and HTM deposition processes were performed in a nitrogen-filled glovebox while purging with a nitrogen flow for reducing the DMF and DMSO vapours concentration.

Device characterization

Current-voltage characteristics were measured using a Sun 2000 solar simulator (150 W, ABET Technologies), the proper filters of the lamp were set to simulate the AM 1.5G solar spectrum, calibrated with a silicon photodiode (NREL) to obtain 1000 W·m^{-2} of light intensity. Applied voltage and current were measured with a Keithley digital 2400 Source Meter (sweep speed 0.6 V·s^{-1}, auto-scale disabled).

TPV and CE measurements were carried out using a white light LED ring LUXEON® Lumileds providing different light intensities, the signal is measured in an oscilloscope Yokogawa DLM2052 registering drops in voltage. The light perturbations pulses were provided by a nanosecond PTI GL-3300 nitrogen laser.

In CE, a complete device is held at open circuit conditions and irradiated using white LEDs until the steady-state is reached, in other words, until the V_{OC} of each device is completely stabilized; then the device is simultaneously short-circuited and the LEDs are switched off. The charges, which have been accumulated during the irradiation, are extracted throughout an external circuit having an oscilloscope in parallel to a known small resistance (50 Ω). The measurements are performed at different light irradiation intensities, the voltage measured across the small resistance is converted to a current (via Ohm's law) and the integration over time gives the extracted charge at different light intensities.

The current-voltage scans data acquisition was performed with open source Python code developed in-house PyPV (https://github.com/ilario/PyPV). The data analysis for current-voltage scans, CE and TPV was performed with open source R developed in-house (https://github.com/ilario/photophysics-data-processing-R).

For the morphological characterization, thicknesses were measured scratching the surface and using a calibrated profilometer (Ambios Tech. XP-1). The surface roughness characterization has been done via AFM (Pico SPM II) and processed with WSxM software.[2] The superficial features were further investigated via ESEM-EDX (FEI Quanta 600). Cross section images of complete devices were recorded using ESEM system FEI Quanta 600 in high vacuum (10^{-8} bar) with an accelerating voltage of 20 kV.

XRD measurements were made using a Bruker-AXS D8-Discover diffractometer equipped with parallel incident beam (Göbel mirror), vertical θ-θ goniometer, XYZ motorized stage and with a GADDS (General Area Diffraction System). Complete solar cell devices were placed directly on the sample holder and the area of interest (typically a region between two diodes, avoiding the area with the gold electrode) was selected with the aid of a video-laser focusing system. An X-ray collimator system allows to analyze areas of 500 µm. The X-ray diffractometer was operated at 40 kV and 40 mA to generate Cu Kα radiation. The GADDS detector was a HI-STAR (multiwire proportional counter of 30x30 cm with a 1024x1024 pixel). We collected frames (2D XRD patterns) covering 15-70° 2θ from three different detector positions at a distance of 15 cm from the sample. The exposition time was 300 s per frame and it was chi-integrated to generate the conventional 2θ vs. intensity diffractogram. Identification of the minerals was achieved by comparison of the XRD diffractogram with the ICDD data base (release 2007) using Diffracplus Evaluation software (Bruker 2007).

Mobility measurements via space-charge limited current

The HTM hole mobility has been estimated on a device with configuration ITO/PEDOT:PSS (25 nm)/HTM (100 nm)/Au (120 nm) from a current-voltage measurement up to 5 V. The mobility was obtained fitting the SCLC curve.[3,4]

Work Function determination via KPFM

WF measurements were carried out at room temperature and under ambient conditions using a commercial scanning probe microscopy (SPM) instrument from Nanotec Electrónica. Data were analysed using the WSxM freeware.[2] Conducting CrPt coated Si tips (by Budgetsensors) mounted on cantilevers with nominal force constant $k = 3\ N{\cdot}m^{-1}$ were used. WF values were obtained by measuring the CPD between tip and sample that is determined from the parabolic dependence of the frequency shift versus bias voltage, $\Delta f(V)$ (see SI). In this work $\Delta f(V)$ curves were acquired for pristine CsFAMAPbIBr, spiro-OMeTAD/CsFAMAPbIBr and the diverse TAEs/CsFAMAPbIBr. To avoid tip-dependent uncertainties, CPD measurements were systematically performed on grounded on-top Au electrodes (that in air conditions has been reported to be $WF_{Au} = 4.9$ eV)[5] deposited on each device so that a common WF reference and reproducibility were ensured. For each sample, the CPD was measured at a minimum of 15 diverse locations and 5 curves were taken at each position. As a measure of the measurements precision, the given error corresponds to the standard deviation estimated from data obtained for each case.

Theoretical simulations

In order to simulate the UVvis spectra of the three TAE compounds, full level DFT geometry optimization of TAEs were carried out using the M06-2X[6] functional and the def2-SVP basis set[7] as implemented in Gaussian 09, Revision D.01.[8] The M06-2X/def2-SVP level of theory offers a good compromise between the size of the system and the accuracy of the results.[9] Solvent effects (tetrahydrofuran) were incorporated employing the Polarizable Continuum Model (PCM) with the integral equation formalism (IEFPCM calculations)[10] with radii and non-electrostatic terms[11] as implemented in Gaussian 09, Revision D.01. The optimized co-ordinates were used in calculation of UVvis data employing a hybrid exchange–correlation functional (CAM-B3LYP), since this methodology has proven to be reliable in UVvis predictions.[12] The CAM-B3LYP[13] correlation functional and the previously mentioned basis set as implemented in Gaussian were used to calculate excitation energies and oscillator strengths. UVvis data obtained from computational studies were plotted using GaussSum.[14]

2. Novel HTMs synthesis

Compounds **1**, **2,** and **TAE-1** were prepared according to previously reported synthetic procedures[1,15] and showed identical spectroscopic properties to those reported therein.

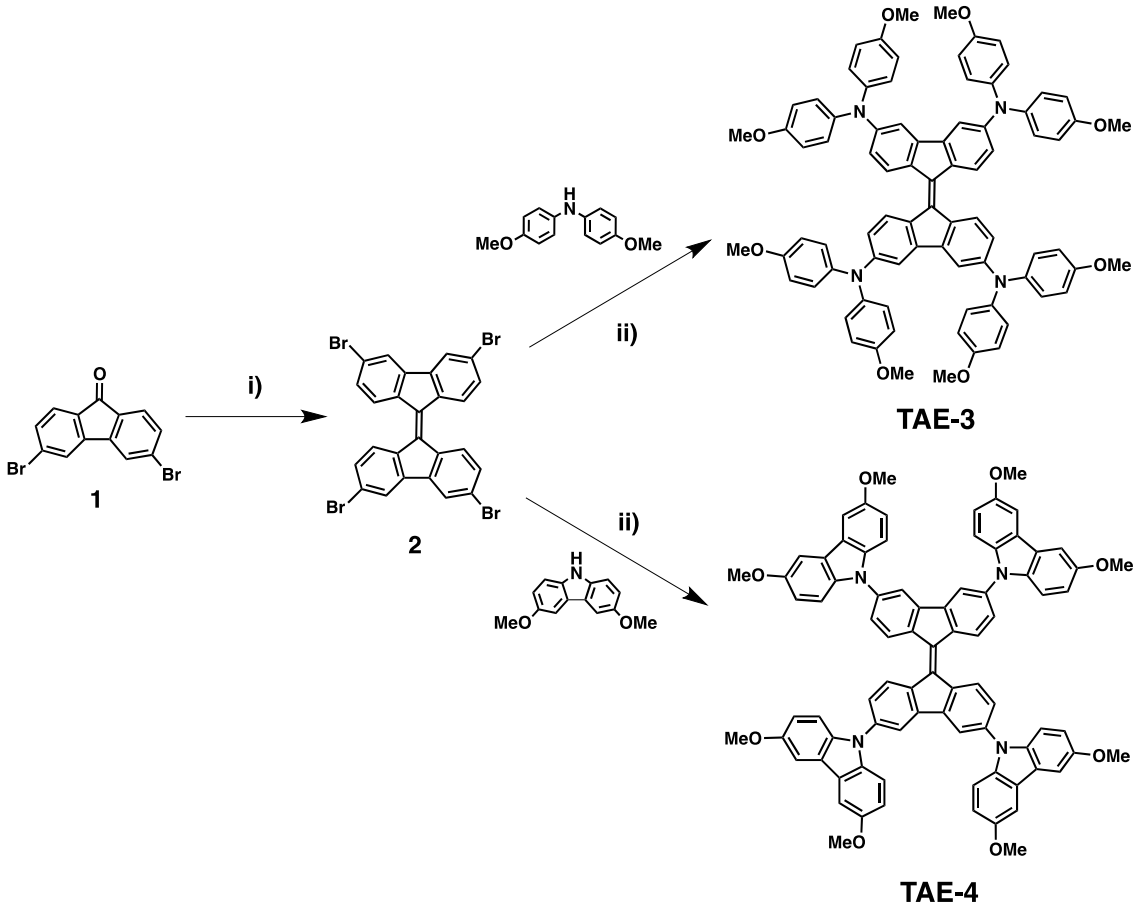

Scheme S1. Reagents and conditions: i) Lawesson's Reagent, toluene, 110°C; ii) *p*-Methoxydiphenylamine or 3,6-Dimethoxy-9H-carbazole , $Pd_2(dba)_3$, XPhos, Na^tBuO, toluene, 110 °C.

3,3',6,6'-Tetrakis [*N, N*-bis(4-methoxyphenyl) amino]-9,9'-bifluorenylidene, TAE-3

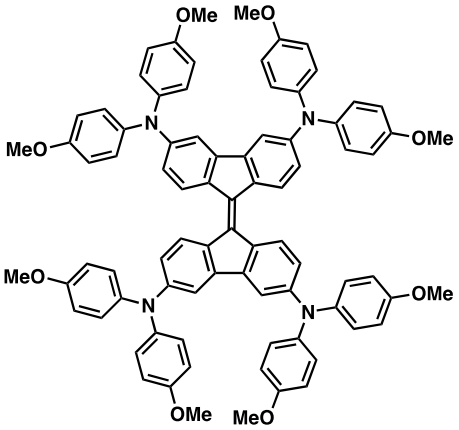

To a dry round bottom flask equipped with a stirrer bar, compounds **2** (100 mg, 0.16 mmol), *p*-Methoxydiphenylamine (178 mg, 0.78 mmol) XPhos (40 mg, 0.02 mmol) and $Pd_2(dba)_3$ (15 mg, 0.02 mmol) were dissolved in anhydrous toluene (35 mL). The resulting mixture was degassed for 30 minutes. Finally, Na^tBuO (82 mg, 0.85 mmol) was added to the solution which was heated to 100 °C for 3 hours. The reaction mixture was extracted with toluene (3 x 50 mL) and washed with water. The combined organic layers were dried over Na_2SO_4 and the solvent was removed under reduced pressure. The crude product was purified by column chromatography (silica gel, DCM and then 100:2 DCM/AcOEt). **TAE-3** was afforded as a blue solid which was washed several times with methanol, hexane and ether (124 mg, 0.10 mmol, 63 %).^{1}H NMR (400 MHz, THF-d_8, 298 K) δ: 7.92 (d, *J* = 8.7 Hz, 4H), 7.03 (d, *J* = 2.2 Hz, 4H), 6.96-6.82 (m, 16H), 6.77-6.64 (m, 16H), 6.54 (dd, *J* = 8.7, *J* = 2.2 Hz, 4H), 3.63 (s, 24H); ^{13}C NMR (175 MHz, $CDCl_3$, 298K) δ 155.7, 148.4, 141.2, 141.0, 132.4, 127.0, 126.3, 119.9, 114.7, 112.3, 55.5; FTIR (neat) ν: 3042, 2996, 2937, 2834, 1598, 1557, 1504, 1448, 1320, 1270, 1237, 1176, 1116, 1034, 825, 721, 575 cm^{-1}; HRMS [MALDI-TOF] calcd. for $C_{82}H_{68}N_4O_8$ [M$^+$], 1236.5032; found 1236.5029; elemental analysis calcd. for $C_{82}H_{68}N_4O_8$: C: 79.59, H: 5.54, N: 4.53; found C: 79.13, H: 5.70, N: 4.08.

3,3',6,6'-Tetrakis(3,6-dimethoxy-9H-carbazol-9-yl)-9,9'-bifluorenylidene, TAE-4.

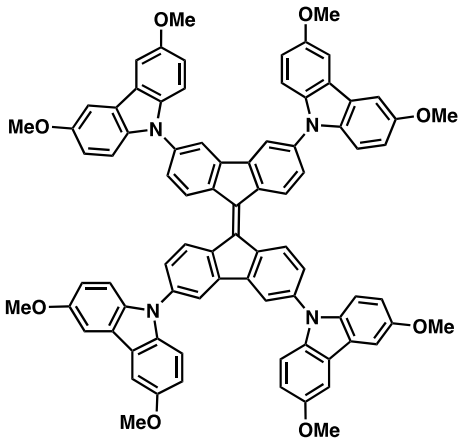

To a dry round bottom flask equipped with a stirrer bar, compounds **2** (100 mg, 0.16 mmol), 3,6-Dimethoxy-9H-carbazole (177 mg, 0.78 mmol), XPhos (37 mg, 0.08 mmol) and $Pd_2(dba)_3$ (14 mg, 0.02 mmol) were dissolved in anhydrous toluene (30 mL). The resulting mixture was degassed for 30 minutes. Finally, Na^tBuO (82 mg, 0.85 mmol) was added to the solution which was heated to 100 °C for 4 hours. The reaction mixture was extracted with toluene (3 x 50 mL) and washed with water. The combined organic layers were dried over Na_2SO_4 and the solvent was removed under reduced pressure. The crude product was purified by column chromatography (silica gel, $CHCl_3$ and then 25:1 $CHCl_3$/AcOEt) to afford **TAE-4** as a purple solid (122 mg, 0.10 mmol, 62 %), which was washed several times with methanol and hexane.^{1}H NMR (400 MHz, $CDCl_3$, 298 K) δ: 8.73 (d, *J* = 8.4 Hz, 4H), 7.95 (d, *J* = 1.9 Hz, 4H), 7.58 – 7.56 (m, 12H), 7.51 (d, *J* = 8.9 Hz, 8H), 7.07 (dd, *J* = 8.9, *J* = 2.5 Hz, 8H), 3.96 (s, 24H). ^{13}C NMR (100 MHz, $CDCl_3$, 298 K) δ: 154.5, 142.4, 139.4, 136.8, 136.0, 128.0, 125.2, 124.3, 118.0, 115.4, 111.0, 103.2, 56.4; FTIR (neat) ν: 2937, 2828, 1608, 1465, 1432, 1328, 1289, 1202, 1159, 1106, 1038, 913, 827, 788, 669, 585 cm^{-1}; HRMS [MALDI-TOF] calcd. for $C_{82}H_{60}N_4O_8$ [M$^+$], 1228.4406; found 1228.4446; elemental analysis calcd. for $C_{82}H_{60}N_4O_8$: C: 80.11, H: 4.92, N: 4.56; found C: 79.94, H: 5.04, N: 4.31.

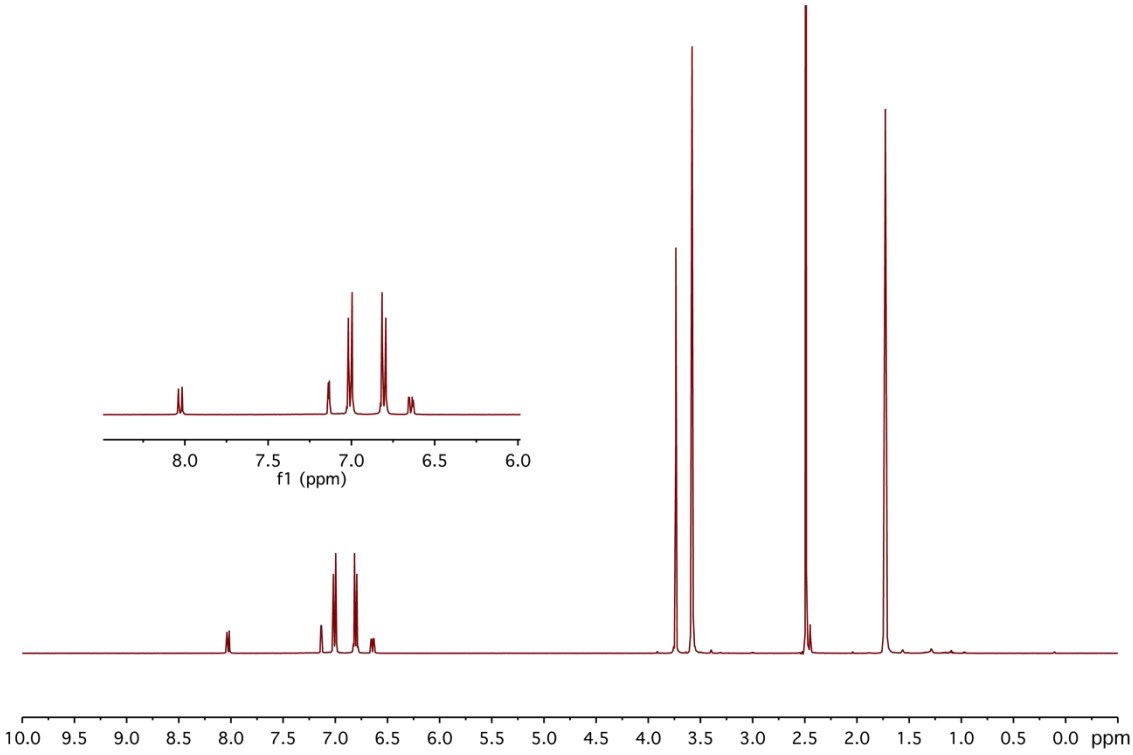

Figure S 1. ^{1}H NMR (400 MHz, THF-d_8, 298 K) of **TAE-3**.

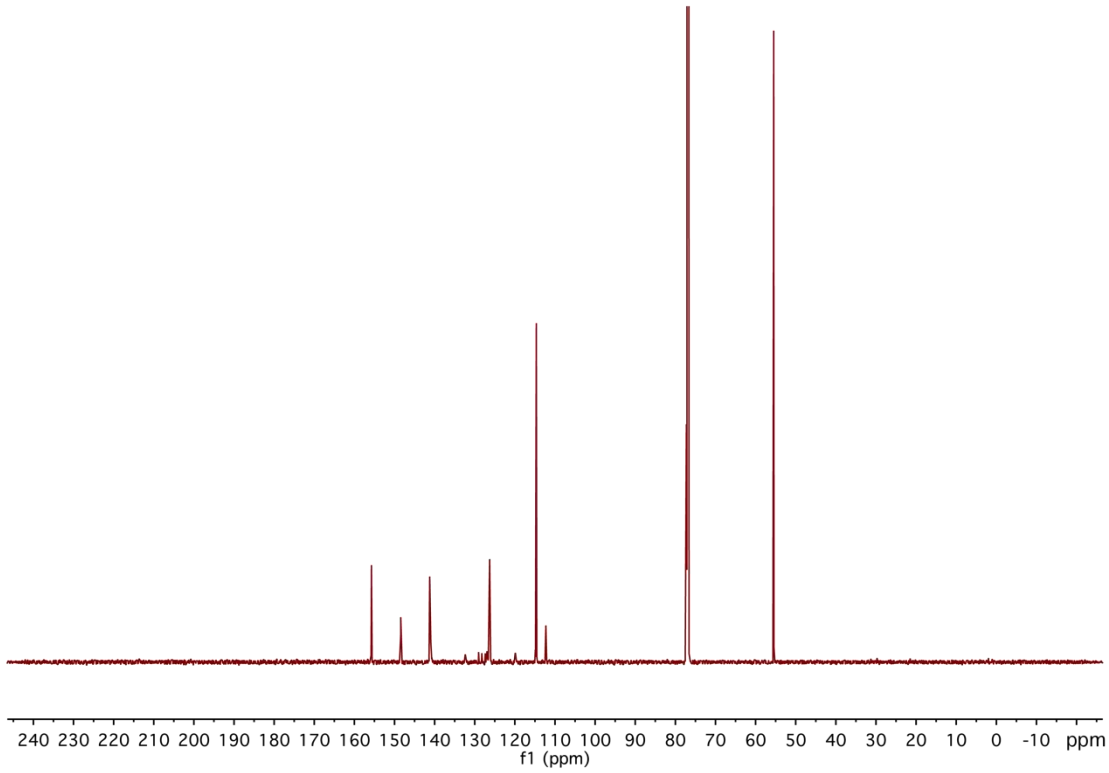

Figure S 2. ^{13}C NMR (175 MHz, $CDCl_3$, 298 K) of **TAE-3**.

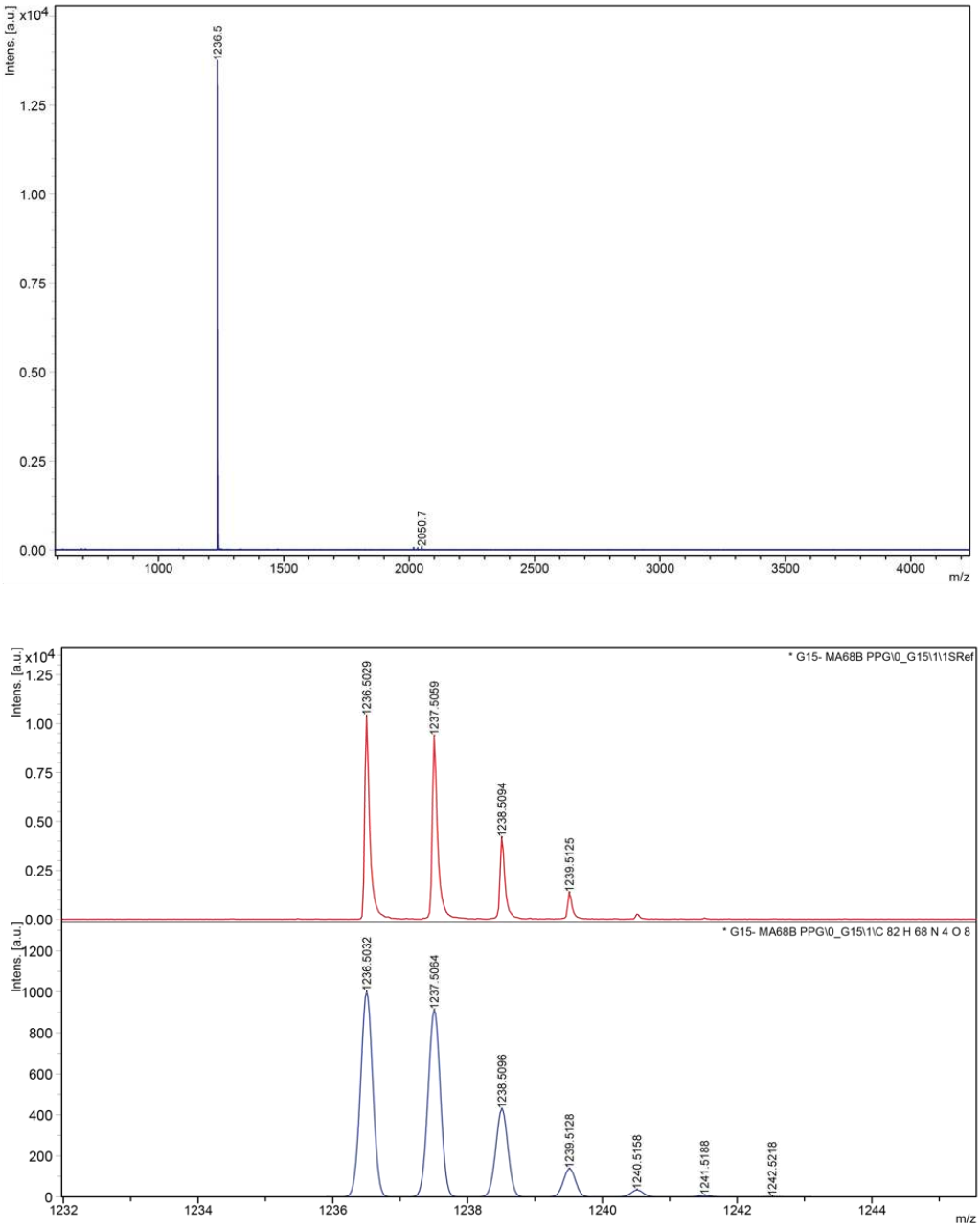

Figure S 3. HR-MALDI-TOF mass spectrum of **TAE-3**.

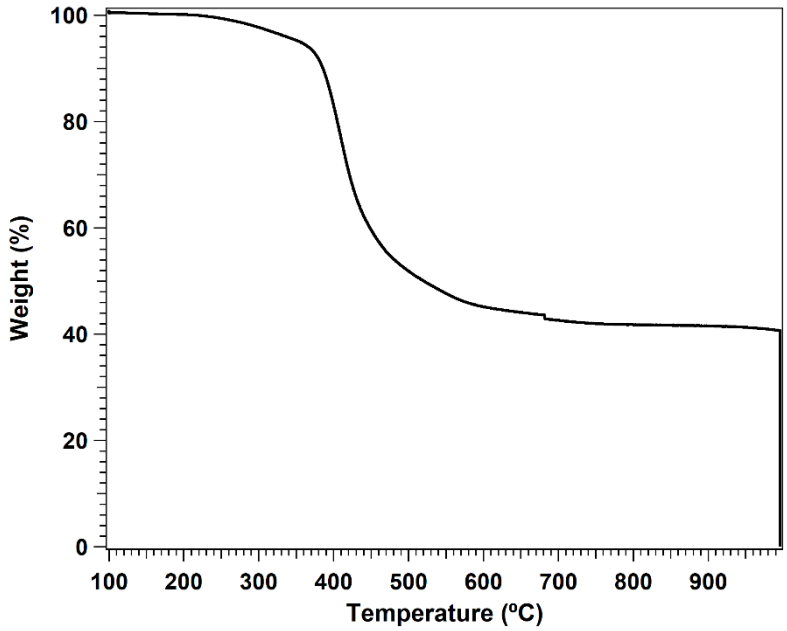

Figure S 4. Thermogravimetric Analysis of **TAE-3** at scan rate of 10 °C/min.

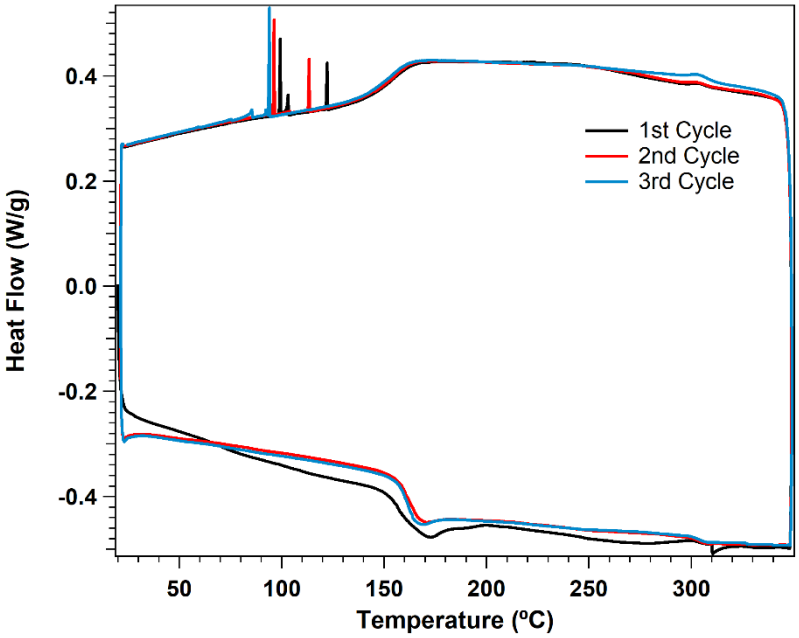

Figure S 5. Differential Scanning Calorimetry of **TAE-3** at scan rate of 20 °C/min.

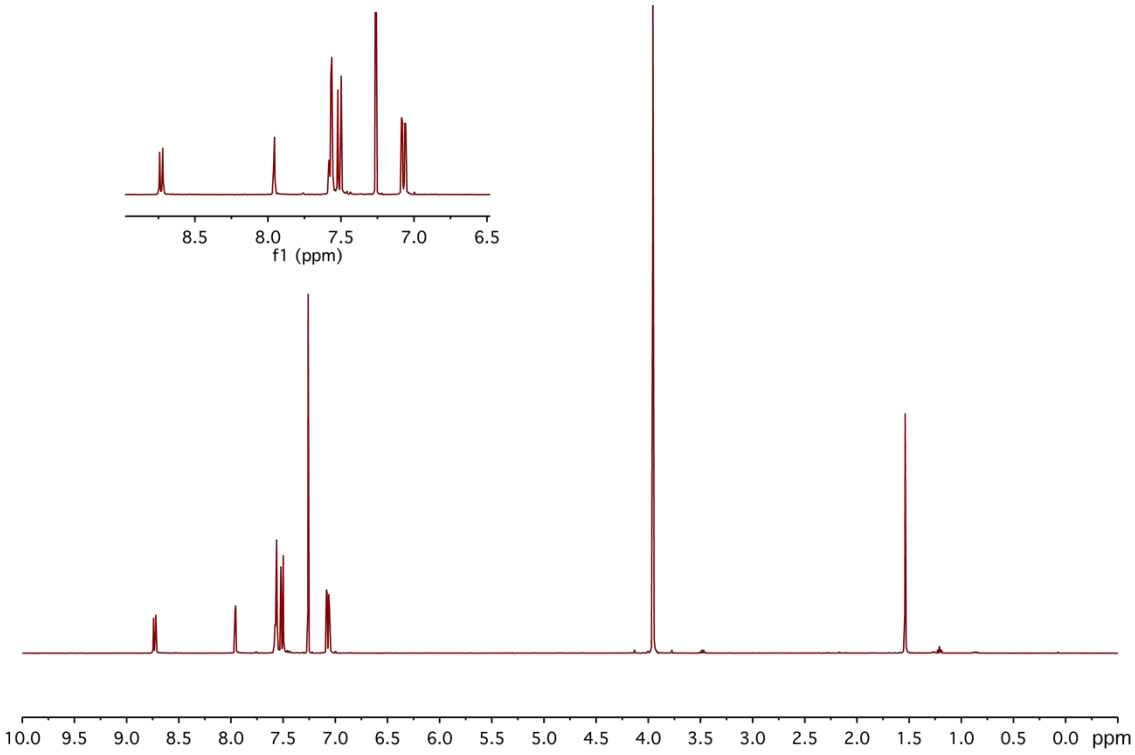

Figure S 6. ^{1}H NMR (400 MHz, $CDCl_3$, 298 K) of **TAE-4**.

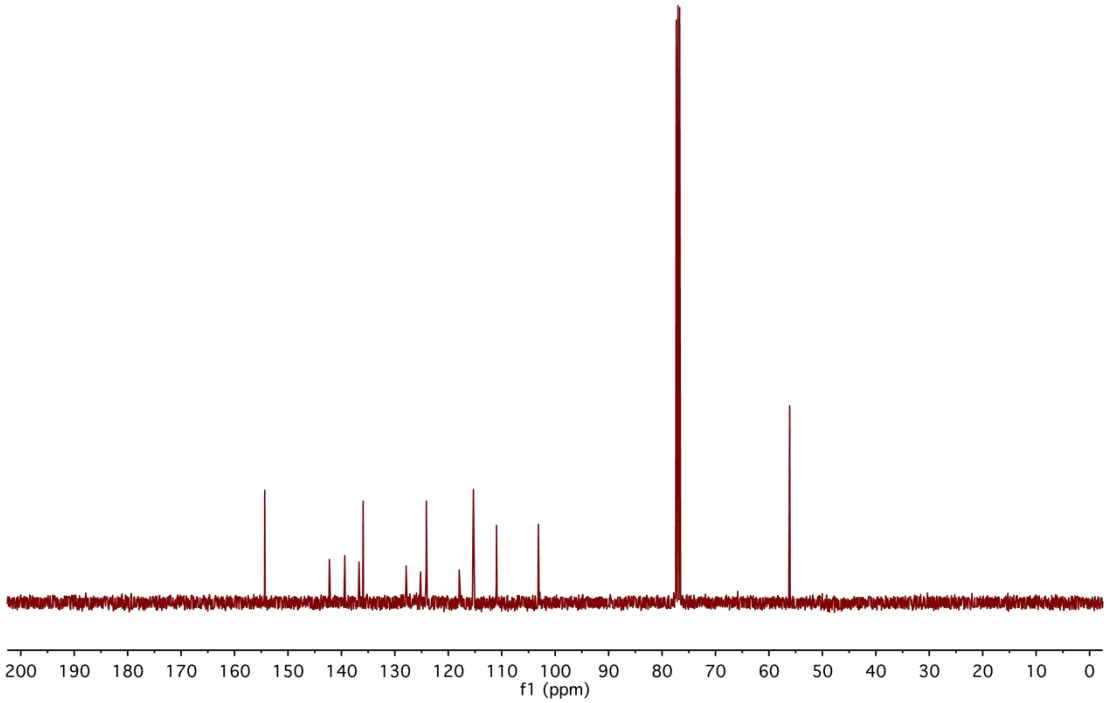

Figure S 7. ^{13}C NMR (100 MHz, $CDCl_3$, 298 K) of **TAE-4**.

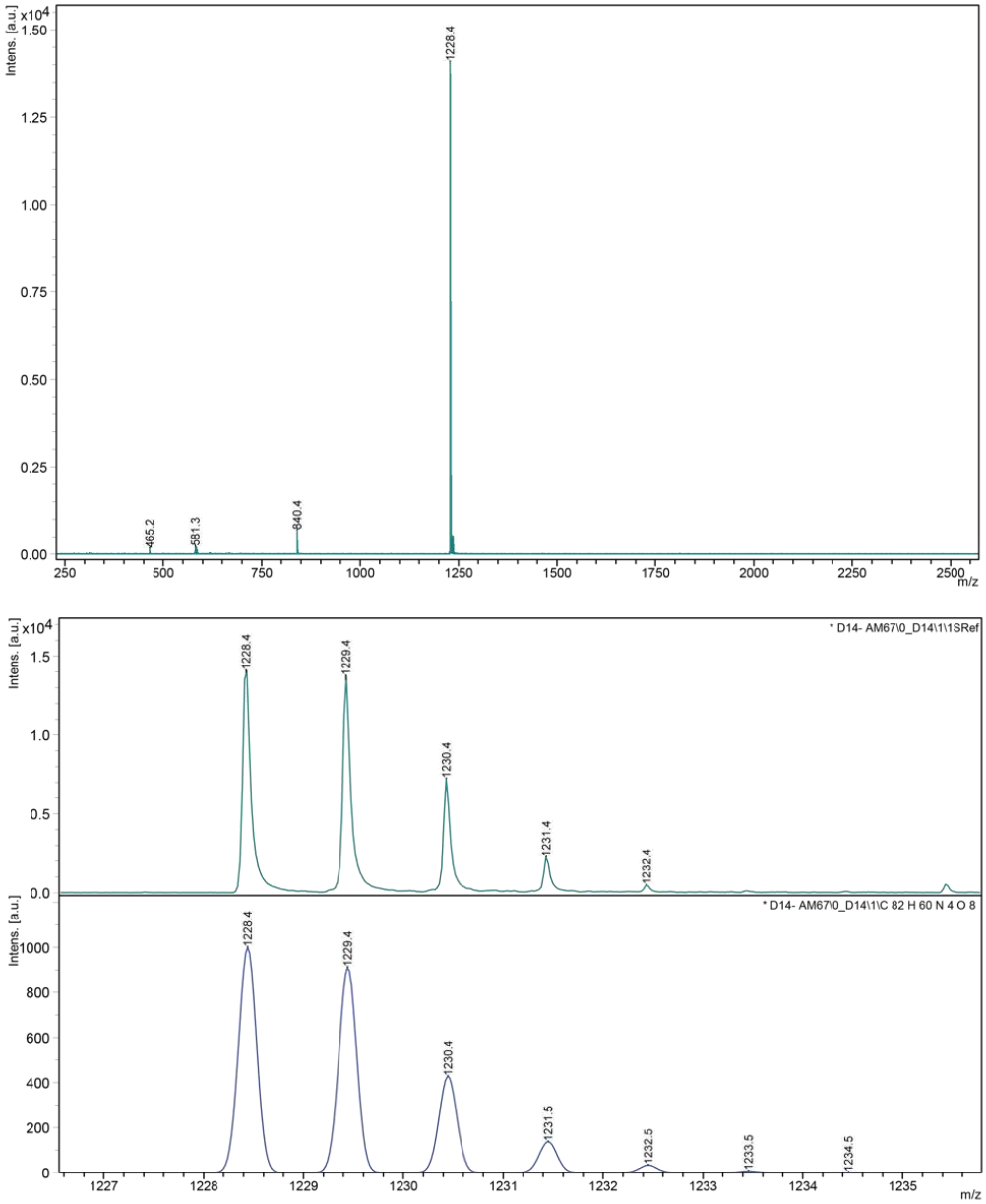

Figure S 8. HR-MALDI-TOF mass spectrum of **TAE-4**.

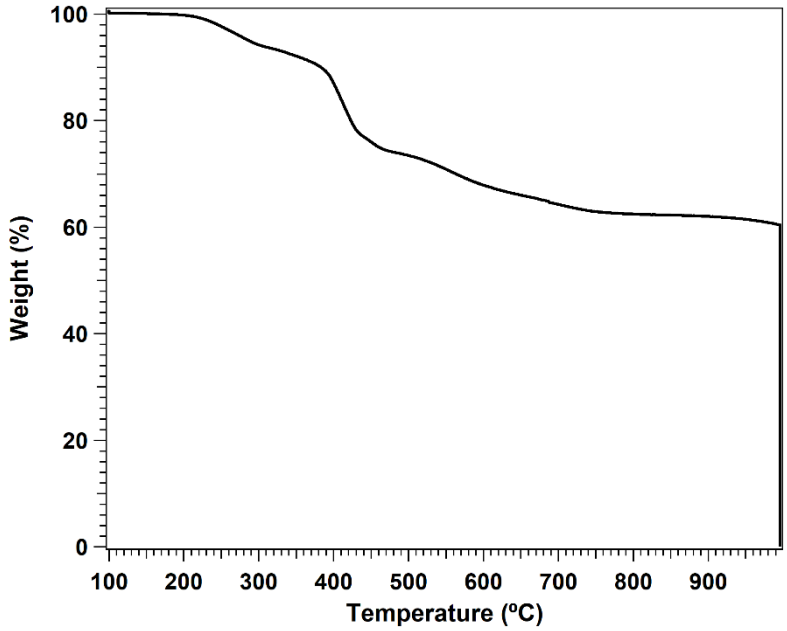

Figure S 9. Thermogravimetric Analysis of **TAE-4** at scan rate of 10 °C/min.

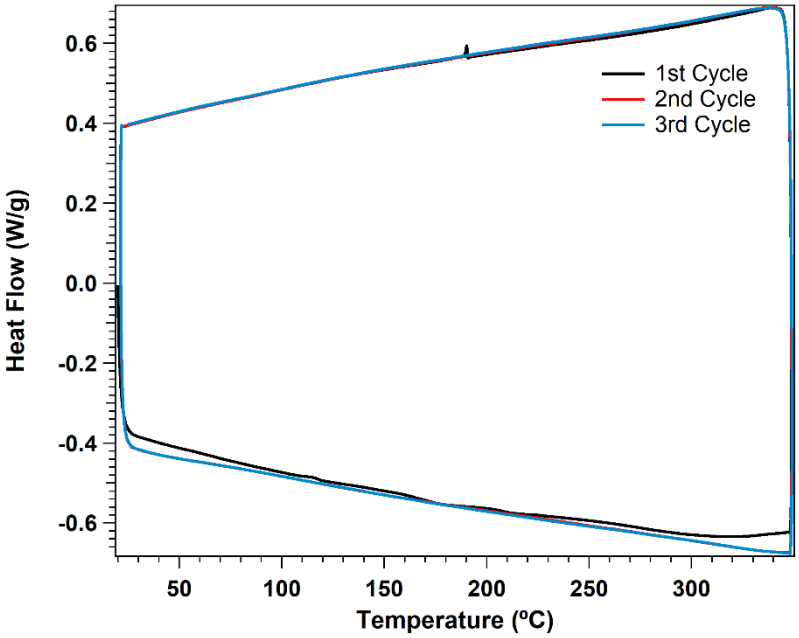

Figure S 10. Differential Scanning Calorimetry of **TAE-4** at scan rate of 20 °C/min.

3. Cyclic voltammograms in solution

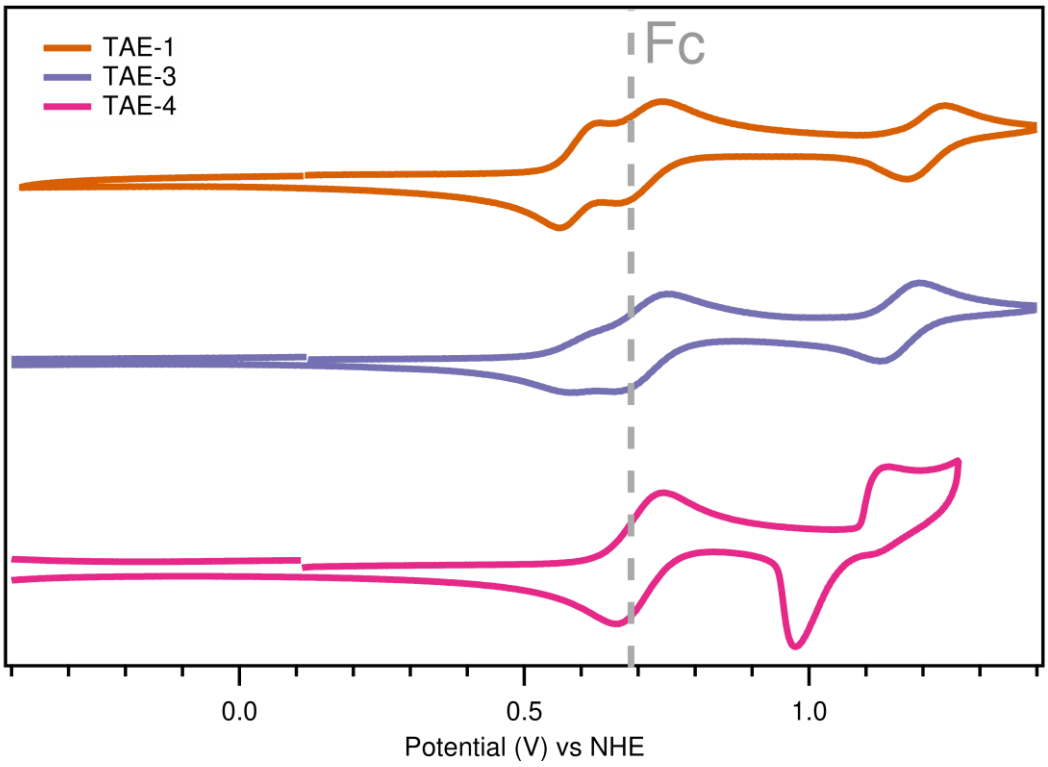

Figure S 11. Cyclic voltammogram of TAE-1, TAE-3 and TAE-4 in DCM including ferrocene and referred to NHE potential.

4. Space charge limited current mobility measurements

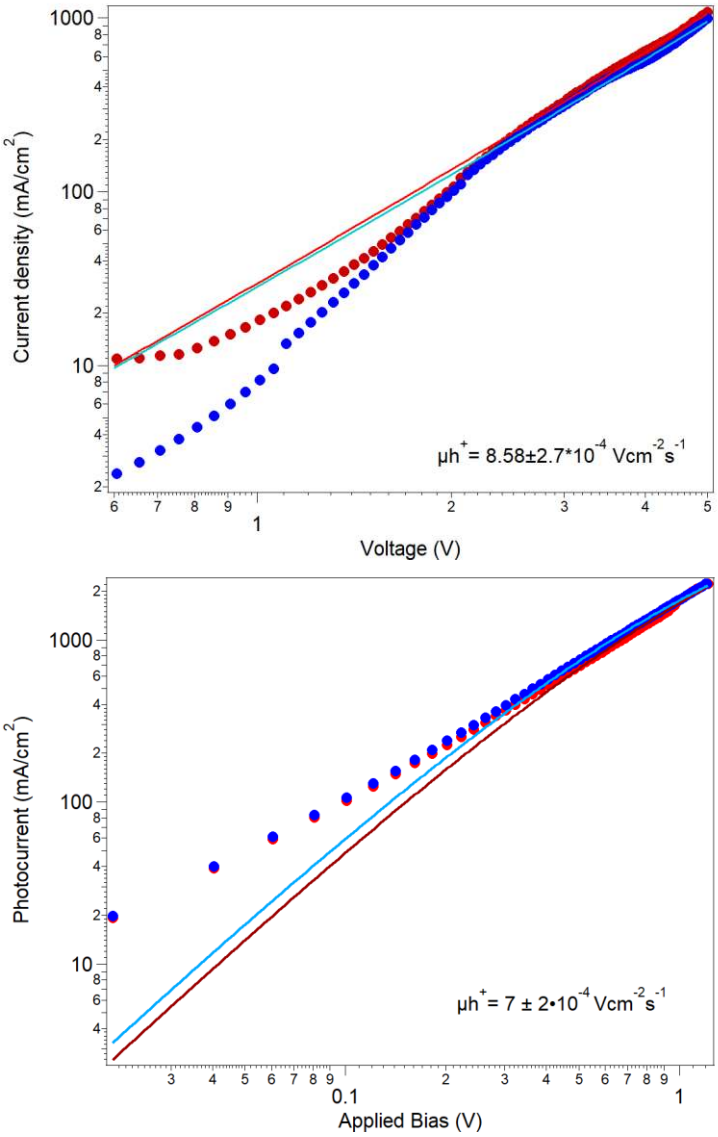

Figure S 12. Hole only (above) TAE-3 and (below) TAE-4 devices J-V at space charge limited conditions. The red symbols correspond to the measurement under illumination and the blue symbols correspond to the measurement in dark.

5. Simulated Molecular Orbitals

Table S 1. Simulated energies for HOMO and LUMO levels, their difference and the direct optical band gap as determined via Tauc plot of simulated absorbance spectra.

HTM	HOMO (eV)	LUMO (eV)	HOMO-LUMO gap (eV)	Optical BG (eV)
TAE-1	-5.61	-0.54	5.07	3.04
TAE-3	-5.54	-1.77	3.77	2.02
TAE-4	-6.14	-2.27	3.87	2.20

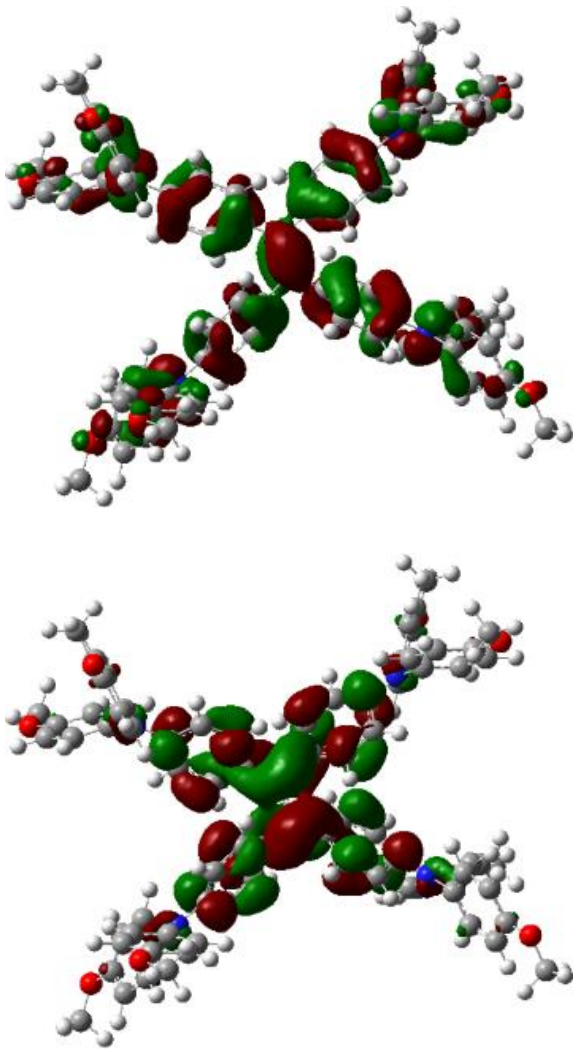

Figure S 13. Representation of the highest occupied (top) and lowest unoccupied (bottom) molecular orbitals (isovalue 0.02) for **TAE-1**.

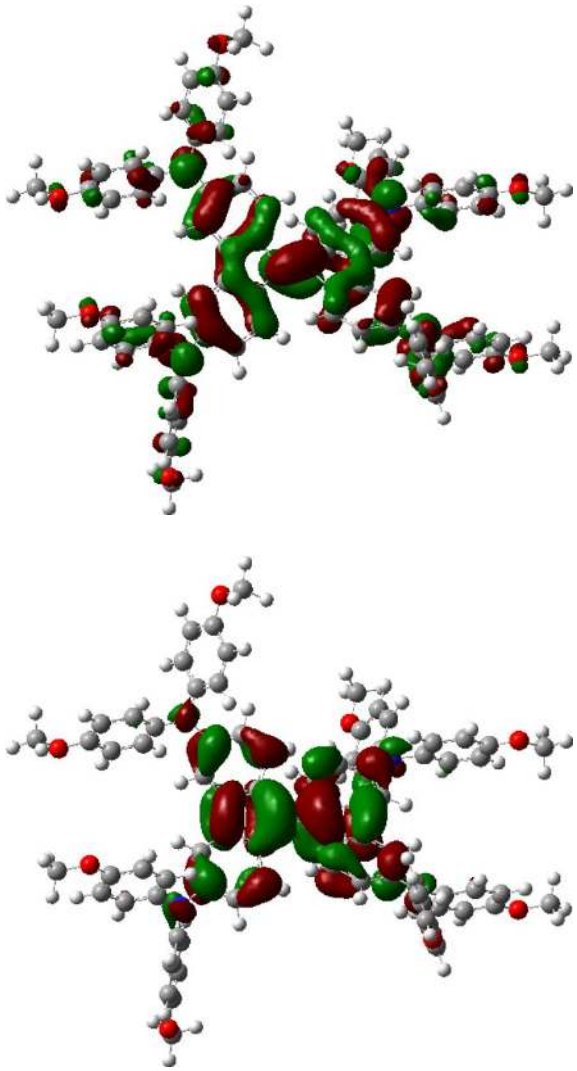

Figure S 14. Representation of the highest occupied (top) and lowest unoccupied (bottom) molecular orbitals (isovalue 0.02) for **TAE-3**.

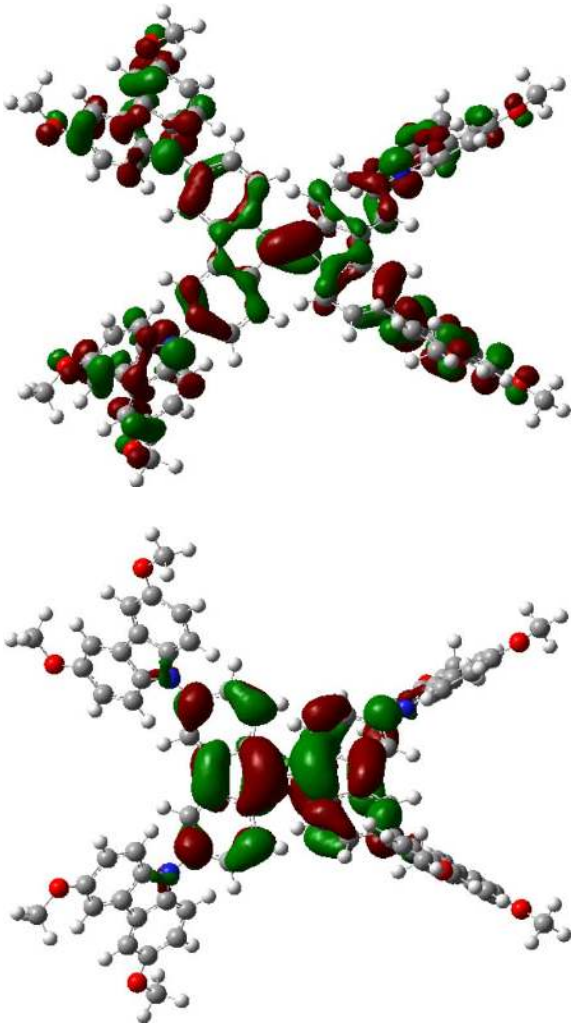

Figure S 15. Representation of the highest occupied (top) and lowest unoccupied (bottom) molecular orbitals (isovalue 0.02) for **TAE-4**.

6. Measured and Simulated UV-vis Absorbance Spectra

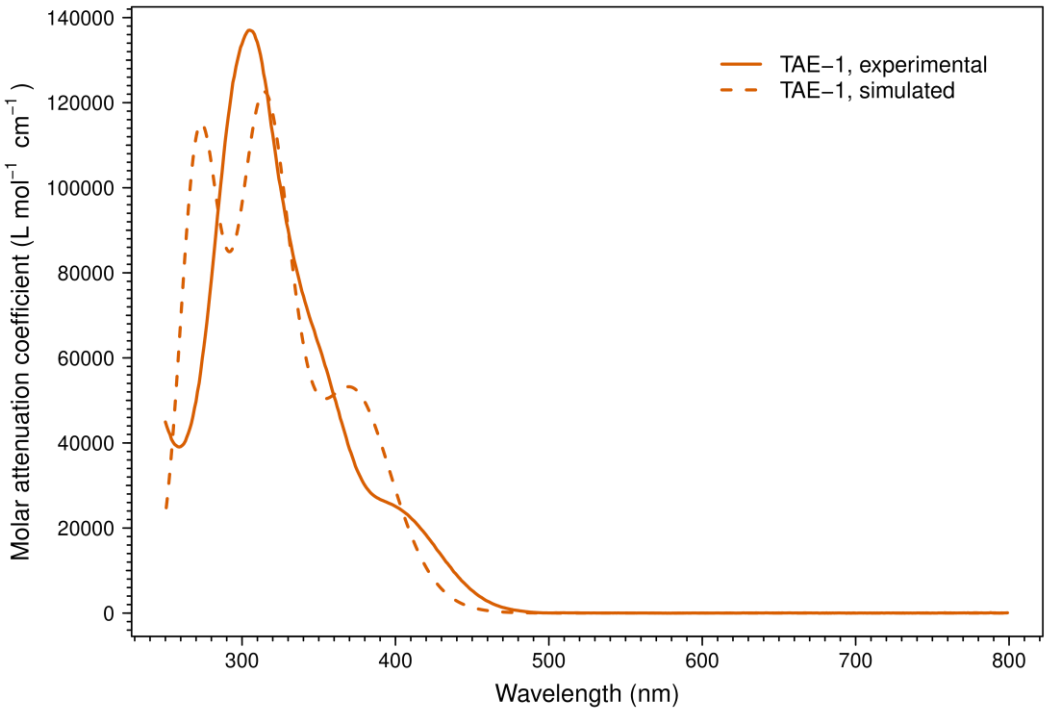

Figure S 16. Experimental (solid line) and simulated (dashed line, using a standard deviation for gaussian peaks of 4000 cm^{-1}) absorbance spectrum of **TAE-1** in THF solution.

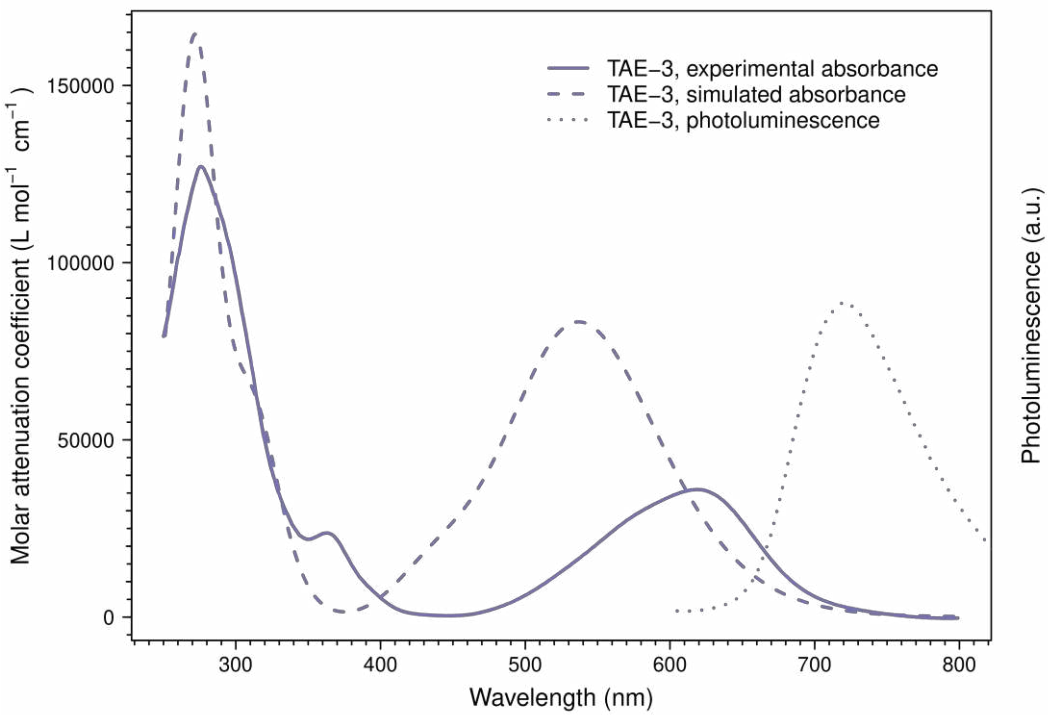

Figure S 17. Photoluminescence (dotted line, excitation wavelength 550 nm), experimental absorbance (solid line) and simulated absorbance (dashed line, using a standard deviation for gaussian peaks of 4000 cm^{-1}) spectrum of **TAE-3** in THF solution.

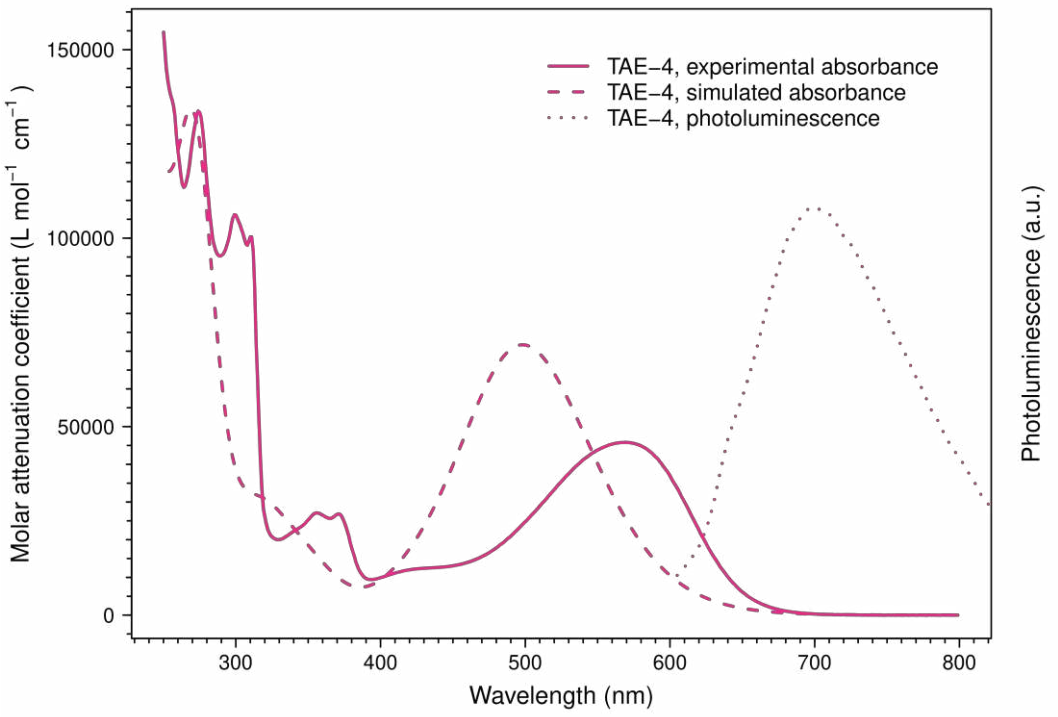

Figure S 18. Photoluminescence (dotted line, excitation wavelength 550 nm), experimental absorbance (solid line) and simulated absorbance (dashed line, using a standard deviation for gaussian peaks of 4000 cm^{-1}) spectrum of **TAE-4** in THF solution.

7. Determination of band gap from absorbance and photoluminescence

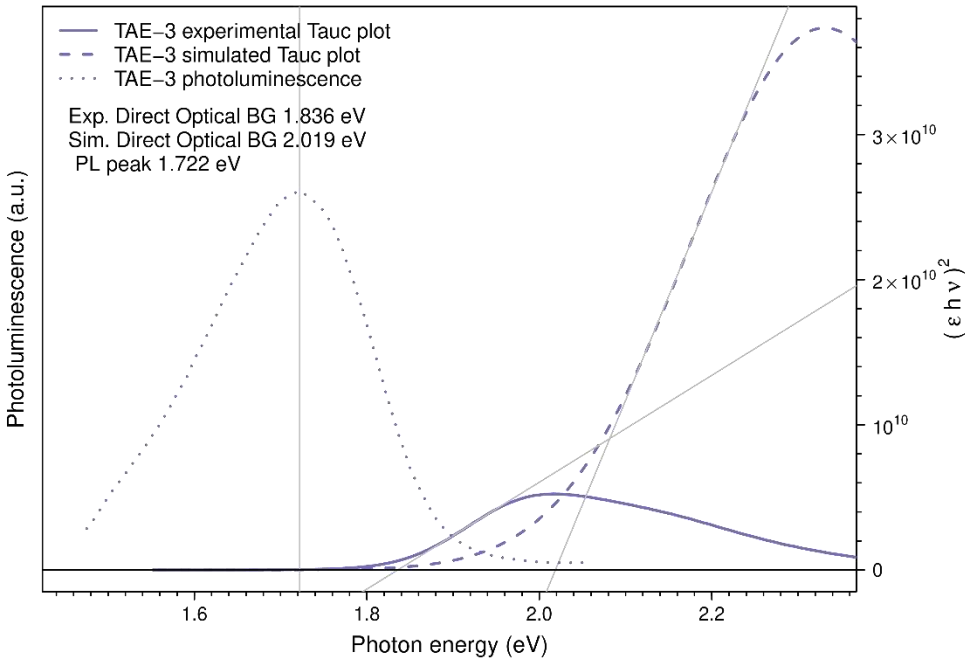

Figure S 19. Photoluminescence (dotted line, excitation wavelength 550 nm) and Tauc plot for direct optical band gap (solid line: from experimental absorbance; dashed line: from simulated absorbance) of **TAE-3** molecule in THF.

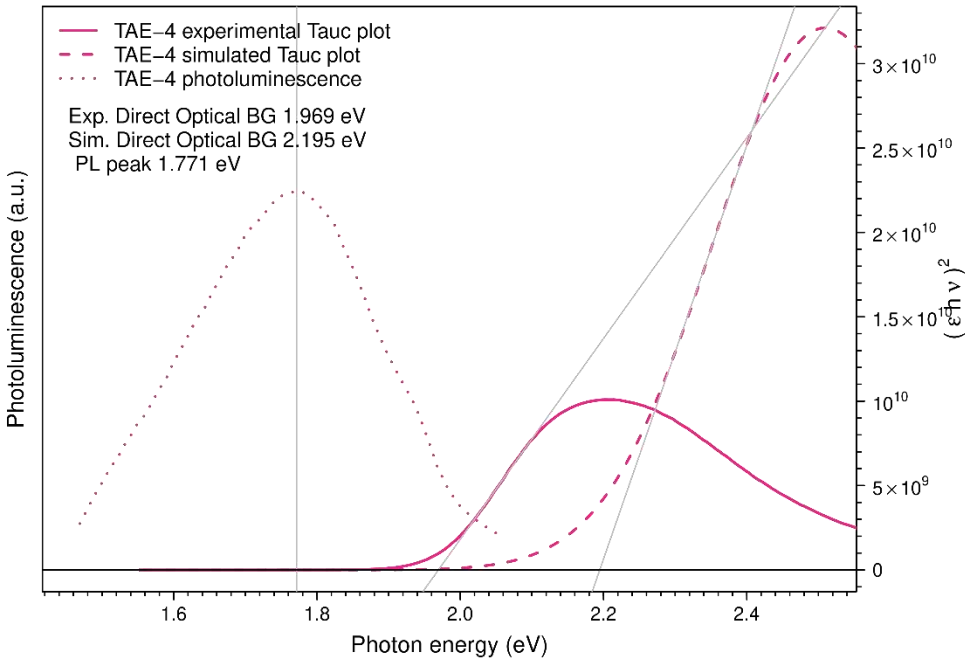

Figure S 20. Photoluminescence (dotted line, excitation wavelength 550 nm) and Tauc plot for direct optical band gap (solid line: from experimental absorbance; dashed line: from simulated absorbance) of **TAE-4** molecule in THF.

8. Surface Characterization via Alternating Current Atomic Force Microscopy (AC-AFM) and Environmental Scanning Electron Microscopy (ESEM) coupled with Energy-Dispersive X-ray analysis (EDX)

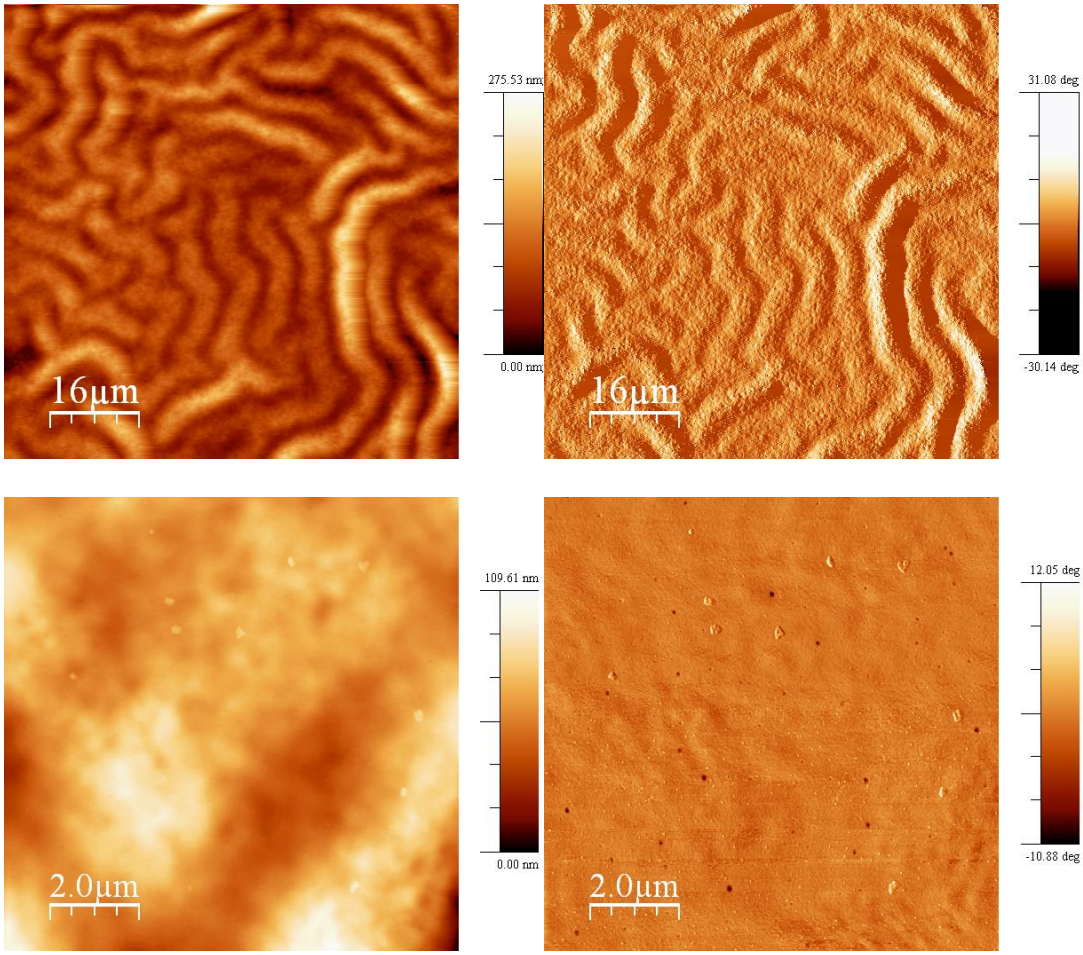

Figure S 21. AC-AFM images of spiro-OMeTAD surface in complete devices. Topography in the images on the left hand side and phase in the images on the right hand side. From the 80x80 micrometre area topography in the top image, a roughness average of Ra = 24 nm and a root mean square average roughness of RMS = 31 nm can be obtained. From the 10x10 micrometre area topography in the bottom image, a roughness average of Ra = 10 nm and a root mean square average roughness of RMS = 13 nm can be obtained.

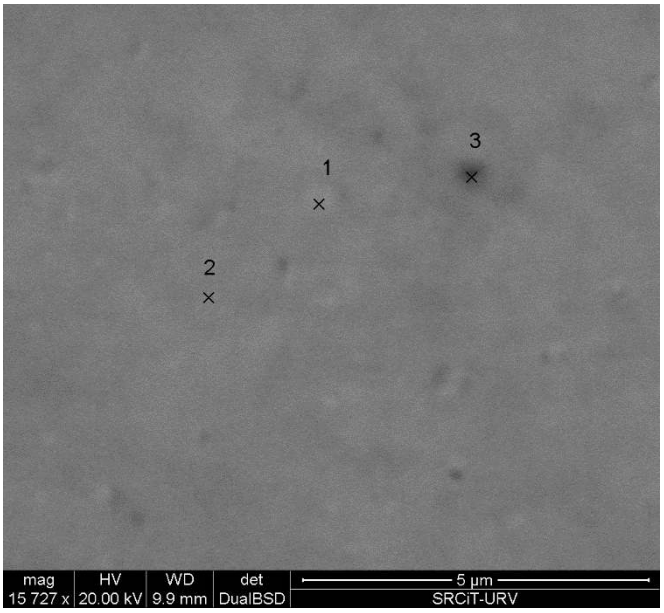

Figure S 22. ESEM imaging of the spiro-OMeTAD surface in a complete device. The three marked positions were analysed by EDX as reported in **Figure S 23**. The three locations were chosen as representative of the interesting features observed in the AC-AFM topography: position 1 is on an extruding feature, position 2 is in the flat surface and position 3 is in a hole.

Table S 2. Elemental analysis in atomic percentages as represented in Figure S 23 of the three points indicated in Figure S 22.

Element	C	O	Ti	Br	Sn	I	Pb
Position 1	30.12	16.29	2.53	4.29	13.61	24.52	8.64
Position 2	51.35	10.97	2.07	3.06	10.99	15.85	5.72
Position 3	45.74	14.34	2.47	2.89	13.91	15.32	5.35

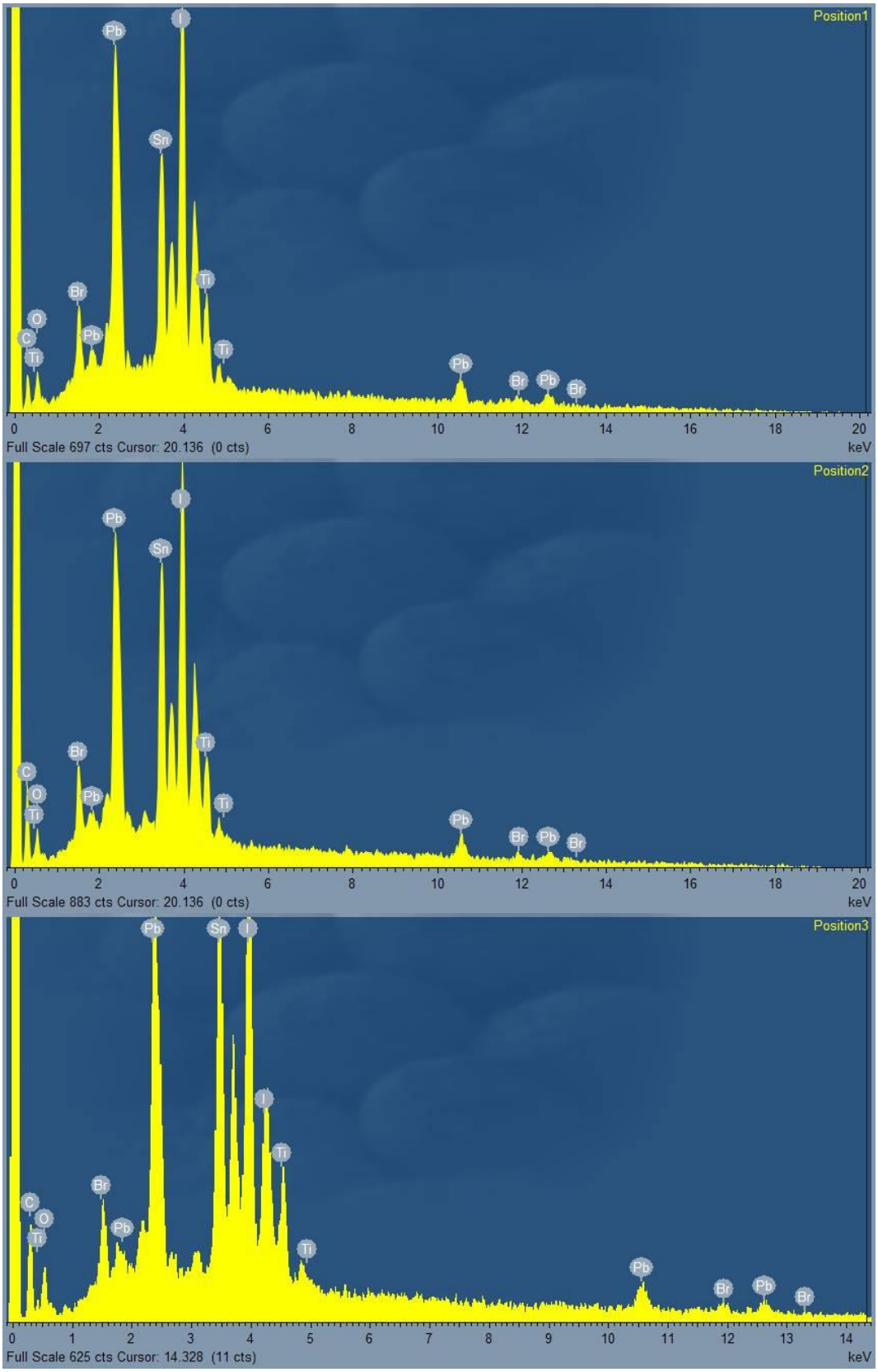

Figure S 23. EDX analysis of the three locations marked in Figure S 22. The elemental analysis is reported in Table S 2.

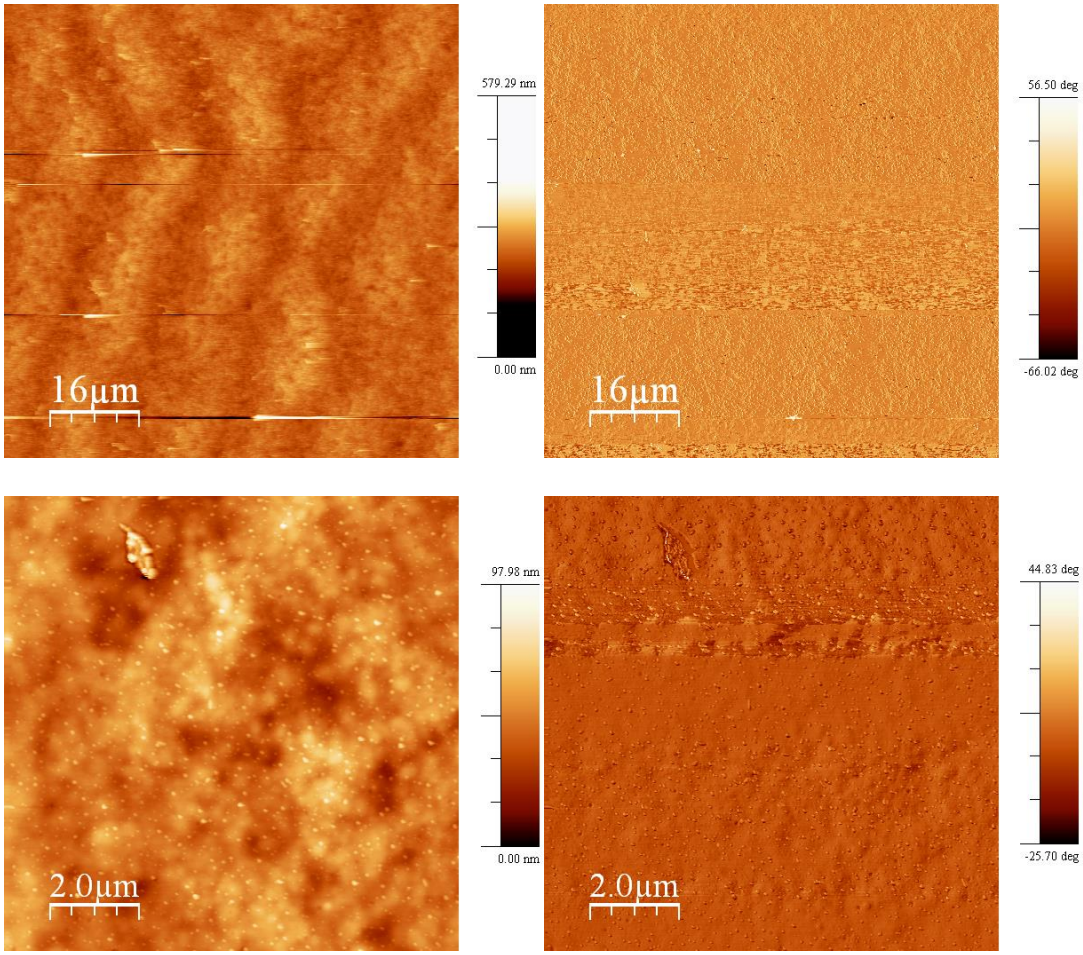

Figure S 24. AC-AFM images of TAE-1 surface in complete devices. Topography in the images on the left hand side and phase in the images on the right hand side. From the 80x80 micrometre area topography in the top image, a roughness average of Ra = 20 nm and a root mean square average roughness of RMS = 30 nm can be obtained. From the 10x10 micrometre area topography in the bottom image, a roughness average of Ra = 8 nm and a root mean square average roughness of RMS = 10 nm can be obtained.

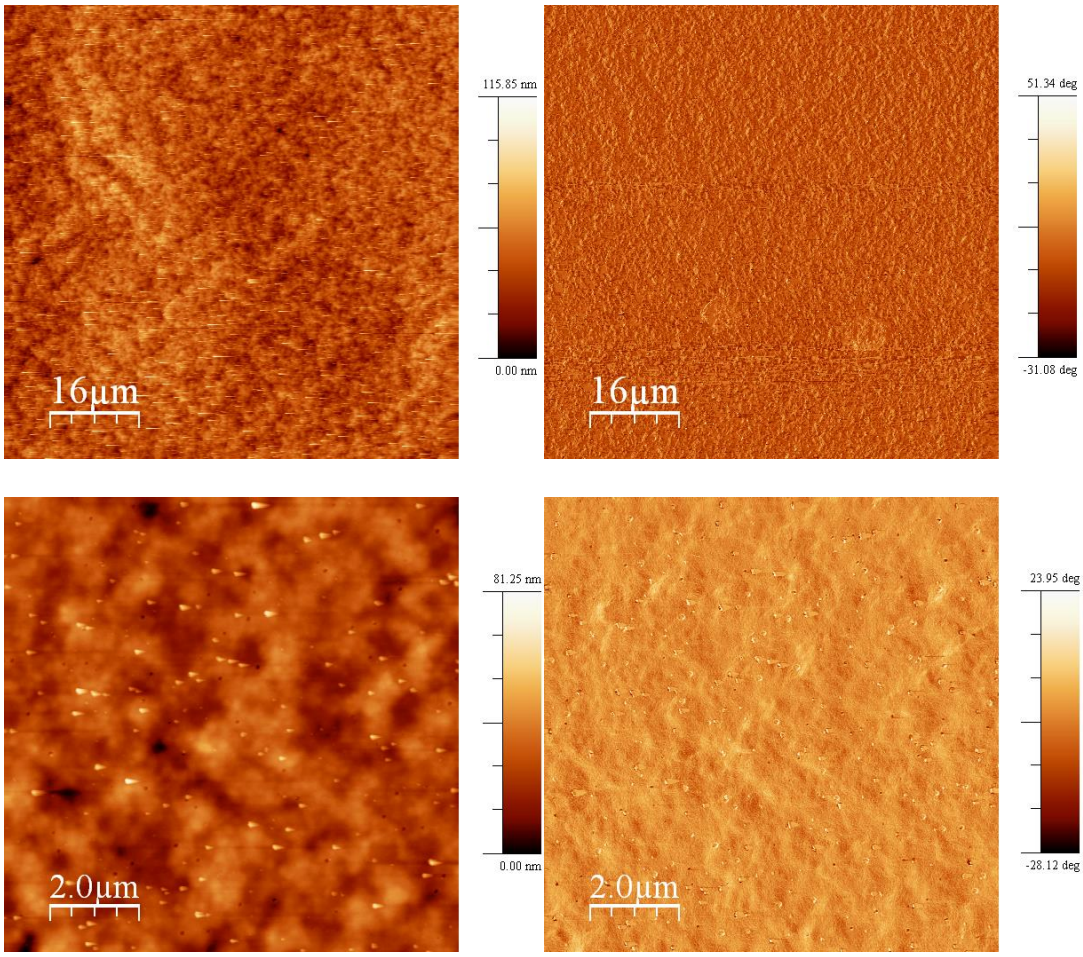

Figure S 25. AC-AFM images of TAE-3 surface in complete devices. Topography in the images on the left hand side and phase in the images on the right hand side. From the 80x80 micrometre area topography in the top image, a roughness average of Ra = 8 nm and a root mean square average roughness of RMS = 10 nm can be obtained. From the 10x10 micrometre area topography in the bottom image, a roughness average of Ra = 6 nm and a root mean square average roughness of RMS = 8 nm can be obtained.

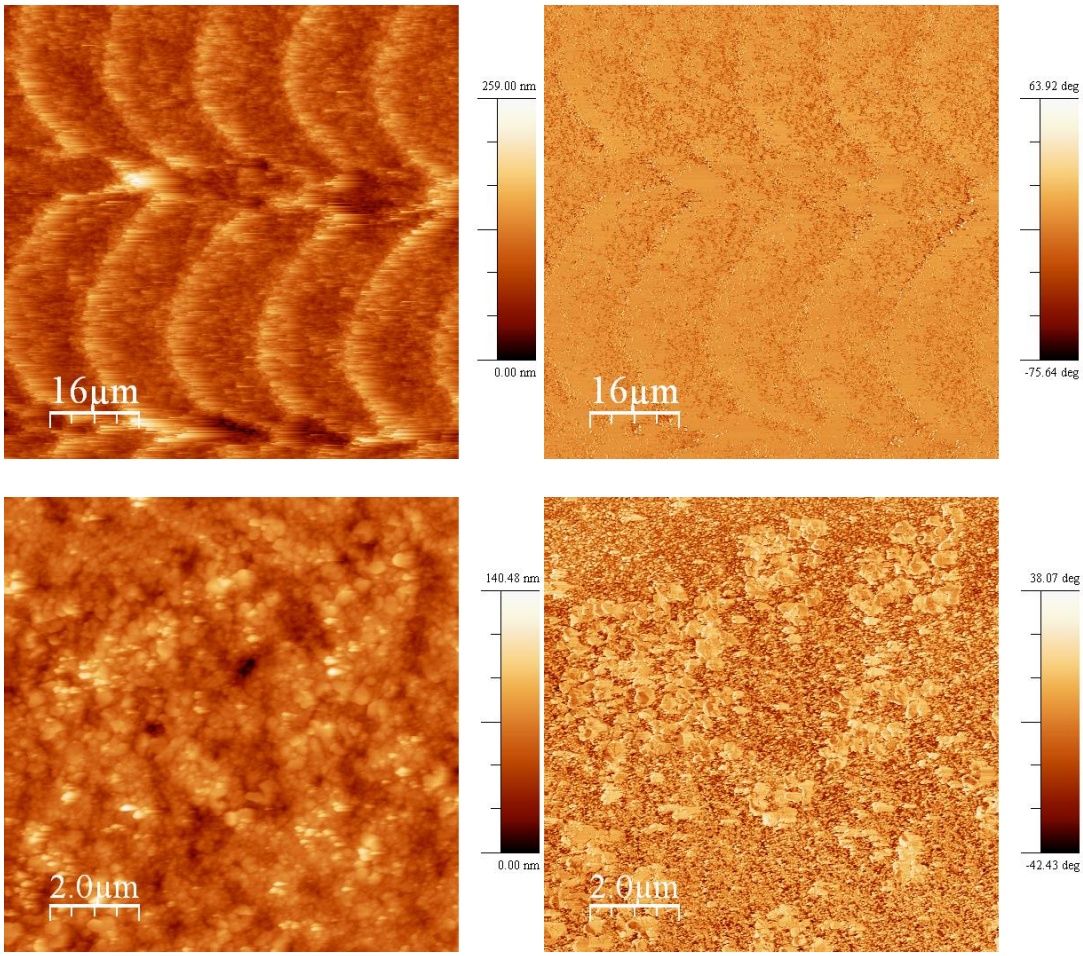

Figure S 26. AC-AFM images of TAE-4 surface in complete devices. Topography in the images on the left hand side and phase in the images on the right hand side. From the 80x80 micrometre area topography in the top image, a roughness average of Ra = 18 nm and a root mean square average roughness of RMS = 22 nm can be obtained. From the 10x10 micrometre area topography in the bottom image, a roughness average of Ra = 12 nm and a root mean square average roughness of RMS = 15 nm can be obtained.

9. XRD analysis of complete devices

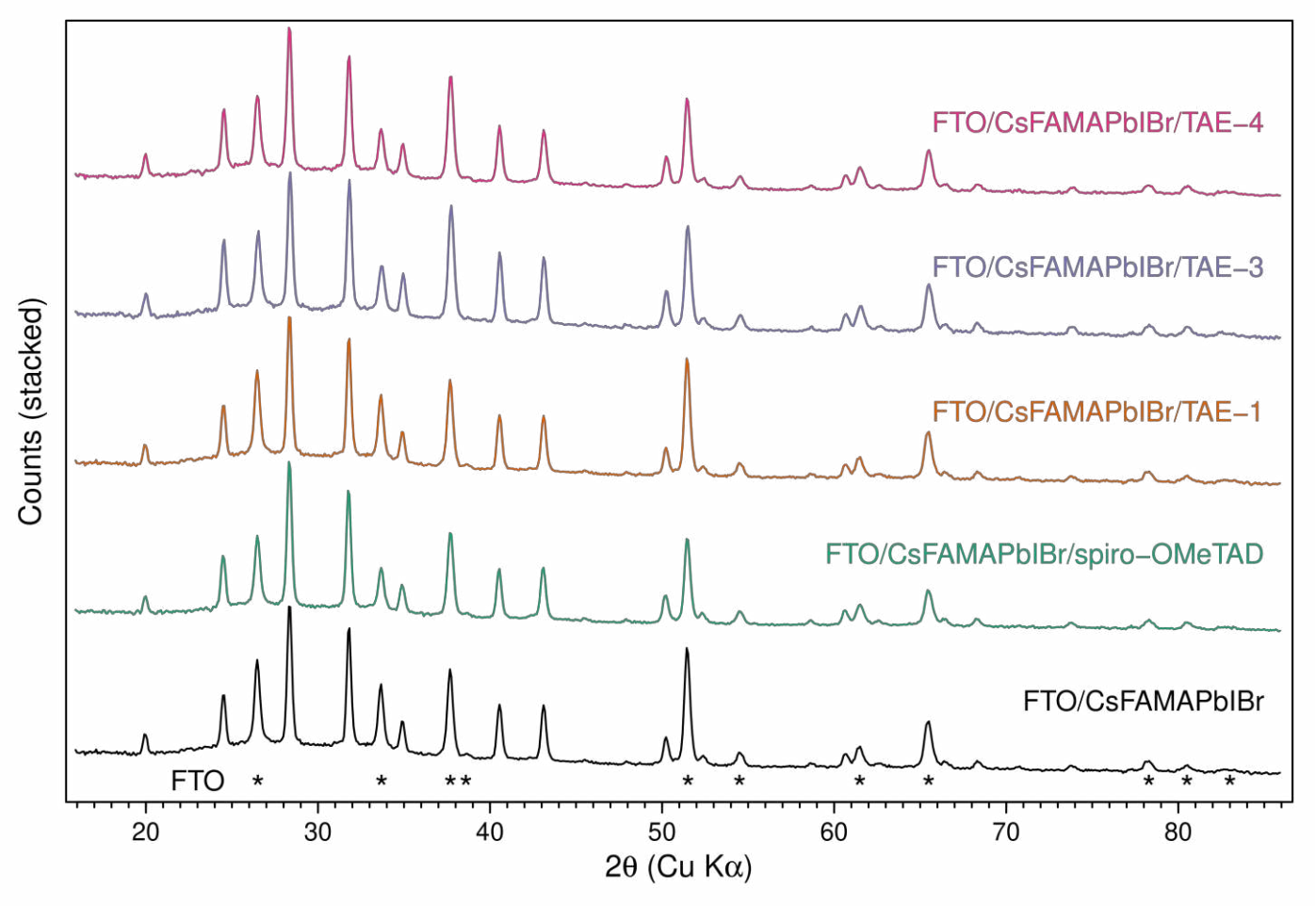

Figure S 27. The XRD pattern measured on complete devices avoiding the area covered with the gold electrode. The amorphous HTMs, the very think titanium oxide layer, and the gold are not visible in the diffraction pattern. The FTO peaks are visible and marked with an * asterisk. The perovskite pattern is identical to the Cs5 reference pattern from [16]. The diffraction pattern of the devices have been measured at least 8 months after their fabrication. The fact that no significant difference can be observed between the perovskite below any of the HTMs and the uncovered perovskite, supports the absence of chemical reactivity between the HTMs and the perovskite layer.

10. Perovskite Layer Thickness Evaluation via Elevation Profile Measurement

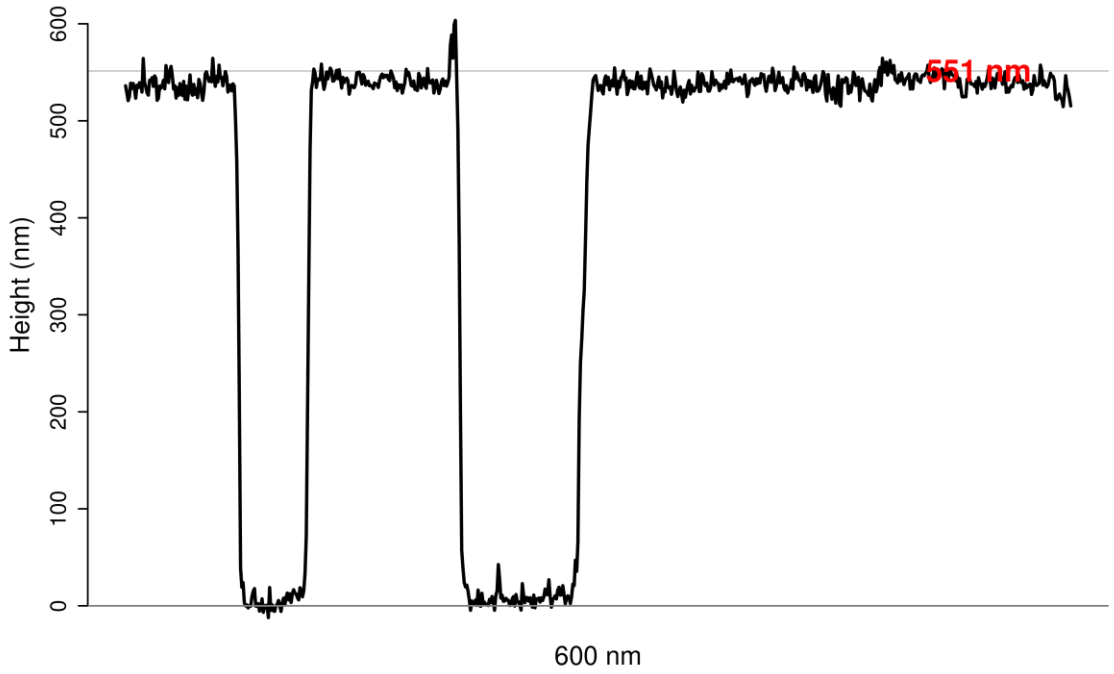

Figure S 28. The elevation profile of a mechanically furrowed perovskite layer not covered by any HTM. The underlying dense titanium oxide layer is hard enough to not be scratched. The measurement was performed with a calibrated stylus profilometer.

11. Cross-sectional characterization via Scanning Electron Microscopy (SEM)

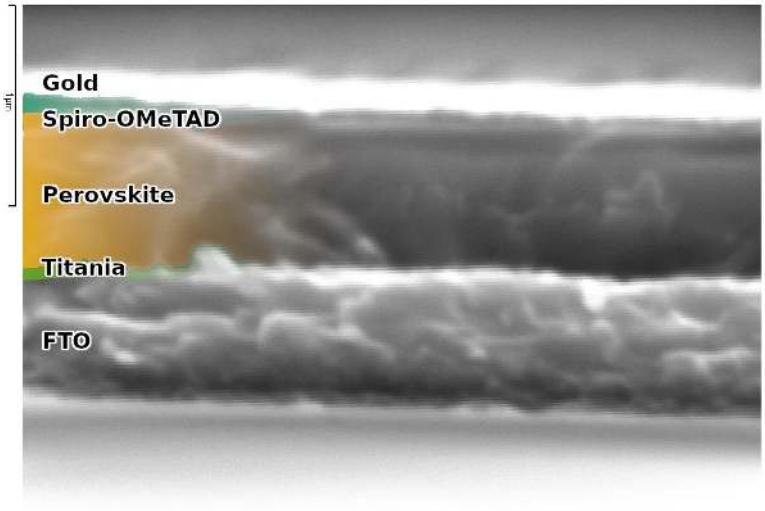

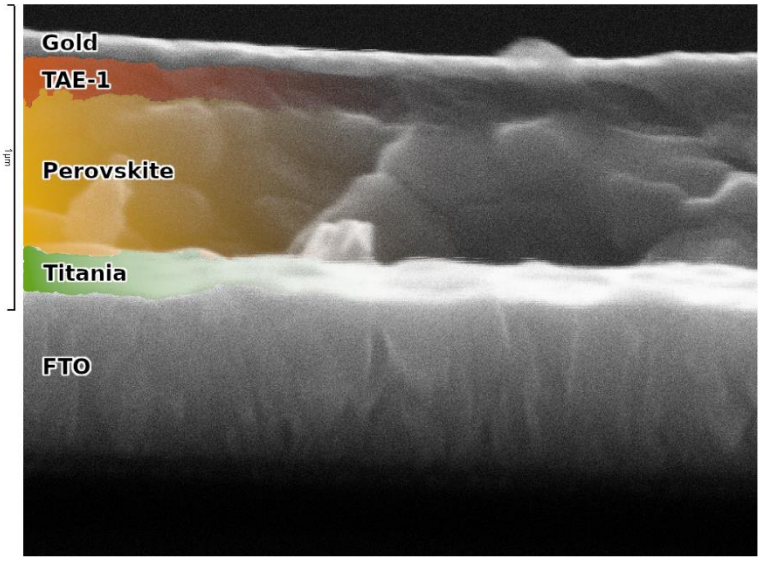

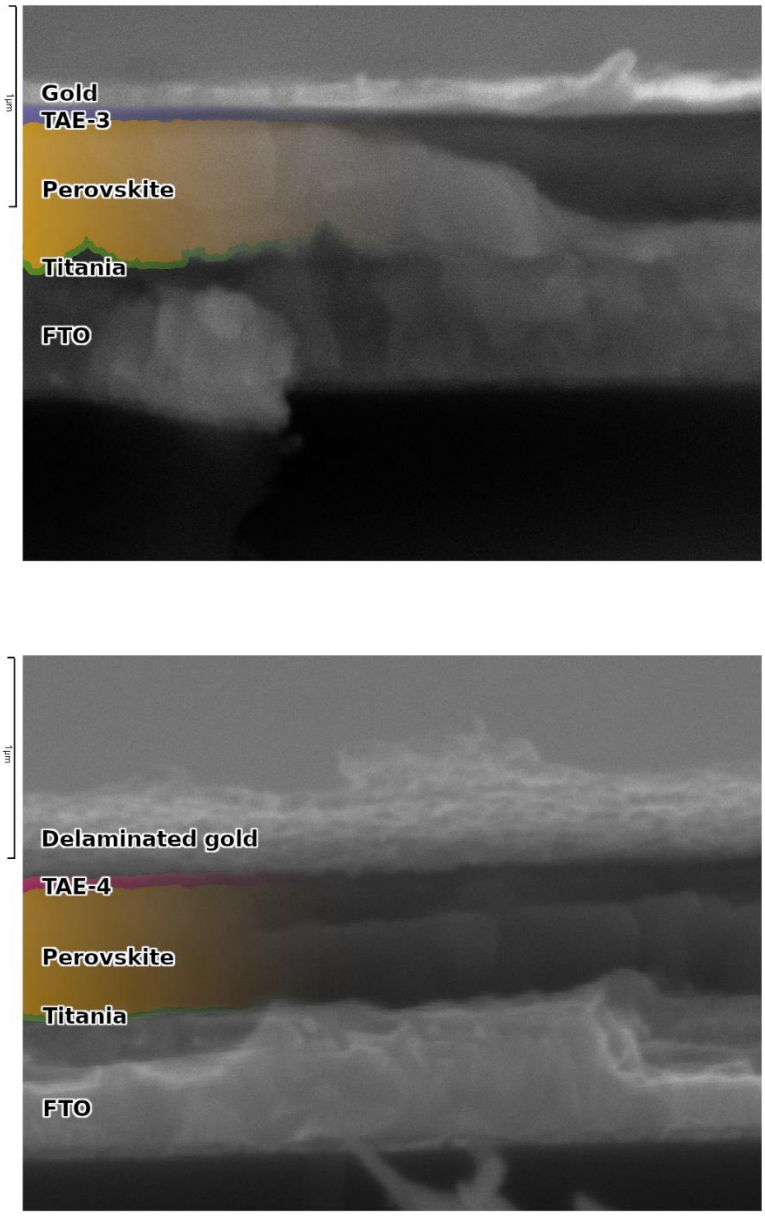

Figure S 29. Cross-section images acquired with an ESEM equipment at high vacuum and 20 kV accelerated electron beam. Full devices with spiro-OMeTAD (first), TAE-1 (second), TAE-3 (third) and TAE-4 (fourth). The scale bar corresponds to 1 µm.

12. Device statistics

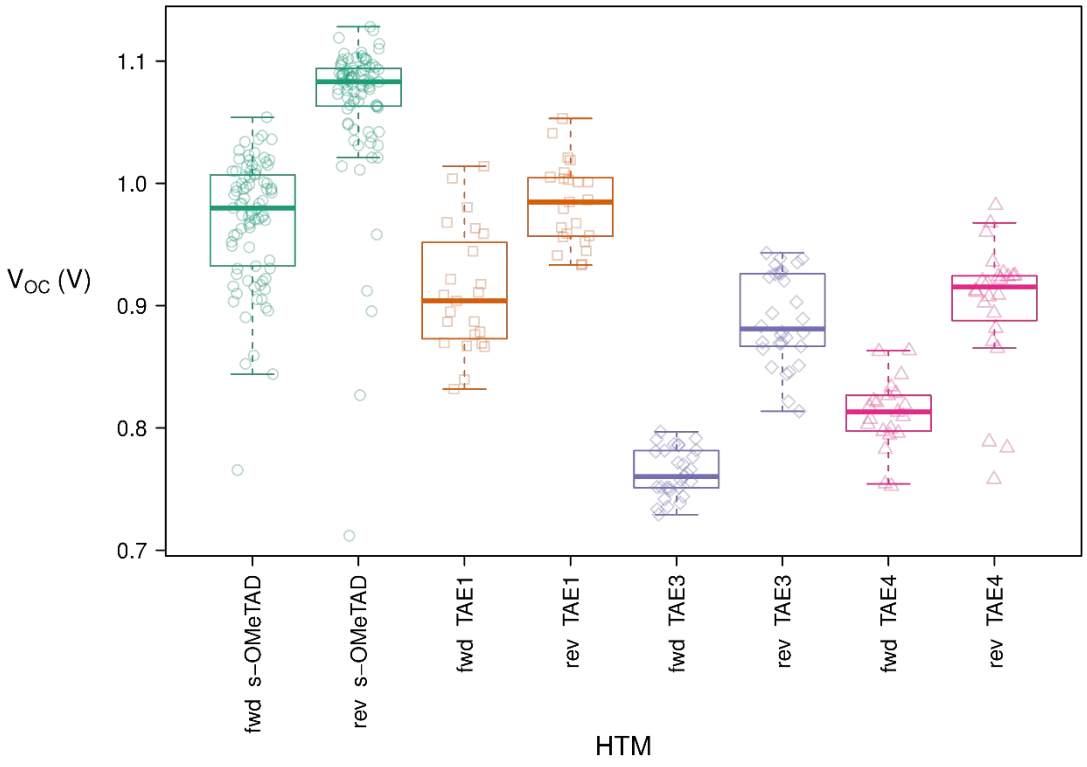

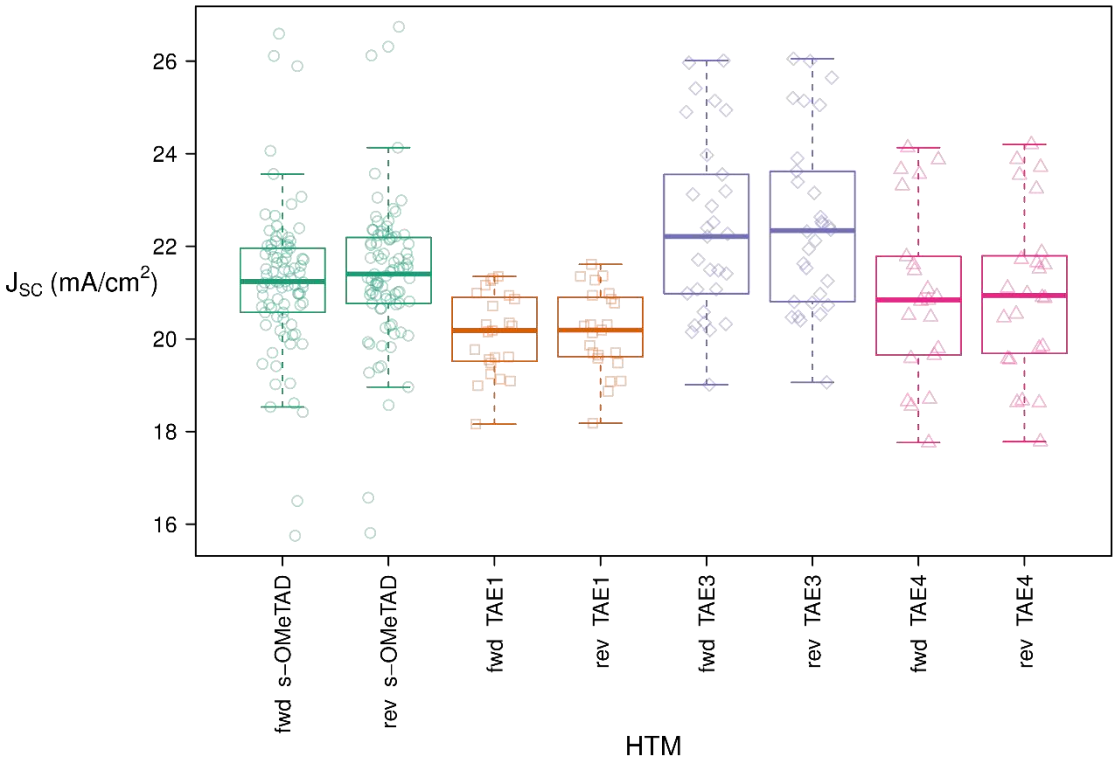

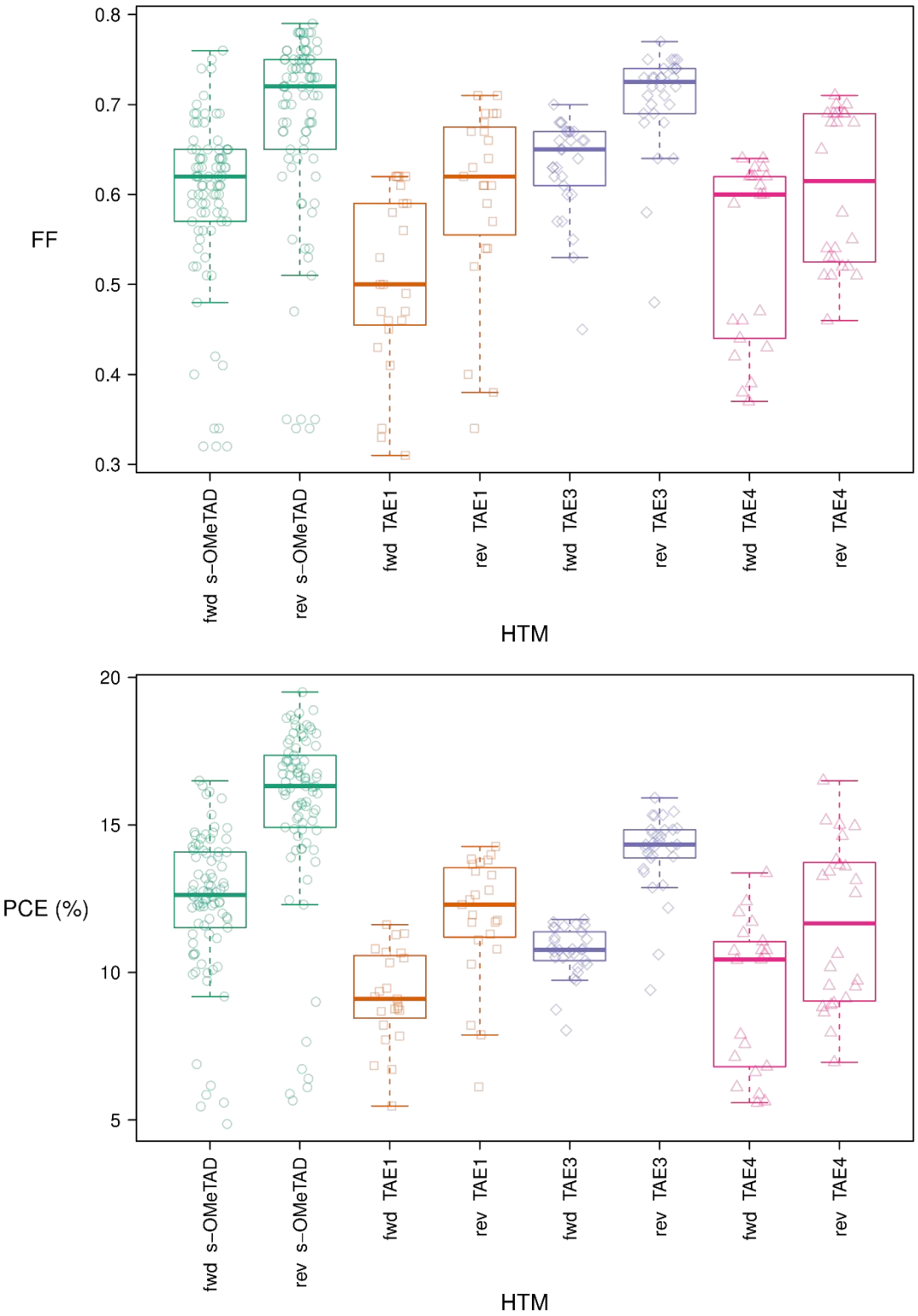

Figure S 30. Device statistics (from top to bottom: open circuit voltage, short circuit current, fill factor, power conversion efficiency) for all devices of spiro-OMeTAD (85 independent diodes), TAE-1 (23 independent diodes), TAE-3 (29 independent diodes) and TAE-4 (21 independent diodes) used in this study.

13. Forward and Reverse Current-voltage Scans for Champion Devices

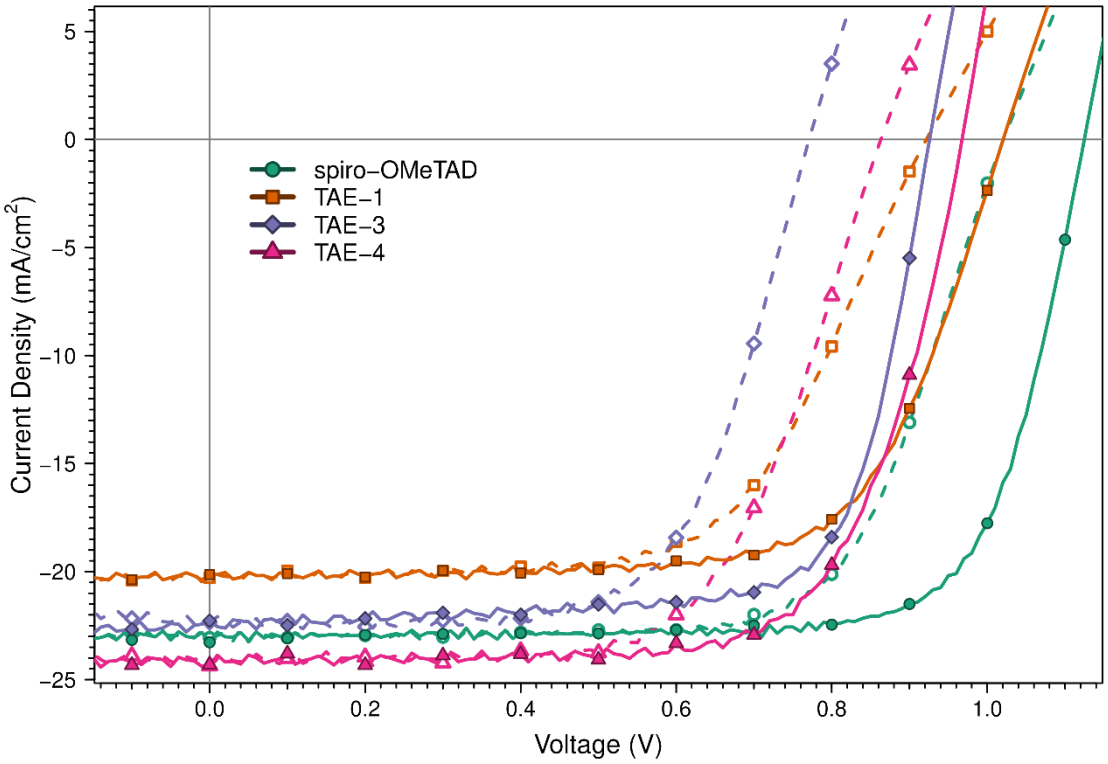

Figure S 31. Forward (dashed) and reverse (solid) current-voltage curves for the most efficient spiro-OMeTAD (green), TAE-1 (orange), TAE-3 (purple) and TAE-4 (magenta) devices. All devices were measured using same conditions (illumination at AM 1.5, 0.6 V/s). The noise observed in the profile is mainly caused by small fluctuations in the illumination intensity.

14. Current-voltage Scans at Different Sweep Speeds

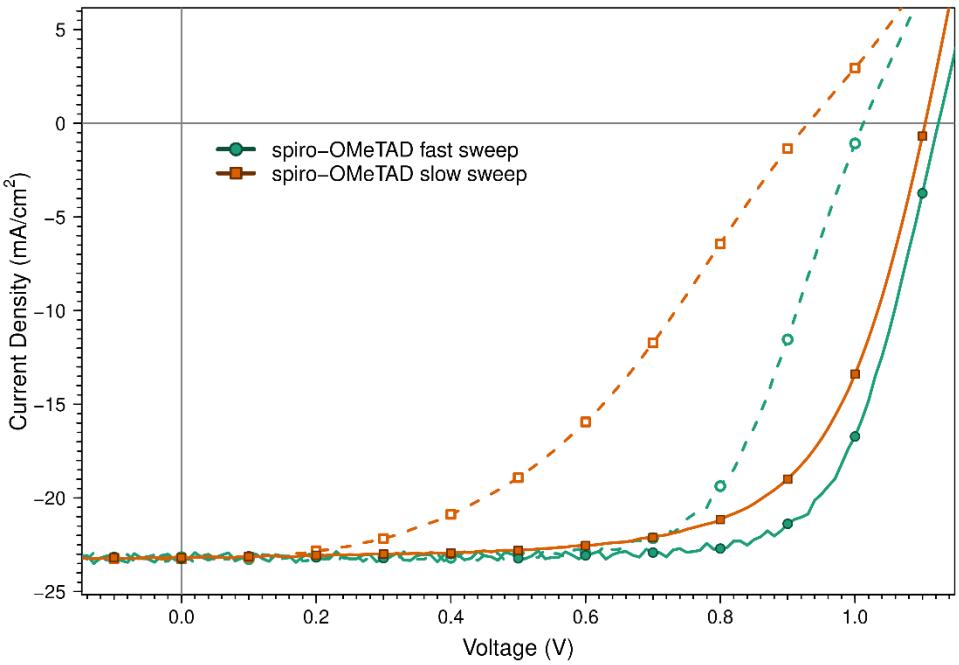

Figure S 32. A current-voltage scan of a device with spiro-OMeTAD as HTM. Fast sweep were performed at 600 mV/s while slow sweeps were performed at 30 mV/s.

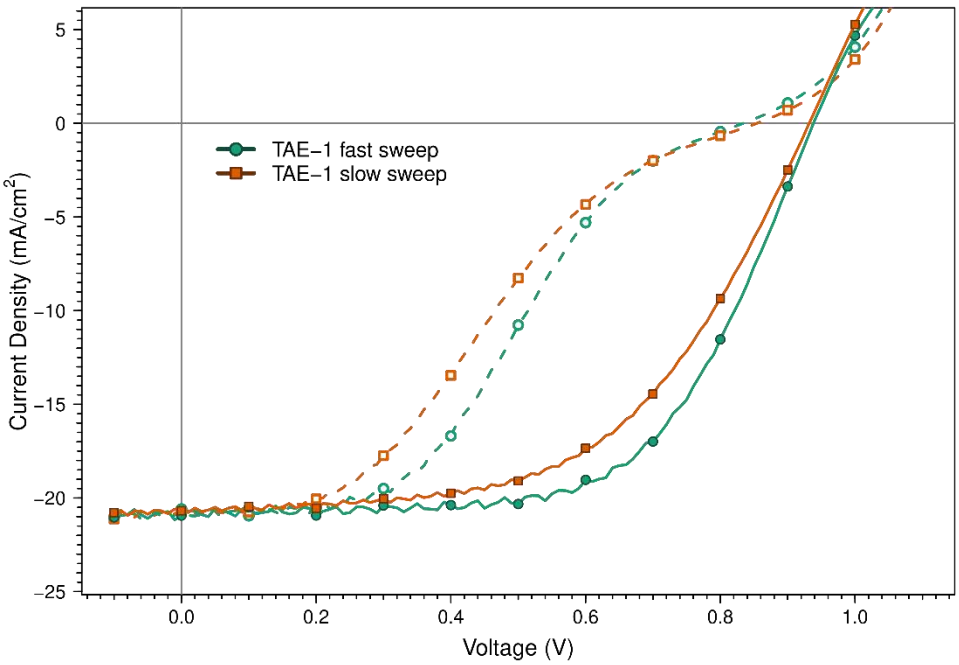

Figure S 33. A current-voltage scan of a device with TAE-1 as HTM. Fast sweep were performed at 600 mV/s while slow sweeps were performed at 300 mV/s.

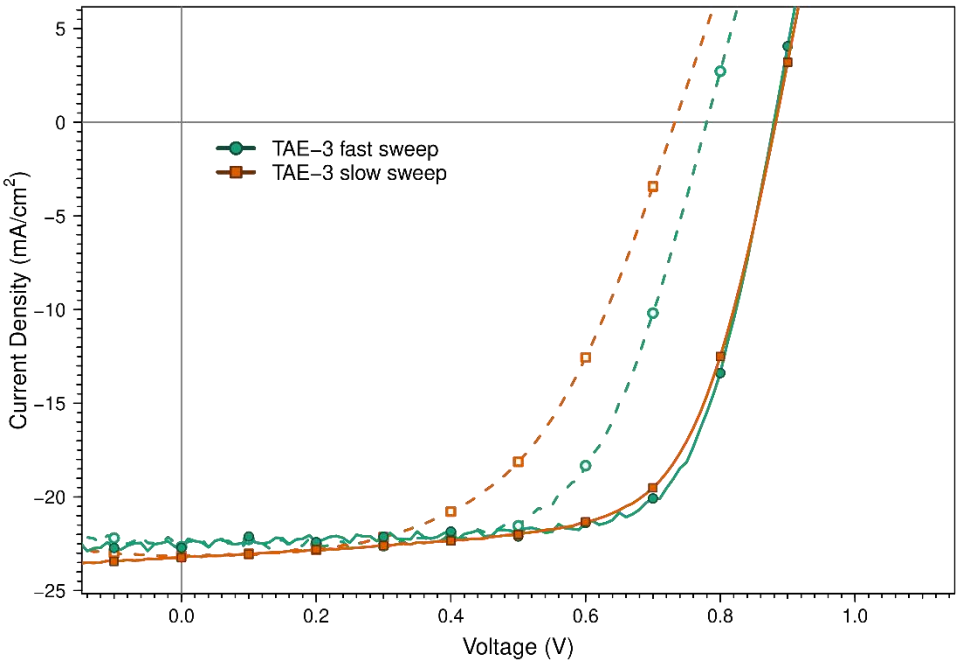

Figure S 34. A current-voltage scan of a device with TAE-3 as HTM. Fast sweep were performed at 600 mV/s while slow sweeps were performed at 80 mV/s.

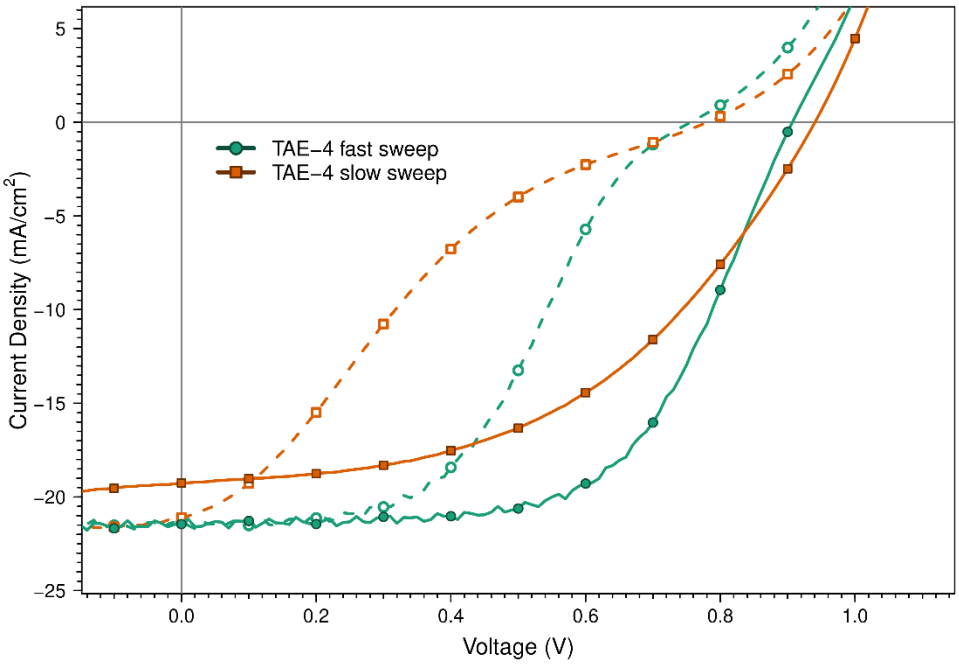

Figure S 35. A current-voltage scan of a device with TAE-4 as HTM. Fast sweep were performed at 600 mV/s while slow sweeps were performed at 30 mV/s.

15. Current-voltage Scans at Different Illumination Intensities

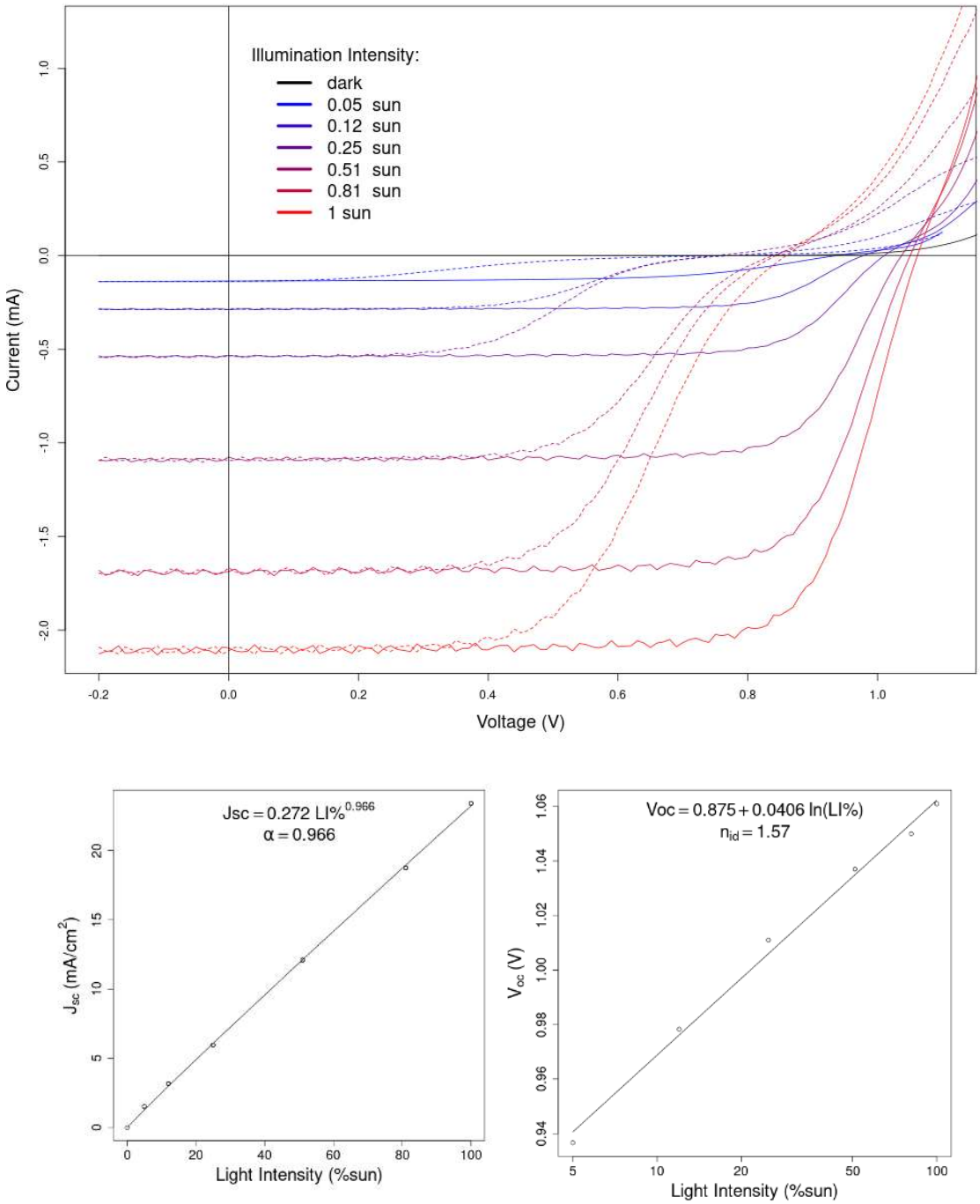

Figure S 36. Current-voltage scans of a perovskite solar cell with **spiro-OMeTAD** as HTM attenuating the solar simulator illumination with filters, scan speed 0.6 V/s: (top) forward (dashed) and reverse (solid); (bottom left) power law fitting of the short circuit current at different light intensity; (bottom right) linear fitting of the reverse scan open circuit voltage versus the natural logarithm of the light intensity, and the obtained ideality factor.

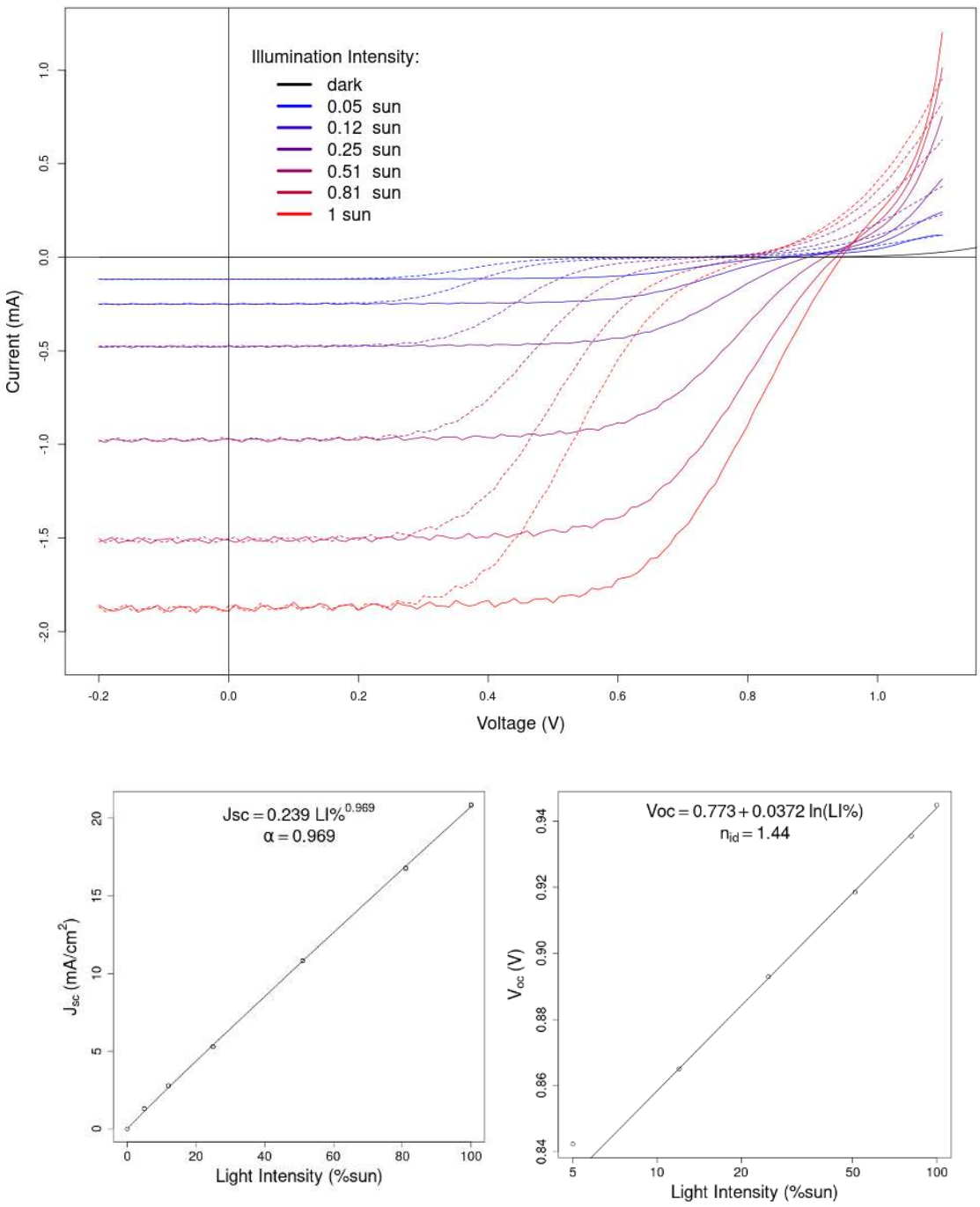

Figure S 37. Current-voltage scans of a perovskite solar cell with **TAE-1** as HTM attenuating the solar simulator illumination with filters, scan speed 0.6 V/s: (top) forward (dashed) and reverse (solid); (bottom left) power law fitting of the short circuit current at different light intensity; (bottom right) linear fitting of the reverse scan open circuit voltage versus the natural logarithm of the light intensity, and the obtained ideality factor.

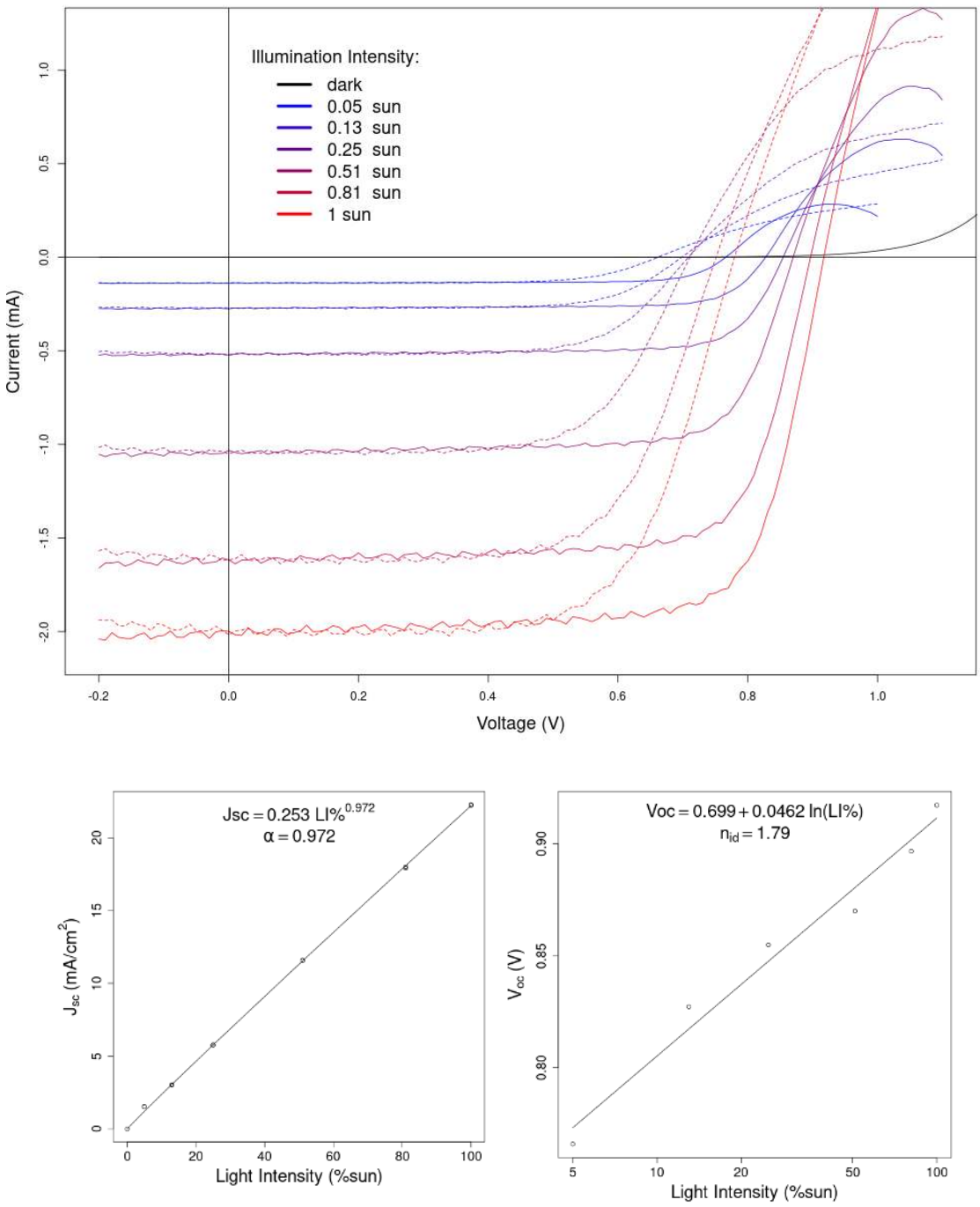

Figure S 38. Current-voltage scans of a perovskite solar cell with **TAE-3** as HTM attenuating the solar simulator illumination with filters, scan speed 0.6 V/s: (top) forward (dashed) and reverse (solid); (bottom left) power law fitting of the short circuit current at different light intensity; (bottom right) linear fitting of the reverse scan open circuit voltage versus the natural logarithm of the light intensity, and the obtained ideality factor.

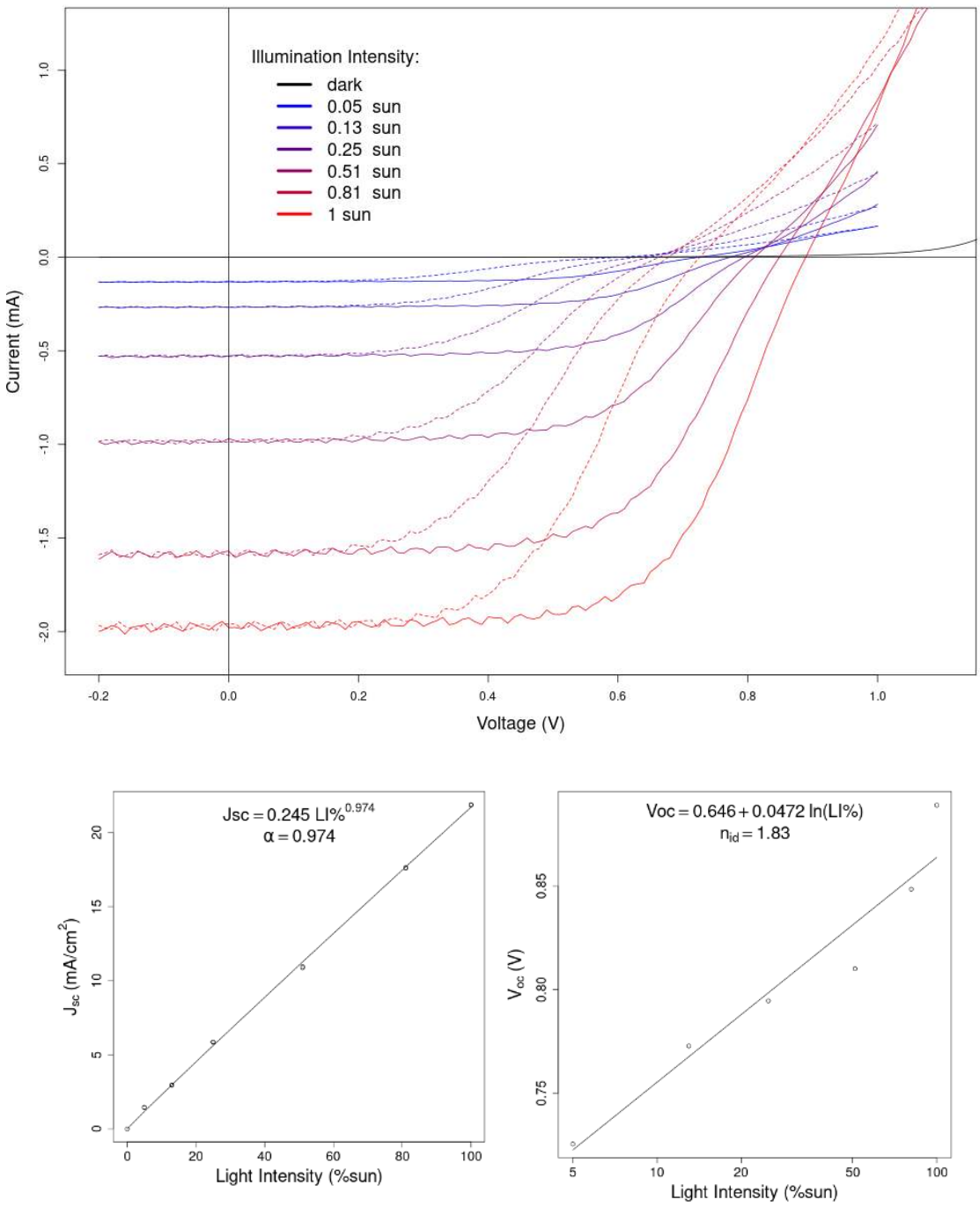

Figure S 39. Current-voltage scans of a perovskite solar cell with **TAE-4** as HTM attenuating the solar simulator illumination with filters, scan speed 0.6 V/s: (top) forward (dashed) and reverse (solid); (bottom left) power law fitting of the short circuit current at different light intensity; (bottom right) linear fitting of the reverse scan open circuit voltage versus the natural logarithm of the light intensity, and the obtained ideality factor.

16. Photo-induced time-resolve measurements

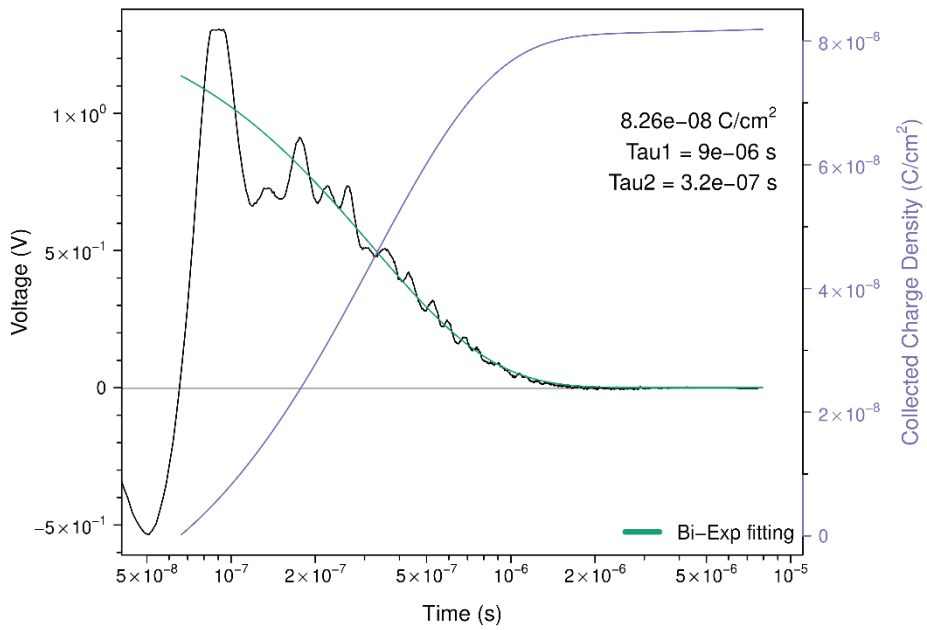

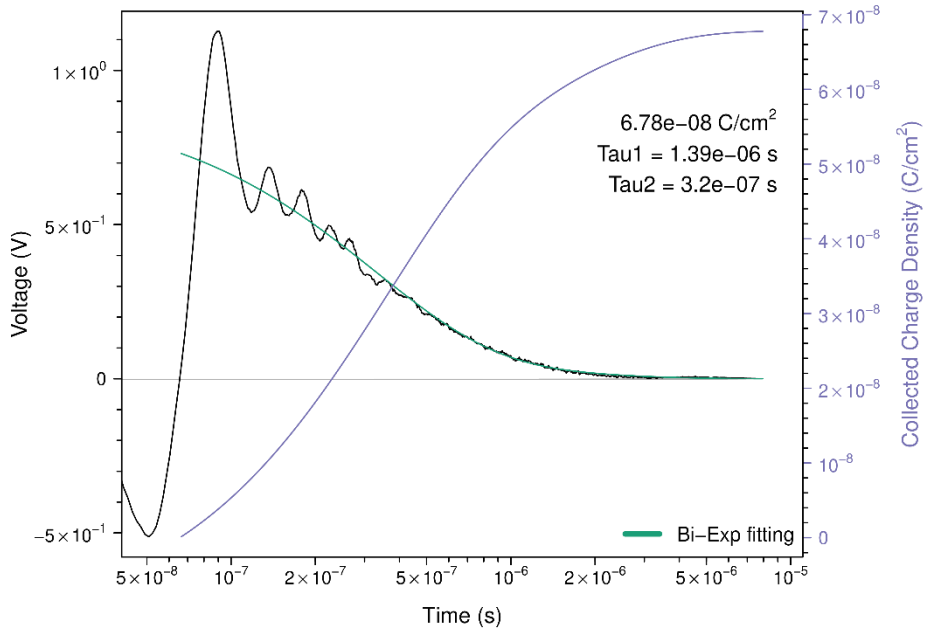

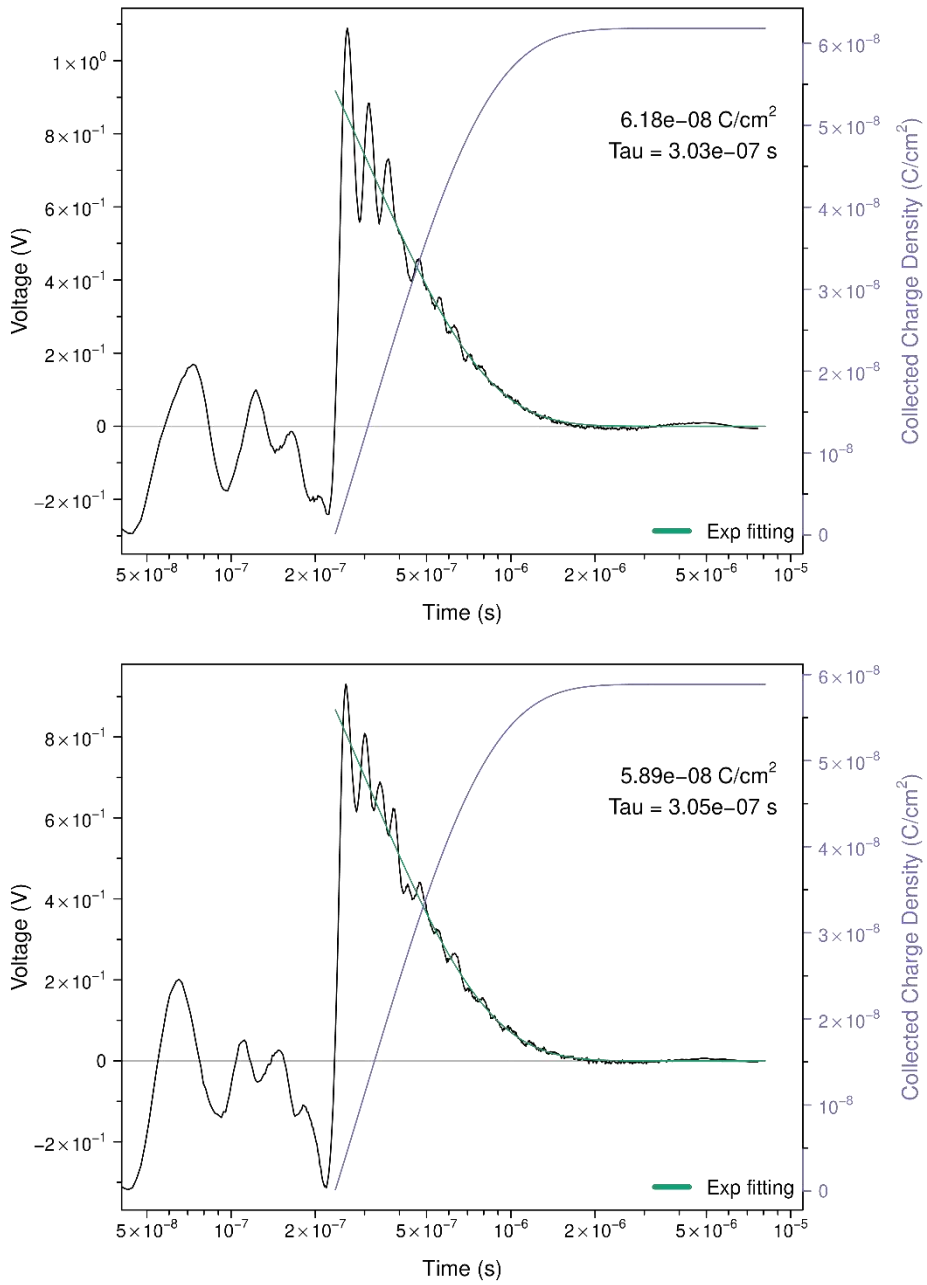

Figure S 40. Charge extraction profile (CE, black) at 1 sun equivalent illumination (lower illuminations have been measured but the full decay is not reported here) for (first) spiro-OMeTAD, (second) TAE-1, (third) TAE-3 and (fourth) TAE-4. The voltage profile can be converted to a current profile dividing by the external circuit resistance of 50 Ω. In grey the baseline for integration. In green the fitting with an exponential or a bi-exponential decay (sum of two exponential decays) as indicated in the legend. The exponential fitting was employed in the cases where bi-exponential fitting was not converging. In any case robust fitting was performed, as implemented in R/robustbase/nlrob.[17] In purple the integral of the fit. The whole procedure can be seen in https://github.com/ilario/photophysics-data-processing-R/blob/master/ce-integrateExp.R

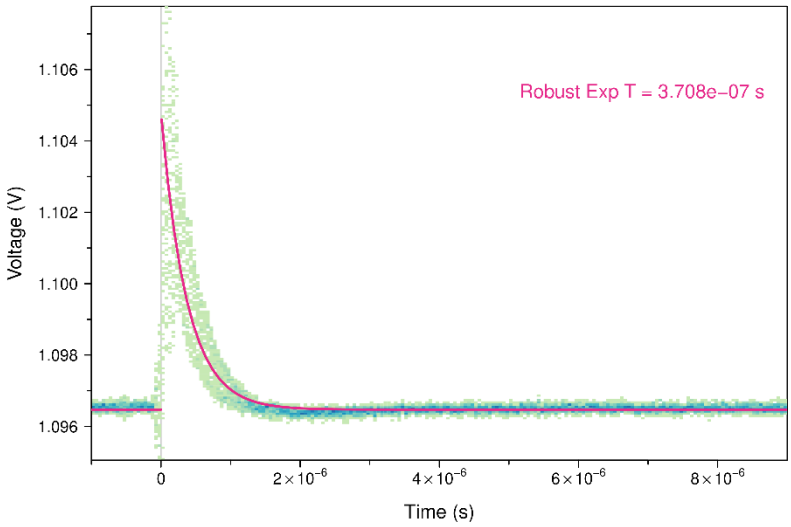
Robust Exp T = 3.708e−07 s
Voltage (V)
1.106
1.104
1.102
1.100
1.098
1.096
0
2×10⁻⁶
4×10⁻⁶
6×10⁻⁶
8×10⁻⁶
Time (s)

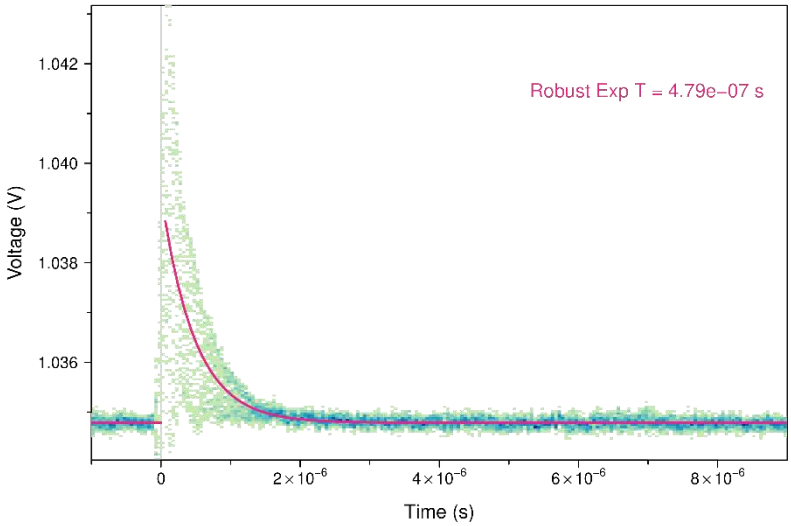
Robust Exp T = 4.79e−07 s
Voltage (V)
1.042
1.040
1.038
1.036
0
2×10⁻⁶
4×10⁻⁶
6×10⁻⁶
8×10⁻⁶
Time (s)

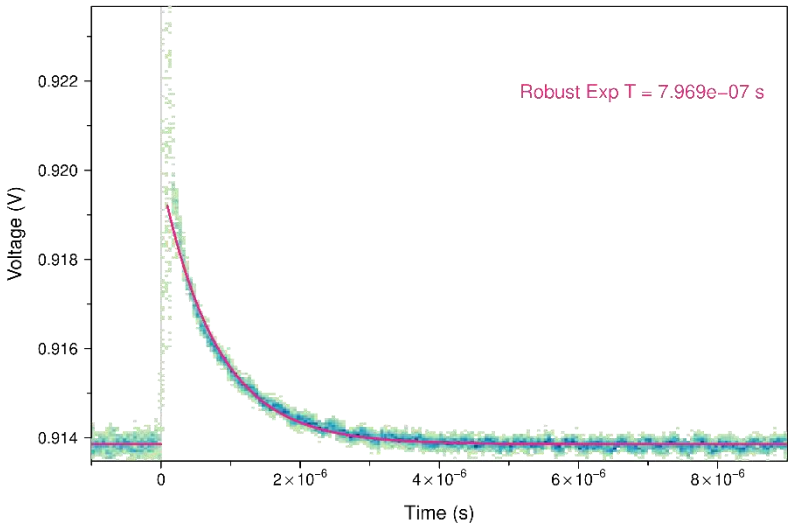
Robust Exp T = 7.969e−07 s
Voltage (V)
0.922
0.920
0.918
0.916
0.914
0
2×10⁻⁶
4×10⁻⁶
6×10⁻⁶
8×10⁻⁶
Time (s)

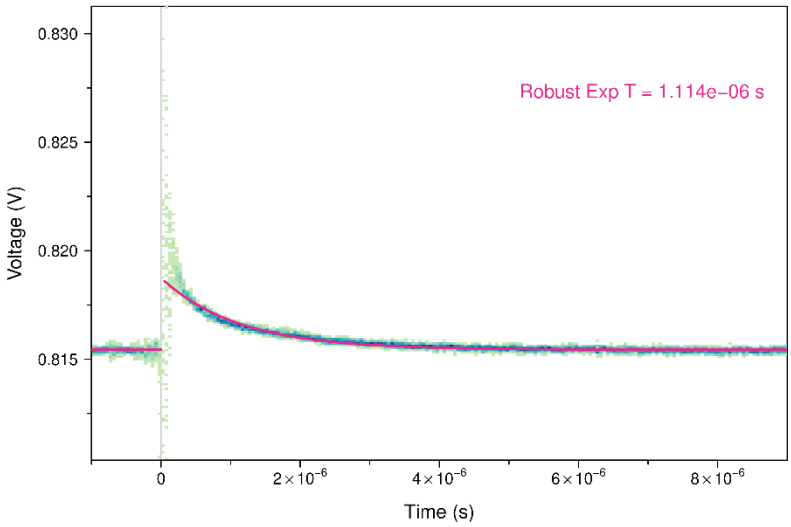

Figure S 41. Transient voltage decays from TPV (monitoring the V_{OC} profile evolution of a complete device after a perturbation via a laser pulse) of devices with (first) spiro-OMeTAD, (second) TAE-1, (third) TAE-3 and (fourth) TAE-4 as HTM. In this case the background illumination was equivalent to 1 sun. In order to limit the overplotting problem, the 12500 data points has been represented as a 2D histogram. The solid purple line represents the robust mono-exponential ($V = V_0 + \Delta V\ e^{-t/\tau}$) fitting as implemented in R/robustbase/nlrob.[17] The number reported in purple in the plot is the exponential coefficient τ from the fit. Biexponential fit ($V = V_0 + \Delta V_1\ e^{-t/\tau 1} + \Delta V_2\ e^{-t/\tau 2}$) has also been performed, showing no significant improvement.

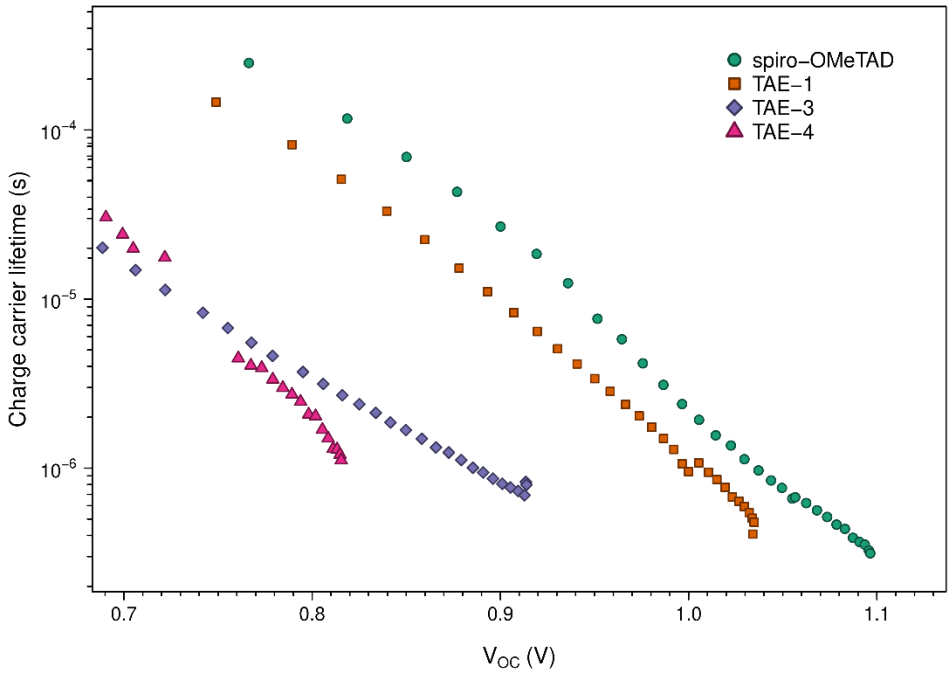

Figure S 42. Charge carrier lifetime at different applied illuminations (TPV). The x axis reports the V_{OC} due to the applied illumination (light bias)**.**

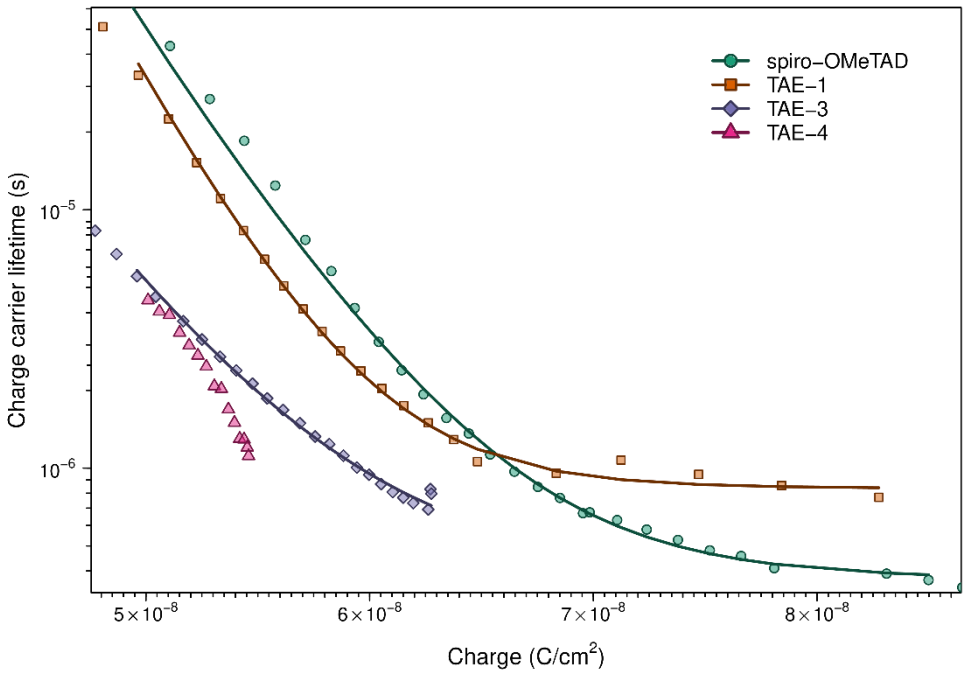

Figure S 43. Charge carrier lifetime (from TPV) plotted versus the total charge obtained via charge extraction (CE, including both charge stored in geometrical and chemical capacitance). The solid lines are power law fitting ($y=y_o+Ax^{-\lambda}$), as shown in the main text, but the recombination orders obtained in this case (considering also the geometrical capacitance charge) are unphysical (16 for spiro-OMeTAD devices, 18 for TAE-1 devices, 13 for TAE-3 devices, and it was not fitted for TAE-4).

17. Contact potential difference measurements for work function determination

Electrostatic force measurements were performed by means of an Scanning Probe Microscope to evaluate the contact potential difference between a metallic tip and the sample. The contact potential difference, CPD or V_{CPD}, can be measured from the parabolic dependence of the electrostatic force with the tip-sample applied bias. In dynamic electrostatic force measurements, an oscillating tip is not in direct contact with the sample but electrically connected via electronics, causing the alignment of their Fermi levels and, therefore, creating a CPD between tip and sample. If the work function of the tip (vibrating electrode) is ϕ_{tip} and ϕ_{sample} is that of the sample, then the contact potential difference between tip and sample is:

$$V_{CPD} = \frac{\phi_{tip} - \phi_{sample}}{-e} = {\Delta\varphi_s}/{e} \qquad (1)$$

where e is the electric charge. Due to this CPD, an electrostatic force is developed which has a parabolic dependence with the tip-sample bias voltage. As the frequency or phase shift of the oscillating probe is proportional to the force gradient, it will also present the same dependence:

$$\Delta f(V) = -\frac{f_0}{4k}\frac{\partial^2 C(z)}{\partial z^2}(V - V_{CPD})^2 \qquad (2)$$

where f_0, k, z, $C(z)$ and V_{CPD} are, respectively, the resonance frequency, spring constant, distance, capacitance and contact potential difference of the tip-sample system and Δf(V) is the magnitude measured. Thus, in principle, knowing the work function of the tip (ϕ_{tip}), the work function of the sample (ϕ_{sample}) can be calculated from (1). However, in order to avoid uncertainties related to the tip conditions or material, having an in-situ reference is convenient. The use of such a reference also permits reliable comparison between different samples. In the present case, this reference is provided by a gold electrode deposited on top of each surface layer. In such a way, the contact potential difference between the sample and the gold electrode (ϕ = 4.9 eV)[5] permits evaluating the sample work function independently of the material the tip is made of:

$$\Delta\phi = \phi_{sample} - \phi_{Au} = e\,[V_{CPD}(sample) - V_{CPD}(Au)] \qquad (3)$$

To obtain $\Delta\phi$ we perform spectroscopic curves: direct measurement of $\Delta f(V)$ by obtaining the frequency shift versus applied bias over specific surface locations. The robustness of the method and reproducibility of the results are verified by statistical analysis of measurements taken on diverse locations and several curves obtained at each position. As a measure of the precision, errors for each case are estimated as the standard deviation of the mean: SDOM = $\pm\,\sigma/\sqrt{n}$, where σ is the standard deviation of the data and n is the number of data values.

18. Supplementary references

1 L. Cabau, I. Garcia-Benito, A. Molina-Ontoria, N. F. Montcada, N. Martin, A. Vidal-Ferran and E. Palomares, *Chem. Commun.*, 2015, **51**, 13980–13982.

2 I. Horcas, R. Fernández, J. M. Gómez-Rodríguez, J. Colchero, J. Gómez-Herrero and A. M. Baro, *Rev. Sci. Instrum.*, 2007, **78**, 013705.

3 P. N. Murgatroyd, *J. Phys. D. Appl. Phys.*, 1970, **3**, 308.

4 J. A. Röhr, D. Moia, S. A. Haque, T. Kirchartz and J. Nelson, *J. Phys. Condens. Matter*, 2018, **30**, 105901.

5 I. D. Baikie, A. C. Grain, J. Sutherland and J. Law, *Appl. Surf. Sci.*, 2014, **323**, 45–53.

6 M. W. Wong, K. B. Wiberg and M. J. Frisch, *J. Am. Chem. Soc.*, 1992, **114**, 1645–1652.

7 F. Weigend and R. Ahlrichs, *Phys. Chem. Chem. Phys.*, 2005, **7**, 3297.

8 M. J. Frisch, G. W. Trucks, H. B. Schlegel, G. E. Scuseria, M. A. Robb, J. R. Cheeseman, G. Scalmani, V. Barone, G. A. Petersson, H. Nakatsuji, X. Li, M. Caricato, A. V Marenich, J. Bloino, B. G. Janesko, R. Gomperts, B. Mennucci, H. P. Hratchian, J. V Ortiz, A. F. Izmaylov, J. L. Sonnenberg, Williams, F. Ding, F. Lipparini, F. Egidi, J. Goings, B. Peng, A. Petrone, T. Henderson, D. Ranasinghe, V. G. Zakrzewski, J. Gao, N. Rega, G. Zheng, W. Liang, M. Hada, M. Ehara, K. Toyota, R. Fukuda, J. Hasegawa, M. Ishida, T. Nakajima, Y. Honda, O. Kitao, H. Nakai, T. Vreven, K. Throssell, J. A. Montgomery Jr., J. E. Peralta, F. Ogliaro, M. J. Bearpark, J. J. Heyd, E. N. Brothers, K. N. Kudin, V. N. Staroverov, T. A. Keith, R. Kobayashi, J. Normand, K. Raghavachari, A. P. Rendell, J. C. Burant, S. S. Iyengar, J. Tomasi, M. Cossi, J. M. Millam, M. Klene, C. Adamo, R. Cammi, J. W. Ochterski, R. L. Martin, K. Morokuma, O. Farkas, J. B. Foresman and D. J. Fox, *Gaussian 09 (Gaussian Inc., Wallingford, CT)*.

9 B. Balakrishna, A. Bauzá, A. Frontera and A. Vidal-Ferran, *Chem. - A Eur. J.*, 2016, **22**, 10607–10613.

10 G. Scalmani and M. J. Frisch, *J. Chem. Phys.*, 2010, **132**, 114110.

11 A. V Marenich, C. J. Cramer and D. G. Truhlar, *J. Phys. Chem. B*, 2009, **113**, 6378–6396.

12 S. Kupfer, J. Guthmuller and L. González, *J. Chem. Theory Comput.*, 2013, **9**, 543–554.

13 T. Yanai, D. P. Tew and N. C. Handy, *Chem. Phys. Lett.*, 2004, **393**, 51–57.

14 N. M. O'boyle, A. L. Tenderholt and K. M. Langner, *J. Comput. Chem.*, 2008, **29**, 839–845.

15 B. Wang, Z. Xie, Y. Li, Z. Yang and L. Chen, *Macromolecules*, 2018, **51**, 3443–3449.

16 M. Saliba, T. Matsui, J.-Y. Seo, K. Domanski, J.-P. Correa-Baena, M. K. Nazeeruddin, S. M. Zakeeruddin, W. Tress, A. Abate, A. Hagfeldt and M. Grätzel, *Energy Environ. Sci.*, 2016, **9**, 1989–1997.

17 M. Maechler, P. Rousseeuw, C. Croux, V. Todorov, A. Ruckstuhl, M. Salibian-Barrera, T. Verbeke, M. Koller, E. Concieção and M. A. di Palma, 2018, robustbase: Robust statistics R package 0.93-3.